Coherently seeded broadband ultrafast fiber amplifiers

by

Anupamaa Rampur

Dissertation presented for the degree of Doctor of Philosophy at the University of Warsaw

Adviser: Dr. hab. Mariusz Klimczak
Co-adviser: Dr. Tomasz Stefaniuk
Faculty of Physics, Department of Information Optics,
University of Warsaw, Poland

May 2020

Abstract

The dissertation will be focused on optical, coherently seeded ultrafast fiber amplifiers. Research work shall include building of experimental setups for characterization and spectro-temporal characterization of coherent supercontinuum, as well as building of fiber amplifier setups and their characterization. Specifically, thulium-doped, and synchronized thulium-doped and erbium-doped amplifiers will be investigated, under optical seeding from a common, coherent supercontinuum signal. Research will be therefore conducted using laser sources covering wavelengths around 1560 nm and between 1800 nm and 2100 nm, which correspond to gain bands of erbium-doped and thulium-doped fiber amplifiers. In particular, the latter – amplifiers based on thulium doped active fibers is especially interesting because these devices dispose of the widest gain band among the three main fiber amplifiers (doped with either of Yb^{3+}, Er^{3+} or Tm^{3+} ions). It is planned, that during the work, advantage would be taken from seeding one or two amplifiers from a common, spectrally broad, and coherent seed signal. This would specifically include addressing of entire amplification bandwidth of every seeded amplifier, as well as intrinsic synchronization and assuring of the same CEO (carrier-envelope offset) of pulses amplified in each of the seeded amplifiers. This opens entirely new possibilities in generation and synthesis of ultrashort light pulses in all-fiber systems.

The first part of dissertation shall include description of measurements and detailed analysis of results obtained in spectro-temporal characterization of group delay in coherent supercontinuum light pulses in all-normal dispersion photonic crystal fibers. This part of work is aimed at experimental verification of temporal structure of spectrally broad pulses and selecting the most suitable fiber for generation of seed signal for seeding of ultrafast amplifiers. Selection criteria shall include dispersion and nonlinear properties, as well as birefringence and feasibility to obtain linearly polarized and spectrally broad seed pulses.

In the second part of work, discussion shall be focused on experimental results of broadband seeding of thulium doped fiber amplifiers. The research will include work on setups built using polarization maintaining optical fibers and fiber components. Research methodology will be based on measurements of group delay characteristics using frequency resolved optical gating (FROG) and on measurements of noise characteristics of amplifiers, while the general aim of work will be

identification of the compression point, i.e. the shortest obtainable output pulse duration in the investigated systems. Various factors influencing the compression point will be discussed, including seed pulse characteristics, spectral width of the output pulse, uncompensated third-order dispersion.

The third part of dissertation shall be dedicated to discussion of results obtained with seeding of thulium-doped fiber amplifiers and erbium-doped amplifiers with a common, broadband and coherent seed signal. Only polarization maintaining fiber-based setups will be investigated. In addition to characterization of group delay profiles and noise performance of the output pulses, the work includes an attempt of nonlinear mixing of the two output pulses from each of the amplifiers and generation of sum frequency signal. The discussion thus includes results of work on group delay matching between the output pules, as well as their spectro-temporal characteristics and measurements of noise characteristics of the obtained sum frequency signal.

Streszczenie

Rozprawa będzie dotyczyć ultraszybkich wzmacniaczy światłowodowych zasiewanych koherentnym sygnałem szerokopasmowym. Badania obejmą budowę układów eksperymentalnych do charakteryzacji oraz charakteryzację spektralno-czasową sygnału szerokopasmowego w postaci źródła czasowo-spójnego superkontinuum, budowę układów wzmacniaczy światłowodowych oraz ich charakteryzację. W szczególności badane będą światłowodowe wzmacniacze tulowe, oraz układy wzmacniaczy tulowych i erbowych zasiewanych ze wspólnego źródła koherentnego sygnału szerokopasmowego. Prace będą zatem prowadzone przy wykorzystaniu źródeł laserowych na zakres długości fali wokół 1560 nm oraz pomiędzy 1800 nm i 2100 nm, które odpowiadają pasmom wzmocnienia światłowodowych wzmacniaczy erbowych oraz tulowych. W szczególności ta druga grupa – wzmacniaczy wykorzystujących światłowody domieszkowane jonami Tm^{3+} jest szczególnie interesująca, ze względu na najszersze dysponowane pasmo wzmocnienia wśród trzech głównych wzmacniaczy światłowodowych (domieszkowanych odpowiednio jonami Yb^{3+}, Erb^{3+} lub Tm^{3+}). W trakcie badań, wykorzystane mają być zalety oczekiwane w przypadku zasiewania jednego lub dwóch wzmacniaczy wspólnym sygnałem szerokopasmowym. Należy tu wymienić adresowanie całego pasma wzmocnienia każdego wzmacniacza w układzie, możliwość automatycznej synchronizacji dwóch różnych wzmacniaczy przy jednoczesnym zapewnieniu tego samego przesunięcia obwiednia-nośna we wszystkich zasiewanych wzmacniaczach. Otwiera to ciekawe możliwości w generacji i syntezie ultrakrótkich impulsów światła w układach całkowicie światłowodowych.

W pierwszej części pracy zawarty zostanie opis pomiarów i szczegółowej analizy wyników w zakresie charakteryzacji spektralno-czasowej impulsów przewidzianych jako sygnał zasiewający. Badane będą charakterystyki opóźnienia grupowego impulsów koherentnego superkontinuum w światłowodach fotonicznych o charakterystyce dyspersji chromatycznej całkowicie w zakresie normalnym. Celem badań będzie eksperymentalne potwierdzenie struktury czasowej impulsu o szerokim widmie oraz wybór światłowodu najlepszego do zastosowania w generacji sygnału zasiewającego dla ultraszybkich wzmacniaczy światłowodowych. Kryterium wyboru będzie uwzględniało właściwości dyspersyjne i nieliniowe, a także dwójłomność i możliwość uzyskania szerokopasmowego impulsu zasiewającego o polaryzacji liniowej.

W drugiej części pracy zawarte zostaną wyniki badań zasiewania szerokopasmowego światłowodowych wzmacniaczy tulowych. Badania będą dotyczyły układów eksperymentalnych zbudowanych ze światłowodów oraz komponentów światłowodowych utrzymujących polaryzację. Metodologia badań będzie zawierała pomiary charakterystyk opóźnienia grupowego w układzie frequency-resolved optical gating, pomiary charakterystyk szumowych wzmacniaczy, a ogólnym celem badań będzie wskazanie punktu kompresji, czyli najkrótszego osiągalnego czasu trwania impulsu wyjściowego w badanym układzie. Dyskusja obejmie wpływ na punkt kompresji czynników tj. charakterystyka impulsu początkowego, pasmo wzmocnionego impulsu, nieskompensowana dyspersja trzeciego rzędu.

W trzeciej części pracy omówione będą wyniki badań układów wzmacniaczy tulowych oraz erbowych zasiewanych wspólnym spójnym sygnałem szerokopasmowym. Wyniki badań zawarte w dwóch poprzednich częściach pracy oraz komplikacja układu dwóch wzmacniaczy sprawia, że podjęta zostanie próba budowy układu z wykorzystaniem wyłącznie światłowodów i komponentów światłowodowych utrzymujących polaryzację. Ponad badania charakterystyk opóźnienia grupowego i właściwości szumowych w tej części pracy podjęta została próba mieszania nieliniowego impulsów wyjściowych każdego z obydwu wzmacniaczy i generacji sygnału o częstości sumacyjnej. Omówione zostały zatem wyniki prac związane z kontrolą opóźnienia grupowego pomiędzy impulsami oraz z ich charakteryzacją czasowo-spektralną, a także z pomiarami charakterystyki szumowej sygnału o częstości sumacyjnej.

Acknowledgments

I wish to express my sincere thanks to, Prof. dr hab. Ryszard Buczyński for providing me the wonderful opportunity to work in the laboratory. I would like to express my heartfelt thanks to my supervisor Dr. hab. Mariusz Klimczak for all the scientific discussion, guidance, motivation, advice, and continued support throughout my research. I am grateful for the patience and support of my supervisor to guide through my mistakes and for the successful completion of the thesis. Also, I would like to thank him for all the timely help which made my days in Poland easy.

I would like to thank Dr. hab. Yuriy Stepanenko for giving me the opportunity to work in the Institute of Physical Chemistry and for his valuable inputs on building amplifier setup and fruitful scientific discussions. I also thank Dr. Tomasz Kardaś for valuable insights about designing amplifier systems

I am grateful for Prof. Dr. Alexander M. Heidt for hosting me twice at the University of Bern and giving me the opportunity to learn from him. I extended my thanks to Prof. Thomas Feurer and Dr. Dirk Mathys Spangenberg for their valuable discussions.

I wish to express my sincere thanks to my Colleague, Mr. Dominik Dobrakowski, and Dr. Grzegorz Stępniewski with whom I enjoyed working along in this project.

I would also like to thank all the current and former colleagues of my laboratory for their continuous support and help in providing me a friendly scientific atmosphere.

I would like to thank all my friends in Warsaw for nice trips, potluck, and recreational activities.

Finally, I would like to express my gratitude to my family (Dad, Mom, and Sister) and friends in India for their continuous support and encouragement. I am particularly grateful to my boyfriend Dr. Karthik Mohanraj for his invaluable patience and a constant motivation for work.

This work has been realized within the First TEAM program of the Foundation for Polish Science co-financed by the European Union under the European Regional Development Fund, project number First TEAM/2016-1/1, POIR.04.04.00-00-1D64/16-00.

Finally, I acknowledge the Schlumberger Foundation for awarding me the Faculty for the Future fellowship.

List of publications

The following publications resulted from the work on this dissertation:

Journal publications:

1. P. Ciąćka, **A. Rampur**, A. Heidt, T. Feurer, and M. Klimczak, “Dispersion measurement of ultra-high numerical aperture fibers covering thulium, holmium, and erbium emission wavelengths,” J. Opt. Soc. Am. B 35, 1301–1307 (2018).
2. D. Dobrakowski, **A. Rampur**, G. Stępniewski, A. Anuszkiewicz, J. Lisowska, D. Pysz, R. Kasztelanic, and M. Klimczak, “Development of highly nonlinear polarization-maintaining fibers with normal dispersion across entire transmission window,” J. Opt. (United Kingdom) 21, (2019).
3. **A. Rampur**, Y. Stepanenko, G. Stępniewski, T. Kardaś, D. Dobrakowski, D.-M. Spangenberg, T. Feurer, A. Heidt, and M. Klimczak, “Ultra low-noise coherent supercontinuum amplification and compression below 100 fs in an all-fiber polarization-maintaining thulium fiber amplifier,” Opt. Express 27, 35041 (2019).
4. **A. Rampur**, D.-M. Spangenberg, G. Stępniewski, D. Dobrakowski, K.Tarnowski, K. Stefańska, A. Paździor, P. Mergo, T.Martynkien, T. Feurer, M. Klimczak, and A. M. Heidt, “Temporal fine structure of all-normal dispersion fiber supercontinuum pulses caused by non-ideal pump pulse shapes,” Optics Express, manuscript accepted for publication (2020)

Conference contributions:

1. D. Dobrakowski, **A. Rampur**, G. Stępniewski, A. Anuszkiewicz, J. Lisowska, D. Pysz, R.ł Kasztelanic and M. Klimczak, “Development of highly nonlinear polarization maintaining fibers with normal dispersion across entire transmission window,” in XIV International Workshop on Nonlinear Optics Applications NOA’2018, 23-26 May 2018, Wroclaw, Poland.
2. D. Dobrakowski, **A. Rampur**, G. Stępniewski, A. Anuszkiewicz, J. Lisowska, D. Pysz, R.ł Kasztelanic and M. Klimczak, “Development of highly nonlinear polarization maintaining fibers with normal dispersion across entire transmission window,” in 8th EPS-QEOD Europhoton Conference Solid State, Fibre, and Waveguide Coherent Light Sources, 02-07 Sep 2018, PRBB Congress Centre, Barcelona, Spain.
3. **A. Rampur**, G. Stępniewski, D. Dobrakowski, Y. Stepanenko, T. Feurer, A. Heidt, and M. Klimczak, “96 fs all-fiber polarization maintaining thulium doped amplifier seeded by coherent supercontinuum,” in 2019 Conference on Lasers and Electro-Optics Europe and European Quantum Electronics Conference, OSA Technical Digest (Optical Society of America, 2019), paper cj_1_6.
4. D. Dobrakowski, **A. Rampur**, G. Stępniewski, R. Kasztelanic, A. Anuszkiewicz, D. Pysz, R. Buczyński, and M. Klimczak, “Development of all-glass all-normal dispersion highly

nonlinear photonic crystal fibers with introduced birefringence," in The European Conference on Lasers and Electro-Optics (Optical Society of America, 2019), p. cj_p_42.

5. **A. Rampur**, G. Stępniewski, D. Dobrakowski, Y. Stepanenko, A. Heidt, T. Feurer, and M. Klimczak, "All-fiber polarization maintaining Thulium doped amplifier seeded by coherent polarized supercontinuum," in Conference on Lasers and Electro-Optics, OSA Technical Digest (Optical Society of America, 2019), paper SM3L.5.

Journal publications out of the scope of this thesis:

1. **A. Rampur**, P. Ciąćka, J. Cimek, R. Kasztelanic, R. Buczyński, and M. Klimczak, "Development of suspended core soft glass fibers for far-detuned parametric conversion," J. Opt. (United Kingdom) 20, (2018).
2. D. Dobrakowski, **A. Rampur**, G. Stępniewski, D. Pysz, L. Zhao, Y. Stepanenko, R. Buczyński, and M. Klimczak, "Femtosecond pulse delivery around 1560 nm in large-core inhibited-coupling fibers," JOSA B 36, 3030–3038 (2019).
3. T. Karpate, G. Stepniewski, D. Pysz, **A. Rampur**, Y. Stepanenko, R. Buczynski, and M. Klimczak, "Soliton detuning of 68.5 THz in the near-infrared in a highly nonlinear suspended core tellurite fiber," J. Opt. Soc. Am. B 37, 1502–1509 (2020).
4. M. Heidt, J. Modupeh Hodasi, **A. Rampur**, D.-M. Spangenberg, M. Ryser, M. Klimczak, and T. Feurer, "Low noise all-fiber amplification of a coherent supercontinuum at 2 μm and its limits imposed by polarization noise," arXiv e-prints arXiv:1903.09583 (2019).

Conference contributions out of scope of this thesis:

1. **A. Rampur**, P. Ciąćka, J. Cimek, R. Kasztelanic, R. Buczyński and M. Klimczak, "Far-detuned parametric conversion in suspended core soft glass fiber by picosecond pumping," in 8th EPS-QEOD Europhoton Conference Solid State, Fibre, and Waveguide Coherent Light Sources, 02-07 Sep 2018, PRBB Congress Centre, Barcelona, Spain.
2. **A. Rampur**, P. Ciąćka, J. Cimek, R. Kasztelanic, R. Buczyński and M. Klimczak, "Far-detuned parametric conversion in suspended core, heavy metal oxide soft glass fibers," XIV International Workshop on Nonlinear Optics Applications NOA'2018, 23-26 May 2018, Wroclaw, Poland. **Best Oral Presentation.**
3. D. Dobrakowski, **A. Rampur**, G. Stępniewski, D. Pysz, L. Zhao, Y. Stepanenko, R. Buczyński and M. Klimczak, "Femtosecond pulse delivery around 1560 nm in large-core anti-resonant fibers," in 19th Conference on Optical Fibers and Their Applications, Białowieża 27-31.01.2020.

List of acronyms

SC - Supercontinuum

RI - Refractive index

SPM - Self phase modulation

XPM - Cross phase modulation

ZDW - Zero dispersion wavelength

MI - Modulation instability

OWB - Optical wave breaking

PCF - Photonic crystal fiber

ANDi - All normal dispersion

CW - Continuous wave

FWHM - Full-width half-maximum

GNLSE - Generalized nonlinear Schrodinger equation

GVD - Group velocity dispersion

TOD - Third-order dispersion

CPA - Chirped pulse amplification

FCPA - Fiber chirped pulse amplification

HW - Half-wave plate

ISO - Isolator

OSA - Optical spectrum analyzer

PER - Polarization extinction ratio

WDM - Wavelength division multiplexer

UHNA - Ultra-high numerical aperture

Tm - Thulium

Er – Erbium

Yb - Ytterbium

CEP - Carrier envelope phase

ASE - Amplified spontaneous emission

NA - Numerical aperture

MFD - Mode field diameter

rms - Root-mean-square

SEM - Scanning electron microscope

ESA - Electrical spectrum analyzer

PD - Photodiode

PM - Polarization maintaining

PMI - Polarization modulation instability

RIN - Relative intensity noise

SHG - Second harmonic generation

SFG - Sum frequency generation

BBO - beta barium borate

TBP - Time-bandwidth product

LMA - Large mode area

FROG - Frequency-resolved optical gating

XFROG – Cross-correlation frequency-resolved optical gating

VA - Voltage amplifier

Contents

Chapter 1. Introduction

The advent of the ultrafast mode-locked fiber laser sources had a major scientific impact and enabled advancements in direct observation of some of the fastest processes in nature [1], materials processing [2], spectroscopy [3], sensing [4], optical signal processing [5] and optical fiber communication systems [6]. In the recent years, near-infrared, rare-earth-doped fiber-based laser sources especially around 1.5 μm to 2 μm wavelength have become essential tools for spectroscopy, frequency combs, and precision metrology, as well as in the exploration of the molecular fingerprint region in the mid-infrared via nonlinear frequency conversion [7–11]. The application-driven requirements are constantly becoming more demanding, because of their compactness, wide spectral bandwidth, and ultra-low noise. But some of the applications requires broadband, high-energy, and high-power sources for laser filamentation [12] and high harmonic generation [13] which are not readily available.

Energy scaling can lead to the destruction of ultrashort pulses in bulk optics because of their intensity-dependent refractive index (RI) which leads to self-focusing. This problem can be overcome by chirped-pulse amplification (CPA). The CPA technique for ultrashort light pulse amplification was introduced in 1985 [14] and won the 2018 Nobel Prize in physics by Donna Strickland and Gérard Mourou. In CPA, pulses are stretched in time (chirped), amplified, and subsequently recompressed to duration depending on dispersion management (dechirping) approaches taken in the system design. This method is widely used in optical parametric chirped-pulse amplification (OPCPA), which incorporates bulk optics and overall operation depends on dispersion management [15]. It is further extended and extensively used in fiber laser and amplifier sources and called fiber chirped-pulse amplification (FCPA). In the FCPA system, the stretched pulse is amplified in a gain fiber and then recompressed to a very short duration. Here dispersion management is achieved by proper use of normal and anomalous dispersion fibers to effectively stretch and recompress the pulses. In the case of broadband operation, it is very important to know the broadband dispersion for successively building fiber laser and amplifier systems.

Nonlinear properties of fibers are extensively studied in relation to the growth of pulse energy in picosecond and femtosecond fiber lasers. Additionally, improvements in the fabrication technology of optical fibers in the 1970s [16], ultimately led to their use in nonlinear optics as the nonlinear medium. The advantage is that the well-defined spatial modes offer high beam intensity that can be sustained over larger propagation distances. Further interest in exploring the nonlinear effects in fibers led to the invention of the photonic crystal fiber (PCF) [17–19] and the subsequent demonstration of supercontinuum (SC) generation [20]. The SC generation was demonstrated earlier in bulk materials and standard nonlinear fibers [21–23]. The possibility of controlling the geometry and dispersion characteristics in PCF paved its way into nonlinear optics, creating its important, fiber-based branch in this community [19]. The common type of PCF has a solid silica core with surrounding silica cladding with air-holes. The PCF can offer enhanced nonlinearity compared to conventional fibers under proper design conditions [24] and can exhibit single-mode behavior over a broad wavelength range [25]. The SC broadening undergoes different nonlinear processes depending on whether it is pumped in normal or anomalous dispersion regime and depending on pump pulse parameters such as central wavelength (especially in relation to the zero-dispersion wavelength (ZDW) of the nonlinear medium i.e. the fiber) or the pulse duration.

There is a high demand for pump sources to produce broadband and highly coherent spectra. The most common SC generation was studied in conventional fiber with single ZDW and pumped in the anomalous dispersion regime. The spectral broadening dynamics are in this case dominated by soliton dynamics, in particular, the break-up of the injected pulse due to soliton fission [26]. In this case, in order to maintain the temporal coherence of generated SC pulses, highly stable pulses of typically less than 50 fs duration and at least several nanojoule pulse energy are required [27]. For longer pulses, the SC dynamics become sensitive to input pulse fluctuations and pump laser shot noise due to the increasing noise amplification through modulation instability (MI) and soliton fission [28,29]. Consequently, such broad SCs pulses show a complex temporal and phase profile, with considerable fine structures over their spectral bandwidth [30]. They also exhibit pulse-to-pulse variations if pumped by long pump pulses [31]. These problems associated with soliton dynamics and MI can be worked around by pumping in the normal dispersion wavelengths of fibers with engineered all-normal dispersion (ANDi) characteristics. Pumping with femtosecond pulses favors the self-seeded self-phase modulation (SPM) spectral broadening, which for non-parabolic profile pump pulses is followed by the onset of new wavelength components through optical wave breaking (OWB). This can result in octave-spanning SC bandwidths with uniformly flat spectral profiles, and, most importantly, high stability and coherence for a range of pump pulse parameters [32–37]. However, recent numerical study demonstrated the limitations in the coherence of ANDi SC for high peak powers and pump pulses around 2 ps. One of the other possibilities of SC coherence degeneration is polarization modulational instability (PMI), which is a form of modulation instability that affects the polarization state of light that propagates through the fiber [38,39]. Hence, PMI assisted by the weak unintentional birefringence of the fibers leads to significant pulse-to-pulse fluctuation and coherence degradation of SC pulses even in all-normal dispersion fibers [40,41]. Therefore the use of polarization-maintaining ANDi fibers has been proposed to avoid such limitations [42,43].

Many of SC-based applications require uniform and smooth spectral and temporal profiles. ANDi SC pulses are often assumed to fulfill these requirements, backed up by many numerical simulations available in literature covering various fiber designs and pump wavelengths (e.g. [33,44–48]). However, detailed experimental data on the spectro-temporal characteristics of ANDi SC pulses is scarce [49,50], yet such measurements are necessary to evaluate the properties of ANDi SC and its suitability for specific applications under real pumping conditions.

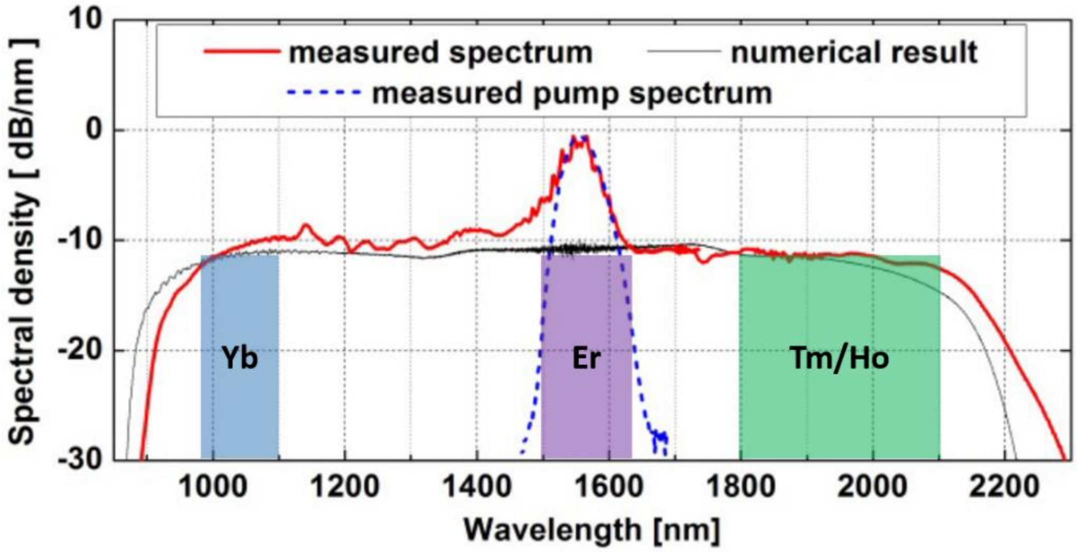

Figure 1.1. Supercontinuum generated in ANDi all solid PCF [51]

Dispersion engineering in solid-core ANDi PCF has enabled coherent SC extension over much of the long-wave near-infrared range of the spectrum, as shown in figure 1.1 [51–53] in recent years. These SC pulses with a high degree of temporal coherence and octave-spanning spectral bandwidths enable stabilized optical frequency combs that have revolutionized the fields of precision spectroscopy and frequency metrology. In addition, the SC can also cover three main amplification bandwidths of the trivalent ytterbium, erbium, and thulium dopant ions. Although

SC sources have been successfully exploited in many applications [23,54,55], an important drawback is the small core diameters and large RI steps are required for effective dispersion engineering [56,57]. As a result spectral or temporal shaping ultrashort pulses usually remain restricted to relatively low pulse energies of a few nano Joules, limited by the damage threshold of small-core PCFs [58].

One approach for boosting the pulse energy is using the entire or partial spectral bandwidth of low energy SC pulses as shown in figure 1.1 for coherent seeding of broadband amplifiers. To date in the context of optical fiber amplifiers, this has mainly been explored in 2 μm region using the solitonic part of conventional SC pumped in the anomalous dispersion region of highly nonlinear fibers and PCFs [59–62] The reported integrated root mean squared (rms) relative intensity noise (RIN) values of such systems are typically in the range 0.3 - 0.7%. In contrast to these previous works, the SC pulses generated in non-PM ANDi fibers were used as seed sources in [63] for seeding of Tm/Ho doped fiber, reported low noise of 0.07% RIN, but PMI was one of the limiting factors. Hence ANDi SC with highly birefringent combination offer several key advantages and is especially relevant in the context of ultrashort pulse amplification [64]: (I) noise amplifying nonlinear dynamics are suppressed in ANDi fibers such that the generated SC can have lower relative intensity noise (RIN) than the pump laser [45,48,63,65]. In contrast, conventional SC solitons and MI amplify pump laser noise [60,66]. (II) ANDi SC preserves the temporal integrity of the pump pulse and exhibits flat, smooth, and stable spectra that can be compressed to high-quality single-cycle pulses [67,68]. (III) The conventional SC may exhibit significant temporal jitter between wavelength components, the jitter of wavelength components far from the pump is reduced by 2 orders of magnitude in normal dispersion SC, reaching attosecond precision [69] (IV) PMI in the ANDi SC can be suppressed by employing only highly birefringent PCF pumped along their principal axis [41–43]. All these properties enable the realization of synchronous ultrafast seeding of multiple amplifiers operating at different wavelengths. Hence in this thesis, I implement the benefits of using PM ANDi SC pulses for broadband, coherent seeding of ultrafast amplifiers.

The main objectives of my work are:

1. Design and development of experimental, fiber-based setups for amplification of coherent, polarized seed signals in the 2 μm spectral window and its subsequent temporal recompression to below 100 fs.

2. Design and development of a fiberized platform enabling simultaneous coherent seeding of erbium and thulium fiber amplifiers and their output pulse compression and nonlinear mixing.

Detailed goals of the dissertation are:

- **experimental characterization of the dependence between the front-end driving laser full-filed parameters (pulse spectrum, pulse time shape, phase profile) and spectro-temporal structure of coherent supercontinuum seed pulses, as well as of amplified pulses at output of amplifier – using frequency resolved optical gating techniques and full-field information retrieval algorithms.**
- **optimization of amplifier setups using chirp management with custom photonic crystal fibers delivering the seed pulse, as well as with available dispersion compensating silica single mode fibers with the criterion of maximum amplified pulse compression.**
- **experimental evaluation of noise properties and assignment of main contributions to relative intensity noise characteristics of amplified pulses in coherent seeding of a single amplifier, as well as in simultaneous seeding of two amplifiers.**

The thesis of the dissertation is that utilizing coherent, polarized supercontinuum pulses as seed signals in thulium-doped or erbium-doped amplifier systems or their simultaneously seeded tandems, enables:

a) post-amplification temporal compression down to around 100 fs using available single mode or polarization maintaining fibers,

b) significantly reduced relative intensity noise characteristics, compared to state-of-the-art soliton-driven ultrafast fiber amplifier systems,

c) nonlinear mixing of a tandem of ultrafast fiber amplifiers, seeded from a common coherent signal, with the relative intensity noise of the mixing product not exceeding the level of state-of-the-art ultrafast fiber amplifiers.

This thesis is organized as follows:

- Chapter 2 gives a theoretical background and introduces the basic concepts underpinning the thesis. Basics of optical fibers, gain fibers, supercontinuum generation in PCF, and femtosecond laser pulse characterization techniques and pulse retrieval methods are covered.
- Chapter 3 covers broadband dispersion and birefringence measurements and discusses the results of measurements of these characteristics in commercially available ultra-high numerical aperture fibers commonly used in chirp management in ultrafast fiber-based systems, as well as in custom nonlinear PM ANDi PCFs exploited in this work for seed signal generation.
- Chapter 4 describes an experimental investigation of spectro-temporal characteristics of coherent supercontinuum (SC) pulses generated in several implementations of silica and soft-glass all-normal dispersion (ANDi) photonic crystal fibers optimized for pumping with Erbium (Er): fiber femtosecond lasers. These fibers and the coherent supercontinuum seed signals are subsequently employed in ultrafast fiber amplifiers covered in Chapters 5 and 6. Here the discussion relates to the fine structure of the supercontinuum seed signal and its relation to spectro-temporal characteristics of the front-end, Er-fiber femtosecond driving laser.
- Chapter 5 covers the development of ultra-low noise, polarization-maintaining, ultrafast thulium-doped all-fiber chirped-pulse amplifier. The polarized all-normal dispersion (ANDi) supercontinuum (SC) discussed in chapter 4 is used as a seed source and the system driven by an ultrafast Erbium-fiber laser. The system comprises only polarization-maintaining fibers and delivers 96 fs pulses with 350 mW output power at 100 MHz, centered at 1900 nm. The RIN measured at the developed amplifier's output is found an order of magnitude lower than similar systems previously seeded with Raman solitons. This highlights the superior noise properties of ANDi SC and their potential as ultra-low noise seed sources for broadband, high power ultrafast fiber amplifiers, and frequency combs.
- Chapter 6 demonstrates the simultaneous and coherent seeding of the Tm and Er-doped fiber amplifiers. The system is based on FCPA enables the realization of linear pulse amplification in an all-fiber, all PM-architecture. Improved SC with better PER and

average power is used, compared to work in Chapter 5. From the Tm amplifier, I obtained 580 mW of average output power, 3 dB bandwidth of 100 nm centered at 1880 nm, which was compressed in a single-mode fiber to 120 fs. Er-doped fiber amplifier system delivered 220 mW of average output power centered at 1555 nm with a 3 dB bandwidth of 64 nm and compressed to 56 fs. The average output power was limited, compared to the Tm-amplifier, by the available amplifier pump power. The RIN of the Tm amplifier was virtually identical to the RIN of the Erbium-fiber laser, while the SC seed Er amplifier was RIN 1.4 times higher. The chapter also summarizes the results of the sum-frequency signal generation (SFG) between the group velocity-matched outputs of the two amplifiers, which are intrinsically synchronized by seeding with the same seed signal. The measured RIN of the SFG signal was 1.47 %, mainly shaped by the Er-amplifier noise.

- Chapter 7 concludes the dissertation and also draws an outline for further work.

Key achievements

- Broadband dispersion measurements in commercial Ultra-high numerical aperture (UHNA) fibers and all solid PM ANDi PCFs.
- Spectro-temporal characteristics of coherent SC pulses generated in several implementations of silica and soft-glass PM and non-PM ANDi PCFs. Relation of femtosecond pump pulse characteristics to sub-25 fs fine structure of coherent supercontinuum pulses.
- Achieving an order of magnitude lower relative intensity noise in a sub-100 fs Tm-doped fiber amplifier, seeded with coherent supercontinuum, compared to systems with similar output parameters, but seeded with solitonic signals.
- Demonstration of simultaneous and coherent seeding of the Tm and Er-doped fiber amplifiers intrinsically synchronized by common, wavelength-demultiplexed seed signal, subsequent sum-frequency signal generation, and confirmation of low relative intensity noise level inherent to highly coherent operation.

Contributions and acknowledgments

The author is responsible for all the work presented in this dissertation.

For work presented in Chapter 3, I have been helped by Dr. Piotr Ciąćka who built the dispersion measurement setup (Mach-Zehnder interferometer), which I have later adjusted to requirements of nonlinear PCF characterization. I along with Dr. Piotr Ciąćka performed the experiments and analyzed the results on ultra-high numerical aperture (UHNA) series of fibers. These results were published in our joint paper "Dispersion measurement of ultra-high numerical aperture fibers covering thulium, holmium, and erbium emission wavelengths" in the Journal of Optical Society of America B [70]. The PM ANDI PCFs were designed by Mr. Dominik Dobrakowski, who also provided me with dispersion and birefringence results obtained numerically for comparison with my results obtained experimentally in the scope of this work. Nonlinear ANDi PCFs were fabricated at the Institute of Electronic Materials Technology by Mr. Dariusz Pysz. Dr. Grzegorz Stępniewski assisted me during PM ANDi PCF dispersion measurements.

Chapter 4: XFROG setup was initially built by my adviser Dr. hab. Mariusz Klimczak. Later I modified and updated it according to the requirements of measurements of pulses with octave-spanning spectra and carried out all the experimental measurements under the supervision of my adviser. Silica/Ge:silica core PM PCFs were provided by Dr. Karol Tarnowski and Dr. Tadeusz Martynkien from Wrocław University of Science and Technology. These fibers were developed by Dr. Paweł Mergo at the Laboratory of Optical Fiber Technology, Maria Curie-Sklodowska University in Lublin, Poland. Dr. Dirk Mathys Spangenberg performed the time-domain ptychography retrieval on my experimental results of the XFROG characterization of coherent SC pulses. Prof. Dr. Alexander M. Heidt performed a numerical simulation of nonlinear propagation in the ANDi PCFs using my experimental data on the femtosecond erbium laser pulse properties. This enabled me to identify the influence of femtosecond laser pump pulse characteristics on the spectro-temporal fine structure of the coherent ANDi seed pulses, which is described in chapter 4. All the results were discussed with Prof. Dr. Alexander M. Heidt, Dr. Dirk Mathys Spangenberg, Prof. Thomas Feurer, and Dr. hab. Mariusz Klimczak.

I designed and built the complete experimental setups and performed characterization of the amplifiers under the supervision of Dr hab. Mariusz Klimczak and Dr. hab. Yuriy Stepanenko.

The results of this work are described in chapters 5 and 6. Dr. Tomasz Kardaś helped in optimizing the length of fiber through numerical simulations. Telluride PM ANDi PCF was designed by Ms. Tanvi Karpate in the scope of the H2020 MSCA ITN SUPUVIR project and Mr. Dariusz Pysz fabricated the fiber. Dr. hab. Mariusz Klimczak and Prof. Dr. Alexander M. Heidt helped in the discussion of results along with Dr. hab. Yuriy Stepanenko.

All the work presented in this thesis has been supported by the First TEAM programme of the Foundation for Polish Science co-financed by the EU under the European Regional Development Fund (project number First TEAM/2016-1/1 - POIR.04.04.00-00-1D64/16-00) and Schlumberger Foundation Faculty for the Future program, of which I was a fellow through most of my PhD.

Chapter 2. Theoretical and Technological Background

In this chapter, I introduce the theoretical and technological background related to understanding the work presented in my dissertation. First, I briefly discuss the basics of conventional passive and active optical fibers. Next, I describe the energy level transitions in Yb, Er, and Tm active fibers. The important fiber parameter – chromatic dispersion – will be discussed in detail. The concept of photonic crystal fiber and mathematical description of nonlinear propagation in fiber using generalized nonlinear Schrödinger equation (GNLSE) will be presented next. Supercontinuum (SC) generation will be discussed on the basics of certain nonlinear dynamics in different operational regimes. Principles of ultrashort pulses characterization techniques such as FROG and XFROG setup, and pulse retrieval techniques are explained, as well. In the end, I addressed the relative intensity noise measurement technique used in this work.

2.1 Optical fiber theory

Conventional step-index optical fibers consist of higher refractive index (RI) core (n_{core}), lower RI cladding (n_{clad}) and outer polymer buffer layer. Light in such fibers propagates as a result of total internal reflection - a phenomenon which was demonstrated in the 19th century [71,72]. These fibers are characterized by defining a so-called V parameter that determines the number of modes supported by the fibers, defined as

$$V = \frac{2\pi a}{\lambda} NA, \qquad (2.1)$$

and

$$NA = \sqrt{n_{core}^2 - n_{clad}^2}, \qquad (2.2)$$

where a is the core radius, and λ is the wavelength of light and NA is the numerical aperture of the fiber. If V < 2.405, the step-index fibers can support the single-mode and are called single-mode fibers (SMF). It is important to note, that the V parameter given with eq. (2.1) and the V <2.405 single mode condition are valid for step-index silica fibers, while for soft glass and photonic crystal fibers this approximation should be used with care. With the rapid development of fiber fabrication technology, optical fibers with very low scattering losses and low impurity losses have been achieved. Owing to its low attenuation and high transmission capacity, optical fibers have revolutionized telecommunications. In addition, optical fibers have been recognized in the field of scientific research for their excellent properties as a gain medium by doping with rare-earth elements such as Neodymium (Nd), Ytterbium (Yb), Erbium (Er) and Thulium (Tm).

2.2 Active optical fiber

Optical fibers containing intentionally introduced, optically active impurities have made their way to the research laboratories and industry in the development of lasers and fiber-based systems. Especially, fiber devices in the near-infrared region, ranging from 0.8 μm to 2.2 μm, have attracted attention due to their wide range of applications, such as optical communications (the erbium fiber amplifier EDFA) [73], micromachining [74], spectroscopy [75], and imaging [76]. The near-infrared emission in fiber devices could be realized by doping with rare-earth elements. Among the rare-earth dopants in active fibers, the trivalent ions Yb^{3+}, Er^{3+}, and Tm^{3+} are the most successful ones incorporated in optical fibers. For further extension of spectral bandwidth in the NIR region, Tm^{3+} is co-doped with trivalent holmium Ho^{3+}. The low loss and high reliability of silica glasses have impacted as host materials for rare-earth materials in the 1 - 2.2 μm wavelength region. Furthermore, it is difficult to extend the emission wavelength due to the high loss in a silica host beyond this wavelength range.

Optical fibers doped with rare-earth ions exhibit several advantages over bulk solid gain medium: (i) Enhanced beam quality results from the good confinement of light in the fiber core. (ii) The large surface-to-volume ratio of optical fiber allows efficient heat dissipation, enabling thermal management for power scaling. (iii) The complicated alignment of optical components in free space could be avoided by all-fiberized architecture. The characteristics of optical fibers boost their wide range applications as a gain medium in lasers and amplifiers.

2.2.1 Ytterbium Doped Fiber

Among all the active fibers, the Yb-doped fiber has matured quite over the last decade. Simple two-energy level structure with large Stark-splitting allows efficient quasi-three level schemes of operation and negligible excited state absorption. Yb systems comprise of $^2F_{5/2}$ excited state, and

$^2F_{7/2}$ ground state, as shown in figure 2.1. The small quantum defect (compared to other rare-earth dopants) potentially promotes high power operation due to a very low energy difference between the pump photon and the emission photon. Moreover, Yb ions possess a broadband absorption spectrum spanning from ~850 nm to ~1080 nm. Together with high-brightness pump sources, efficient lasing is observed in ~1000 nm to ~1100 nm range. As a result, the high quantum efficiency with the available pump sources enables Yb doped fiber laser power level above multi-kW with near-diffraction-limited beam quality.

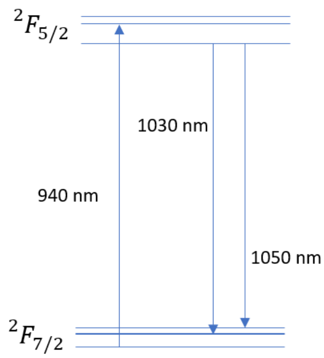

Figure 2.1 Schematic of the energy level diagram of ytterbium ions and possible transitions.

2.2.2 Erbium Doped Fiber

Erbium-doped fiber lasers and amplifiers are important in context of long-range optical fiber communications. Er-doped fiber has an emission band spanning from around 1480 nm to 1620 nm and can efficiently amplify in the 1550 nm wavelength region, where standard SMFs have minimum loss. The 4f energy level scheme of trivalent erbium is silica glass is as shown in figure 2.2. The relaxation time of the $^4I_{13/2}$ energy level is long (in the ms range) enabling efficient laser action even in the three-level scheme.

The Er ion has two strong absorption lines at 980 nm (available from mature laser diode technology) and 1480 nm (bringing in the benefit of decreased excited state absorption cross-section, compared to 980 nm pumping), and these two wavelengths are used for most of the Er-doped lasers and amplifiers. The transition between $^4I_{13/2}$ and $^4I_{15/2}$ energy levels covers an emission band over 50 nm wide around the wavelength 1550 nm, due to large splitting of the terminal $^4I_{15/2}$ level.

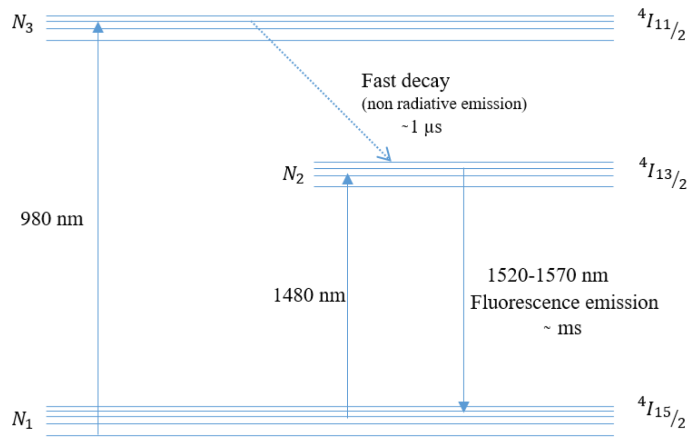

Figure 2.2 Schematic of the energy level diagram of erbium in an approximation of a three-level system with possible pump and lasing wavelengths. Two pump wavelengths around 980 nm and 1480 nm can be used to emit light around 1550 nm.

2.2.3 Thulium Doped Fiber

Tm^{3+} is another popular dopant that provides high optical gain and extends the emission wavelength into the long-wave near-infrared around the wavelength of 2 µm. Tm^{3+} ions energy-level structure with simplified four-level system with the possible fluorescent transition in a Tm^{3+}doped optical material is shown in figure 2.3. The transition between $^3H_4 \rightarrow {}^3H_6$ energy states occur when pumped around 1.56 µm has a broadband emission span from 1.8 µm to 2 µm, offers a wide gain bandwidth for amplifiers and lasers. The gain bandwidth of the Tm doped fiber ranges from 1.7 – 2.1 µm, which can support short, high peak power pulses around 1.9-2 µm. This spectral bandwidth can be extended to the longer wavelengths up to about 2.2 µm when the Ho^{3+} ion is co-doped with Tm^{3+}.

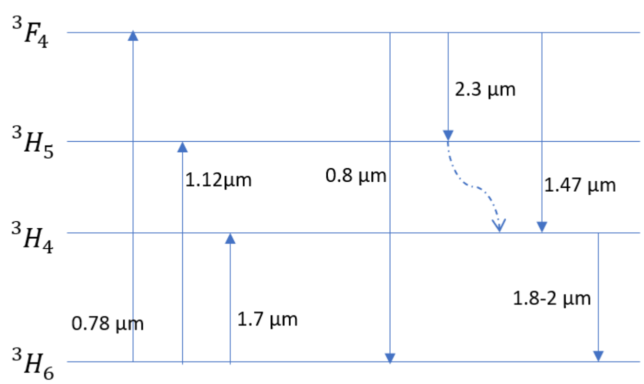

Figure 2.3 Schematic of the energy level diagram of thulium ions in a dielectric optical material host with possible pump and lasing wavelengths.

In addition, conventional optical fibers have strict design limitations: limited choice of materials for fabrication, strict modal cut-off wavelength, the limited core diameter to achieve single-mode operation, and most importantly, very narrow fiber dispersion variation limits [77]. These limitations encouraged researchers to look for alternative light-guiding methods in optical fibers, that gave birth to photonic crystal fibers which will be discussed in the next sections.

2.3 Dispersion

Chromatic dispersion is one of the most important features of the optical fiber in telecommunications, as well as in ultrafast optics systems. When light travels through a dielectric medium it experiences a group delay which causes broadening of pulses traveling through the medium [78]. Group delay T_g is a frequency (ω) dependent quantity which is defined as

$$T_g = \frac{\partial \varphi}{\partial \omega}, \tag{2.3}$$

where φ is a spectral phase of the pulse. Furthermore, the frequency dependence of group delay is called group delay dispersion (GDD) defined as:

$$GDD = \frac{\partial T_g}{\partial \omega}, \tag{2.4}$$

The GDD per unit length gives the group velocity dispersion (GVD).

The GVD plays an important role in the pulse propagation in the optical fiber since each frequency component travels with different speeds due to frequency-dependent RI. The wave propagation constant $\beta(\omega)$ is used to derive the dispersion coefficient and expanded in a Taylor series about the pulse central angular frequency ω_0 as

$$\beta(\omega) = \beta_0 + \beta_1(\omega - \omega_0) + \frac{1}{2}\beta_2(\omega - \omega_0)^2 + \frac{1}{6}\beta_3(\omega - \omega_0)^3 + \cdots \tag{2.5}$$

Where propagation constant is $\beta(\omega) = \frac{\omega n(\omega)}{c}$, $\beta_0 = \frac{\beta}{\omega_0}$, which is $\frac{1}{v_p}$, $\beta_1 = \left(\frac{\partial \beta(\omega)}{\partial \omega}\right)_{\omega=\omega_0}$, which is $\frac{1}{v_g}$, $\beta_2 = \left(\frac{\partial^2 \beta(\omega)}{\partial \omega^2}\right)_{\omega=\omega_0}$ is GVD and $\beta_3 = \left(\frac{\partial^3 \beta(\omega)}{\partial \omega^3}\right)_{\omega=\omega_0}$ is third-order dispersion (TOD) describes the dispersion slope, and so on. Higher-order dispersion is crucial when using extremely short pulses and pumping close to the ZDW.

Dispersion is usually described with the "dispersion parameter" D which is commonly expressed in ps/nm/km in the fiber telecommunications community. It describes how a pulse with a given spectral width (in nm) will have spread in time (in ps) after it has propagated along a certain length (in km) of fiber, and is given by [79].

$$D = \frac{d\beta_1}{d\lambda} = -\frac{2\pi c}{\lambda^2}\beta_2 = -\frac{\lambda}{c}\frac{d^2 n}{d\lambda^2} \qquad (2.6)$$

where λ is the wavelength, c is the speed of light in vacuum

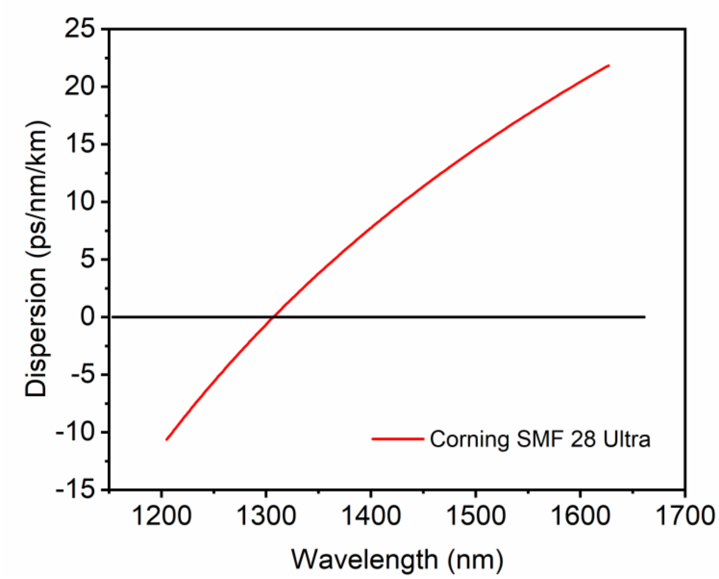

Figure 2.4 Dispersion of Corning SMF-28 was computed using the manufacturer's product information [80].

D and GVD have opposite signs to each other. The D parameter for commercial SMF 28 from Corning was computed using product information [80] and then plotted with respect to wavelength as shown in figure 2.4. The wavelength points where D vanishes is called ZDW (1310 nm for SMF 28), where the pulse can propagate without changing in its shape. When $D > 0$ ($\beta_2 < 0$), it is called "anomalous" and when $D < 0$ ($\beta_2 > 0$), it is called "normal", and this is the terminology used throughout this thesis. In the normal dispersion regime, higher frequencies have a lower group velocity than lower frequencies, and the opposite is true in the anomalous dispersion regime.

When pulse propagates in the fiber it undergoes dispersion and is chirped, which means that it has a time-dependent instantaneous frequency. But when a pulse has no chirp, its duration is the shortest as its spectral bandwidth permits and such a pulse is called transform-limited. The transform-limited temporal pulse profile is obtained by taking the Fourier transform of the pulse spectrum, with a flat spectral phase. Transform-limited pulses will broaden in time when traveling through a dispersive medium, while chirped pulses can be compressed or broadened in time depending on the sign of the dispersion of the medium, in which they propagate. The time-bandwidth product (TBP) can be used to find out if a pulse is transform-limited or chirped. It is the product of the pulse temporal full-width half-maximum (FWHM), and the spectral bandwidth in frequency. The TBP for a transform-limited $sech^2$ pulse is 0.315, and for a Gaussian pulse is 0.441.

2.4 Photonic crystal fibers

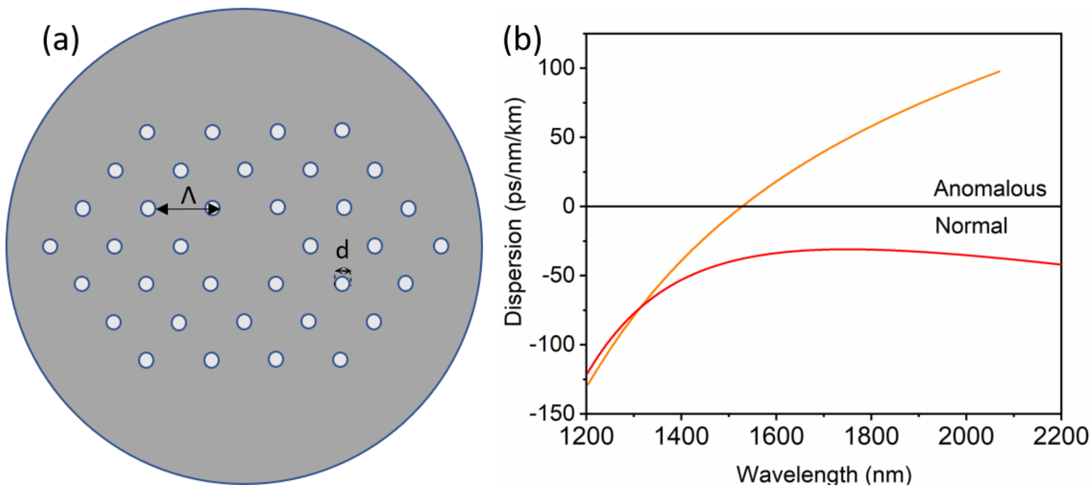

Figure 2.5 (a) Illustration of a typical hexagonal PCF. The two important parameters, pitch and hole size, are marked with Λ and d respectively in the figure. (b) Example of dispersion curve which can be obtained by modifying pitch and hole size.

The fundamental advantage of the PCF is that it offers wide freedom of engineering of the dispersion profile as shown in figure 2.5 (b), as well as mode and nonlinear properties, compared to classic, step index fibers. Over the last decade, many different PCFs have been designed to generate supercontinuum (SC). The basic design is a solid silica core surrounded by a cladding of air holes, mostly arranged in a hexagonal lattice structure shown in figure 2.5 (a). Great progress has been made in terms of design and nonlinear RI material to extend the adaptation to specific pump sources and the tailoring of the generated SC properties to specific applications, either in SC generation and its further uses [81] or in new light sources operating at exotic wavelengths [82,83] In the case of small core diameters, the PCF cladding has a significant influence on the waveguide dispersion, which is added to the material dispersion of silica to yield the total fiber dispersion profile. The basic optimization of the geometric parameters in a regular hexagonal air-hole PCF lattice includes the pitch Λ, different size of air holes d/Λ and the number of rings. With this freedom, the position of ZDW can be controlled and dispersion can be shifted e.g. entirely to normal dispersion in a broad wavelength range. In the presence of nonlinearity, the sign of the GVD becomes an important factor and determines the effects of spectral and temporal broadening dynamics [79].

PCF dispersion plays a central role in determining pulse propagation dynamics and SC spectrum formation [29,54]. It is therefore of paramount importance to be able to estimate dispersion accurately and reliably.

2.4.1 GNLSE

To understand the basics of SC generation, GNLSE and NLSE are very necessary. The derivation of equations and terms used in my dissertation was taken after established textbooks and literature [54,79,84]. The general version of the equation is represented as below

$$\frac{A(z,t)}{\partial z} = i\sum_{m\leq 1}\frac{i^m\beta_m}{m!}\frac{\partial A(t,z)}{\partial t} - \frac{\alpha}{2}A(z,t) + i\gamma\left(1 + i\tau_{shock}\frac{\partial}{\partial t}\right)\left(A(z,t)\int_{-\infty}^{\infty}R(t')\,|A(z,t-t')|^2dt'\right) \tag{2.7}$$

where A(z, t) is the complex pulse envelope, α is the loss β_m is dispersion coefficients, τ_{shock} is the shock time, R(t) is the full material response, the term defined as

$$\gamma = \frac{\eta_2\,\omega_0}{cA_{eff}(\omega_0)}, \tag{2.8}$$

is the effective nonlinear coefficient, η_2 is nonlinear RI and $A_{eff}(\omega_0)$ is the effective mode field area – in this case - of the nonlinear fiber. The first term in on the right-hand side of the equation (2.7) describes the contribution of dispersion, the second term is loss, and the last groups the nonlinear effects. By excluding the delayed Raman contribution, and neglecting both the frequency dependency in the self-steepening term by setting τ_{shock} = 0 and the loss, we arrive at the NLSE,

$$\frac{A(z,t)}{\partial z} = i\sum_{m\leq 1}\frac{i^m\beta_m}{m!}\frac{\partial A(t,z)}{\partial t} - \frac{\alpha}{2} + i\gamma A(z,t)\int_{-\infty}^{\infty} R(t')\,|A(z,t-t')|^2 dt' \quad (2.9)$$

The dispersion length L_D is defined as a length scale over which dispersion becomes an important factor for pulse evolution and is given by

$$L_D = \frac{T_0^2}{|\beta_2|} \quad (2.10)$$

Where T_0 is the initial pulse width at 1/e intensity. When a transform-limited Gaussian pulse propagates by length L_D the pulse is broadened by a factor of $\sqrt{2}$ due to dispersion.

The nonlinear length in the fiber can be defined as the effective propagation distance of the fiber over which the nonlinear phase shift becomes 1 radian

$$L_{NL} = \frac{1}{\gamma P_p}, \quad (2.11)$$

where P_P is the peak power of the pulse.

2.5 Physical mechanisms

There are many ways to generate SC depending on the dispersion of fiber and pump parameters. Figure 2.6 shows a schematic overview of the different regimes and the effects that lead to SC generation.

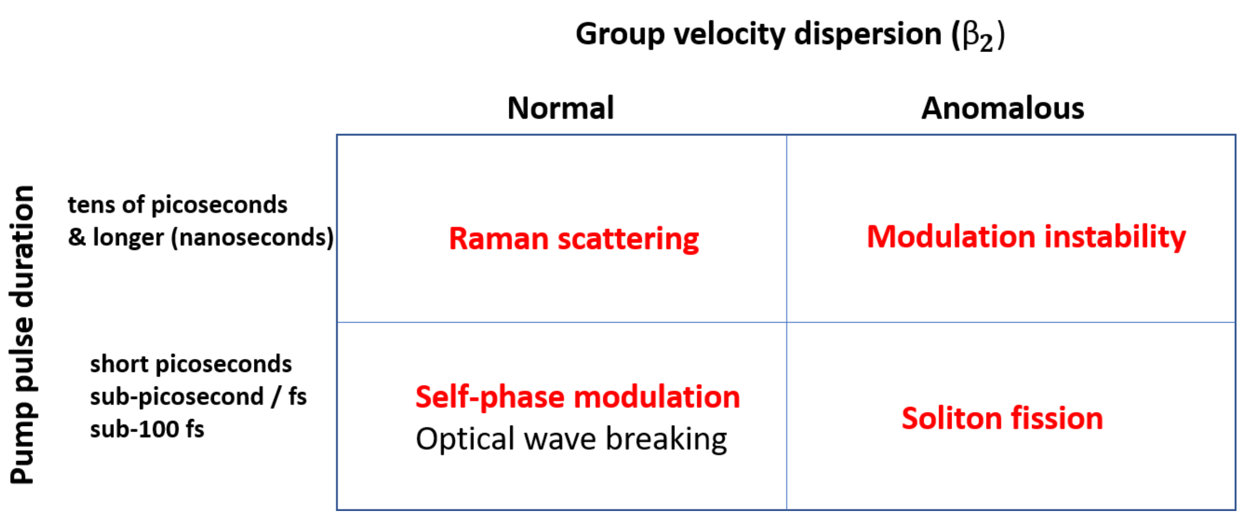

Figure 2.6 Illustration of the different effects that can generate an SC depending on pulse duration and dispersion. It assumes the peak power of the pump pulse is high enough, and the fiber is long enough to allow for sufficient nonlinear interaction.

2.5.1 Self-phase modulation

Self-phase modulation (SPM) stems from the intensity-dependent RI and leads to a spectral broadening of optical pulses [85]. By inspecting equation 2.9, we can study SPM broadening. It can be seen that the nonlinear term introduces a time-dependent phase change and consequently time-dependent instantaneous frequency, thus creating new frequencies. In a normal dispersion regime, at the central frequency, light with longer wavelengths (red-shifted) are produced on the leading edge of the pulse and has larger group velocity, so it moves away from the pulses. The short-wavelength (blue-shifted) light is produced on the pulse trailing edge and moves away from the central part of the pulse as well. This is demonstrated in figure 2.7, with the pulse group delay profile (spectrogram) exhibiting the typical S-shape with a red-shift feature on the leading and a blue-shift on the trailing edge of the pulse. The spectrum shows the oscillatory structure associated with SPM, which is generated by spectral interference of the same spectral components being present at different temporal positions within the pulse.

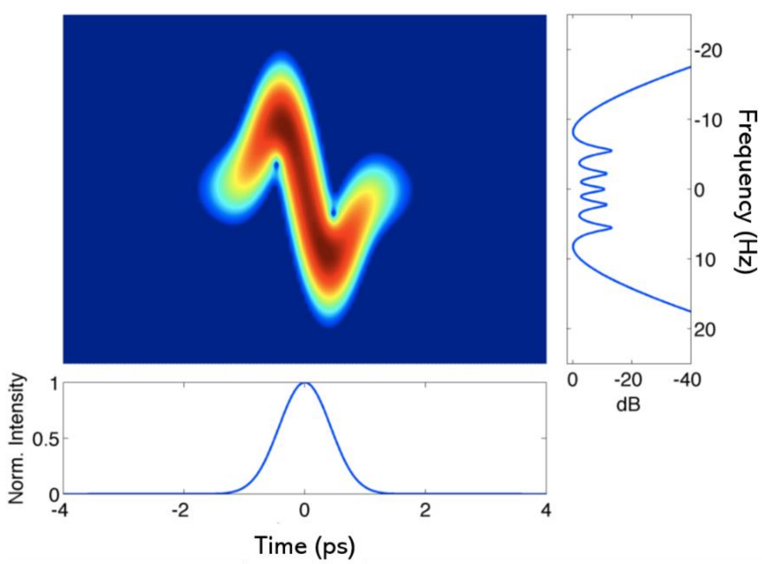

Figure 2.7 Spectrogram of SPM induced spectral broadening

The further propagation of pulse in the fiber involves the dynamics governed by the dispersion profile. In a situation, when the fiber has normal chromatic dispersions at all wavelengths in its transmission window, the blue-shifted wavelength components produced by SPM experience higher GVD in the pulse's intermediate trailing section than the pulse's center frequency, and thus travel slower than the pulse tail. Eventually, the faster tail overtakes the slower intermediate section, leading to the steepening of the trailing pulse edge and the onset of optical wave breaking (OWB). Upon completion of this process, the pulse becomes smooth. These smooth spectrograms can be compressed to obtain few-cycle time-bandwidth limited pulses, much shorter than the initial pulse [67]. Such a scenario is however usually unfeasible, because even small imperfections of the initial pulse (such as post- and pre-pulses or temporal pedestals) introduce significant temporal and spectral structure into normal dispersion-broadened ultrashort pulses, as discussed with my research results in Chapter 4 of this dissertation.

2.5.2 Soliton dynamics

In the anomalous dispersion regime, we can observe a range of nonlinear dynamics. The most important of them all related to soliton formation and propagation. For certain peak power values, the nonlinear positive chirp due to SPM can balance negative linear chirp due to anomalous GVD of the fiber, and solitons are formed. Solitons are solutions that correspond to a pulse that does not change its shape upon propagation. A soliton solution for the initially injected pulses is written as [54]: $A(t) = N \sec h\ (t/t_0)$, where t_0 is the pulse width, and N is the soliton number. It is determined by both pulse, and fiber parameters through $N^2 = L_D/L_{NL}$, which is a balance between dispersive and nonlinear length scales. The Soliton number depends on both fiber and pump pulse parameters. During propagation, both temporal and spectral profiles remain unchanged for the fundamental soliton with N = 1. Solitons with higher-order N > 1 undergo a periodic spectral and temporal changes. In general, the temporal and spectral evolution of higher-order solitons can be very complicated, in particular where nonequilibrium conditions are considered including contributions of higher order dispersion terms, such as in GNLSE.

2.5.3 Soliton fission, self-frequency-shift, and dispersive wave generation.

In real fibers, the soliton formation process is perturbed due to the presence of higher-order dispersion and Raman scattering. This results in the breakup of higher-order solitons into a train of fundamental solitons. The fundamental solitons are ejected one by one, the ones ejected first have the highest amplitude and shortest duration [86]. This break-up is called soliton fission and the characteristic fission length is proportional to soliton number and fiber dispersive length $L_{fiss} \approx L_D/N$. After the soliton fission, each individual fundamental soliton experiences a shift to lower frequencies (longer wavelengths) due to the soliton self-frequency shift caused by intra-pulse

Raman scattering [87]. The dynamics of the frequency shift ν_R can be defined as $\frac{d\nu_R}{dz} \propto \frac{|\beta_2|}{t_0^4}$ [88], which leads to a stronger shift from the fission process for the first ejected soliton and thus to an increasing separation between the individual solitons with propagation distance. Additionally, higher-order dispersion leads to an energy transfer from the solitons to a resonance band in the normal GVD, which is called the dispersive wave (DW). Its location can be determined from a phase-matching argument [89].

2.5.4 Modulation instability

Modulation instability (MI) is a nonlinear effect that occurs due to instability of the nonlinear system resulting from the interplay between nonlinear and dispersive effects. Numerical studies suggests that pump pulse envelope is rapidly modulated during SC generation in case of longer (picosecond, nanosecond) pulses and even CW radiation and this can induce pulse fission into soliton-like sub-pulses followed by self-frequency shift and DW generation [90–92]. In the frequency domain, MI corresponds to the generation of sidebands symmetrically placed about the pump frequency component followed by the self-frequency shift and dispersive wave generation [93]. In the time-domain it corresponds to rapid modulation of pump pulse temporal envelope and eventually, the pulse breaks up into a sequence of soliton-like sub-pulses [79,94]. The characteristic period of MI oscillations is much shorter than the fission length of the pump pulse, so the duration of the sub-pulses is significantly shorter than the pump pulse duration. It is expressed as [79]:

$$T_{MI} = \sqrt{\frac{2\pi^2|GVD|}{\gamma P_p}} \tag{2.12}$$

This is typically tens or hundreds of femtoseconds [29]. Efficient spectrum broadening occurs in the anomalous dispersion region when the pump wavelength is close to ZDW: smaller group velocity mismatch means longer temporal interaction length. A crucial feature of the resulting spectrum broadening is noise-based origin which suggests that there is very little phase stability from shot to shot [95]. MI is possible in the normal GVD regime also, but it is limited to some special cases [96–101]. For conventional MI while solving the NLSE equation by Taylor expansion of the propagation constant only up to second-order term is taken into account. While for the MI in the normal GVD regime, the primary important higher-order term is the fourth-order dispersion term.

2.5.5 Raman scattering

Another important process in SC generation with pumping from with pulses of tens of picoseconds durations in the normal GVD regime is stimulated Raman scattering (SRS). In general, Raman scattering is a phenomenon when the incident photon with a frequency ω_1 is absorbed in the medium and a lower frequency photon ω_2 is emitted due to interaction with intrinsic vibrations of the medium called phonons. The difference in frequencies $\omega_s = \omega_1 - \omega_2$ is called the Stokes shift. When the intensity of incident light is very high the generated lower frequency wave is subsequently amplified and this is called stimulated Raman scattering (SRS) [79]. It has been shown that noise seeded SRS and FWM limit the coherence of normal dispersion SC generation across the whole spectrum [65]. The process is a combination of the regular Raman process, where light is generated at lower energy compared to the pump, and a second step in which it then spreads to other wavelengths by spectrally mixing through four-wave mixing. It is argued that this noise process can be suppressed when the dispersion is close to zero, or if short initial pulses are used.

Another type of SRS important in this discussion is cascaded SRS. This process can be explained as follows. When the efficiency of SRS is very high, the amplification of the Stokes-shifted wave is eventually saturated, and the initial pump wave is depleted. At this moment the Stokes-shifted wave becomes a new pump and a new wave with double Stokes shift is generated. The process repeats itself until the amplification of newly generated Stokes-shifted waves is saturated.

2.5.6 Four-wave mixing

Soliton formation and related nonlinear dynamics phenomena are the key processes to SC formation when pump wavelength is in the anomalous dispersion range of the PCF. In the case of normal GVD range, soliton formation does not occur and spectrum expansion in related to the SPM and OBW and later due to a nonlinear process called four-wave mixing (FWM) and SRS [65]. It is a nonlinear phenomenon arising in optical media with third-order nonlinear optical susceptibility when two waves with frequencies ω_1 and $\omega_1$interact and two additional frequency components $\omega_3 = \omega_1 - (\omega_2 - \omega_1))$ and $\omega_4 = \omega_2 + (\omega_2 - \omega_1))$ are generated as a result. In general, a degenerate case is possible when two initial waves have the same frequency [54].

It has been shown that long pump pulses and long fiber lengths lead to coherence collapse in SC generation due to the occurrence of SRS and FWM in normal dispersion fibers [29,65]. It has further been shown that solitons and dispersive waves can also interact via FWM if phase-matching conditions are satisfied resulting in additional SC spectrum broadening [102–105].

2.5.7 Polarization modulational instability

Another important process is polarization modulational instability (PMI) it is a form of MI that affects the polarization state of light that propagates through the fiber [38,79,106,107]. PMI can exist in weakly birefringent fibers; the effect occurs when one of the linear axes (fast or slow) of the birefringent fiber is excited with a high-intensity pump signal. The polarization state of the generated PMI is orthogonal to the polarization state of the pump. It is important to note that PMI is not a phenomenon limited to normal dispersion fibers but also occurs in anomalous dispersion fibers in addition to other noise amplifying effects [106]. In the case of weakly birefringent fibers, pumping in slow and fast axis differ. First, the PMI produces sidebands separated from the pump regardless of pump power. A low power threshold exists for PMI generation for fast axis pumping, the gain profile only shows sidebands at high pump powers detuned from the pump. The other option is to pump in the slow axis. In this case, there is no critical power, but instead the gain bands are located far from the pump, with the minimum frequency shift from the pump. This opens up for the possibility to push the gain bands outside the SC range by pumping in the slow axis [79].

The recent studies by Gonzalo et al. showed through experimental and numerical studies that the PMI noise can lead to spectral degradation of ANDi SC [41]. PMI assisted by the weak unintentional birefringence of the fibers has been identified as its origin [39]. The use of PM ANDi fibers has been proposed to avoid such limitations [42,43].

2.6 Pulse characterization

The complex nonlinear interactions in SC generation dynamics result not only in the extreme expansion of the pump laser pulse spectrum, but also significantly reshape its temporal profile. Apart from measuring the pulse spectrum (spectral-domain information) of SC with e.g. an optical spectrum analyzer (OSA), it is also important to obtain information in the time domain. SC pulses obtained for the purpose of my research, are generated under femtosecond laser pumping and typically do not exceed a dozen picoseconds of duration. Fast digital to analog-converters, i.e. P-I-N photodiodes have rise/fall times of 25 ps [108]. This is insufficient for accurate temporal characterization of laser pulses handled in this work. In the following subsections, I will briefly discuss principles of a widely used ultrashort pulse characterization techniques, which I used in the main part of my work – the frequency-resolved optical gating (FROG) and extension to cross-correlation FROG (XFROG).

2.6.1 Autocorrelation

The invention of autocorrelation to measure the pulse length was a very important development in the ultrafast optics community [109,110]. The basic principle of operation of an autocorrelator to characterize the pulse duration is to create the correlation of the temporal pulse trace with itself. A beam splitter is used to create the two copies of the incoming pulses. These copies are variably delayed with respect to one another and then superimposed in a nonlinear medium. A nonlinear optical signal will be generated provided that there is a temporal overlap in space and time, and the magnitude of the signal depends on the extent of this overlap. Next, the signal intensity is mapped as a function of relative time delay, from which an autocorrelation width is obtained. Assuming a gaussian and sech pulse shape, the actual pulse width is inferred. Mathematically, an second harmonic generated (SHG) autocorrelation trace is

$$I_{AC}(\tau) = \int_{-\infty}^{\infty} |E(t)E(t-\tau)|^2 dt \qquad (2.13)$$

The drawbacks are that for a measured autocorrelation trace, one can determine the pulse duration if the pulse shape is known. Additionally, it is difficult to uniquely measure the pulse shape with an autocorrelation trace alone. The reason is that the autocorrelation trace is always symmetric, even for asymmetric pulse shapes. Therefore, measurements of non-Fourier transform-limited pulses is approximate. Further, the autocorrelation technique cannot provide information on the phase profile.

2.6.2 FROG

The frequency-resolved optical gating (FROG) technique is a method for spectro-temporal characterization of optical pulses, yielding not only its intensity but also its phase. It was invented by R. Trebino and D. Kane in 1991 [111–114].

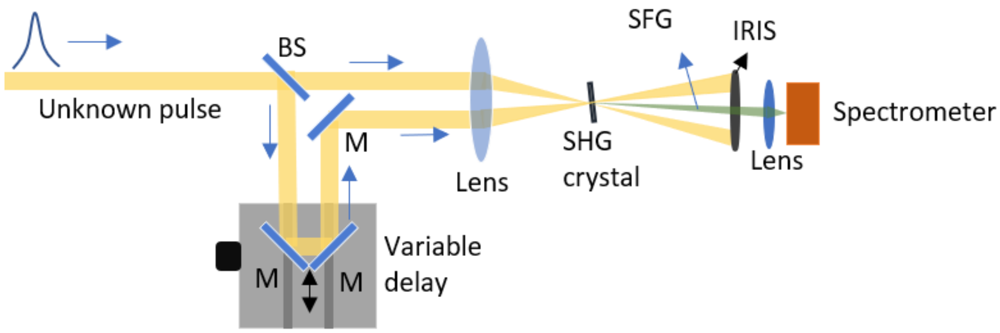

Figure 2.8. Example of experimental second harmonic generation FROG setup

From the experimental point of view, a FROG apparatus is only an autocorrelator, in which a photodiode detector is replaced with a spectrometer as shown in figure 2.8. Therefore, instead of just measuring the intensity of the nonlinear optical signal generated by the two variably delayed pulses, the signal is spectrally resolved into a delay-dependent spectrum. The resulting data is then a two-dimensional trace. If we use the second-harmonic generation (SHG) as the nonlinear optical process, SHG-FROG is the most commonly used FROG variant.

The SHG FROG trace is written as:

$$I_{FROG}(\tau,\omega) = \left|\int_{-\infty}^{\infty} E(t)E(t-\tau)e^{-i\omega t}dt\right|^2 \qquad (2.14)$$

$E(t-\tau)$ is known as the time gating function, producing a set of spectra of gated sections of $E(t)$ as the delay τ is varied. FROG was the first technique to experimentally record a pulse spectrogram, where the signal beam produced by a frequency-mixing autocorrelation is spectrally resolved [111–115].

The SHG-FROG technique has many practical advantages that make it preferable over other FROG variants. The optical arrangement introduces little material dispersion into the beam path and so is suitable for characterizing very short pulses; material dispersion introduced after the nonlinear crystal does not alter the measurement as it does not affect the spectral domain. As SHG is a $\chi^{(2)}$ process the measurement is also very sensitive.

One of the disadvantages of this technique is the introduction of ambiguities in the time domain. The pulse E(t) and its time-reversed conjugate E* (−t) both produce the same SHG-FROG trace. The trace is therefore symmetrical with respect to delay, and as a result, the sign of the higher-order phase terms cannot be determined.

There are several variants of FROG depending on the configuration. For example, we may use a variety of nonlinear optical processes in FROG, including second-harmonic generation (SHG) [116], polarization gating (PG) [112], self-diffraction (SD) [117], transient grating (TG) [118], etc. A huge variety of FROG versions make it more versatile, operable from UV to mid-IR, both single-shot [110] and multi-shot versions are available. A particularly important feature of FROG is that one of its versions cross-correlation FROG (XFROG) can be used to characterize even the most complex pulses, such as supercontinuum light pulses.

2.6.3 XFROG

Cross-correlation FROG (XFROG), first presented by S. Linden with colleagues in 1998 [119], uses a known reference pulse to characterize the investigated pulse. That is, instead of the same pulse acting as the gate and the test, two distinctly different pulses are used, such as two spectrally separate pulses or two spectrally identical pulses with different amounts of chirp. The principal experimental setup for XFROG measurements employing sum-frequency generation is shown in figure.2.9.

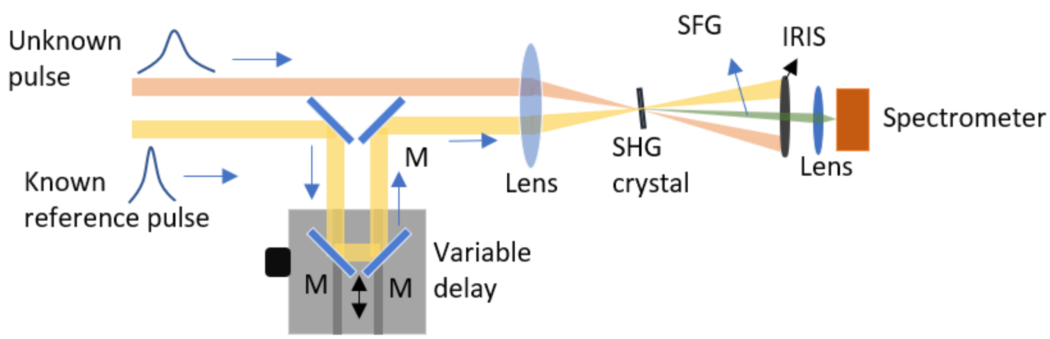

Figure 2.9. Example of experimental sum-frequency generation XFROG setup

Sum-frequency generation XFROG is in principle spectrally resolved cross-correlation. It is also important to note that other geometries such as difference-frequency generation (DFG) XFROG [120] and polarization-gate XFROG [121] have also been demonstrated. With the use of the right retrieval algorithm, both the test and gate pulses can be characterized by this technique.

XFROG has several advantages over conventional FROG techniques. First, a strong reference pulse correlated with a weak test pulse allows the characterizing of extremely weak pulses [122] making XFROG much more sensitive and reliable than SHG FROG. Besides, the XFROG technique does not require a spectral overlap between measured and reference pulses, unlike SHG FROG, hence it does not have time ambiguity. The other variant, DFG XFROG can be used to avoid problems related to the measurement of UV pulses. Therefore all these properties of XFROG enable us to successfully implement it in the investigation of complex pulses including SC pulses [114].

The first SC XFROG measurement was reported in 2001 [123], using a conventional optical fiber which was pumped by a 600 fs chirped-pulse Er-fiber amplifier. The broadband SC was generated from 880 nm – 2400 nm spectral range and was characterized by SFG XFROG measurements. Further, the issue of achieving extremely broad bandwidth was overcome by applying angle dithering technique [124]: that is by rapidly rotating the nonlinear crystal within a certain angular range one can achieve integrated phase-matching for the whole spectral range of SC over the signal integration time. The measured spectrum is an averaged value of many single-shot spectra each at different crystal angles which correspond to phase-matching for distinct spectral components of SC. Additionally, it has been pointed out that by analyzing XFROG traces of SC generated in conventional PCF using femtosecond pulses from Ti: sapphire laser helps intuitively reveal dispersive wave and Raman soliton components [125]. Further, it has been hypothesized that the observed fine spectral structure of SC may reflect single-shot spectra which cannot be directly observed due to "washing out" when averaging many spectra [30].

The XFROG analysis was further analyzed the temporal fine structure of SC which is in good agreement with GNLSE numerical simulations [126]. Similarly, the other studies confirmed that additional spectral broadening during SC generation is observed due to soliton and dispersive wave interaction [105,127]. In all mentioned reports after the first publication, Ti: sapphire laser was used as a pump source for SC generation in PCF, and the angle dithering method was applied to achieve sufficient phase-matching bandwidth. The XFROG setup has been employed for the investigation of SC generation in conventional tapered optical fibers [128,129]. The first experimental method for single-shot PG XFROG was demonstrated recently [130]. The adaptation of the pulse front tilt approach enabled PG XFROG measurements in single-shot mode. Besides, PG XFROG geometry has no phase-matching related problems which removed the need to use angle dithering.

2.7 Pulse retrieval

The general shape of the spectrogram from FROG or XFROG offers some indication of the level of the chirp of pulse, but a more thorough analysis is necessary for accurate characterization. Specifically, both FROG and XFROG are intensity measurements, in which phase information is lost. In autocorrelation, which is only time-resolved, there is no information on the phase, i.e. it is a one-dimensional phase problem, which is unsolvable. FROG and XFROG are spectrally resolved, in addition to being time-resolved, therefore the electric field information, and thus the phase information can be retrieved because it is a two-dimensional phase problem, which is solvable. Several algorithms exist for FROG and XFROG pulse retrieval and they can all be used simultaneously to achieve the most accurate results. The most reliable and easily available ones are referred to as the Generalized Projections algorithm (GP) [131] and time-domain ptychography (TDP) [132–134].

2.7.1 Generalized Projections algorithm of FROG retrieval

There exist several different FROG retrieval algorithms and the main task of the FROG algorithm is to retrieve the complex electric field E(t) of the pulse. The simple flow chart in figure 2.10 is based on the basic FROG algorithm which gives the overview of steps to retrieve a FROG trace [135].

The algorithm starts with a guess for the electric field E(t). The guess can be manually chosen to be either amplitude noise, phase noise, or both. The physical constraint is the mathematical form of the signal field produced when two pulses are combined in a nonlinear medium as described in section 2.62, given by

$$E_{sig}(t,\tau) = E(t)E(t-\tau) \tag{2.15}$$

where $E(t-\tau)$ is the delayed pulse. The FROG trace is the squared magnitude of the Fourier transform of this signal

$$I_{FROG}(\omega,\tau) = \left| \int_{-\infty}^{\infty} E_{sig}(t,\tau)\, e^{-i\omega t} dt \right|^2$$

$$= \left|E_{sig}(\omega,\tau)\right|^2 \qquad (2.16)$$

The next step in the iteration is applying the measured FROG trace to the calculated trace as

$$E'_{sig}(\omega,\tau) = \frac{E_{sig}(\omega,\tau)}{|E_{sig}(\omega,\tau)|}\sqrt{I_{FROG}(\omega,\tau)} \qquad (2.17)$$

Inverse fast Fourier transform of the new signal field is transferred back into the time domain. In order to complete the cycle, integration of the signal field in the time domain is performed along the delay axis, and one arrives back at the electric field E(t) and a new iteration can be started.

This basic FROG retrieval algorithm implementation suffered from drawbacks including predominantly the slow conversion for FROG traces with high complexity.

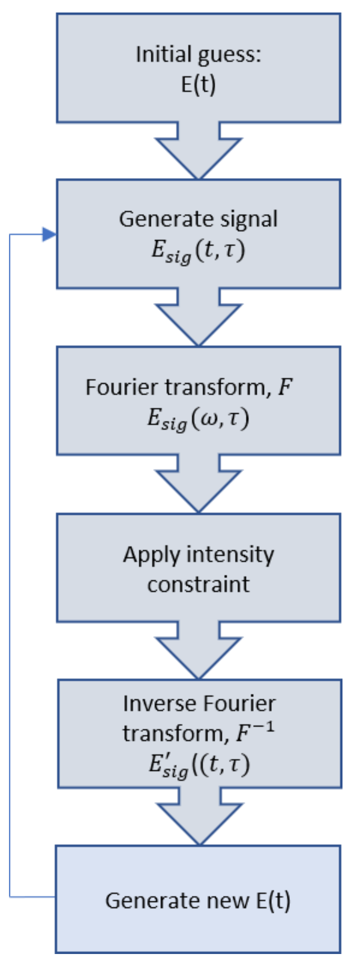

Figure.2.10. The flow chart of the basic FROG algorithm

The improved algorithm for FROG retrieval is based on generalized projections [131]. This iterative approach is motivated by the fact that when certain conditions are fulfilled it is known to converge. To find E(t) ($E_{sig}(t,\tau)$) one needs to satisfy two conditions. The first condition is the mathematical form, the ability to be generated by a known nonlinear-optical process from physically achievable signal field E(t) defined by equation 2.14. The second condition is that the squared magnitude of its Fourier transform corresponds to the FROG trace calculated experimentally defined by equation.2.15.

The algorithm is initiated by guessing the initial signal field and then determined by making projections onto one constraint and then moving to the closest point in another constraint. The process is continued until the point of convergence is reached. The convergence of the solution is guaranteed if the constraint sets are convex. When the constraint sets are not convex, a generalized projection must be defined which in most cases enables convergence. The mathematical form general projections algorithm which tries to find an electric field that minimizes the error metric, Z is defined as

$$Z = \sum_{i,j=1}^{N} \left| E'_{sig}\left(t_i, \tau_j\right) - \mathrm{E}(t_i)\mathrm{E}\left(t_i, \tau_j\right) \right|^2 \qquad (2.18)$$

Thereafter the step is the same as defined in figure 2.10. The accuracy of FROG analysis is evaluated by computing the FROG error which is the root-mean-square (rms) difference between the measured trace $I_{FROG}\left(\omega_i, \tau_j\right)$ and the computed trace $I_{cal}\left(\omega_i, \tau_j\right)$. It is expressed as

$$G = \sqrt{\frac{1}{N^2} \sum_{i,j=1}^{N} \left| I_{FROG}\left(\omega_i, \tau_j\right) - \alpha I_{cal}\left(\omega_i, \tau_j\right) \right|^2} \qquad (2.19)$$

where α is a real number that minimizes G.

2.7.2 Time-domain phytography for XFROG trace retrieval

Characterization of complex supercontinuum pulses requires high sensitivity, large ranges, and fine resolution in both temporal and spectral domains simultaneously. The accurate reconstruction of SC pulses with large TBP is achieved by XFROG which records a large number of time-gated spectra using short gate pulses. It requires a large number of points on time-frequency grids making the experimental measurement and the reconstruction rather cumbersome.

Recently a new retrieval algorithm was introduced for ultrafast pulse characterization called the time-domain ptychography (TDP) [132–134]. Original ptychography was used in lens-less spatial imaging microscopy and diffractive imaging based on a powerful phase retrieval algorithm, the ptychographic iterative engine (PIE) [136,137]. It offers several key advantages, especially relevant in the characterization of complex SC pulses:

(i) The PIE does not require an equally spaced grid in frequency and time. The computational grid size is orders of magnitudes smaller than what is used by many other reconstruction algorithms without compromising temporal resolution [136,137],

(ii) It can reconstruct temporal features much smaller than the probe pulse duration and the required time step needs to be in the order of half the temporal probe since information is encoded in the redundancy [138].

(iii) It has been shown that time-domain ptychography can resolve hyperfine temporal structure, easily 10 times finer than the probe pulse duration, with time steps in the order of the probe pulse duration [138].

(iv) Specifically for each measured spectrogram, the spectral amplitude and phase was extracted, i.e. fully characterized the pulse, using the extended ptychographic iterative engine (e-PIE) for the time domain [139,140] where at the cost of a higher redundancy requirement both the SC pulse and the probe can be reconstructed.

Kane et al. recently performed a comparative study between the PCGP algorithm with the PIE and e-PIE for ultrafast laser pulse measurement applications [141]. The operation of the algorithm is described in figure.2.11 with a simple flow chart adapted from [137,141]. To start the algorithm first we need initial guess labeled $X_j(r)$ and $Y_j(r)$, of the object and gate pulses. Using the previous guess the next guess for the signal is formed by multiplying the object $X_j(r)$ by the shifted gate $Y_j(\boldsymbol{r} - Z_{s(j)})$ to from exit-wave function $\psi_j(r)$. The product is Fourier transformed, and the modulus is replaced by $I_j(u)$, which is the measured intensity data. The updated exit-wave $\psi'_j(r)$ is inverse Fourier transformed, and updated object and gate guesses are extracted from the result using two update functions. Object guess is update using the update function 1 and is given by,

$$X_{j+1}(r) = X_j(r) + \alpha \frac{Y_j^*(r-Z_{s(j)})}{|Y_j(r-Z_{s(j)})|^2_{max}} \times (\psi'_j(r) - \psi_j(r)) \quad (2.20)$$

α can be adjusted to alter the step-size of the update, but typically set to one and can be varied to improve convergence.

The update of the gate proceeds similarly, with update function 2 being given by,

$$Y_{j+1}(r) = Y_j(r) + \beta \frac{X_j^*(r-Z_{s(j)})}{|X_j(r-Z_{s(j)})|_{max}^2} \times (\psi'_j(r) - \psi_j(r)) \quad (2.21)$$

β can be adjusted to alter the step-size of the update similarly to an α. The process continues until an iteration is complete once all the data is used to update the object function.

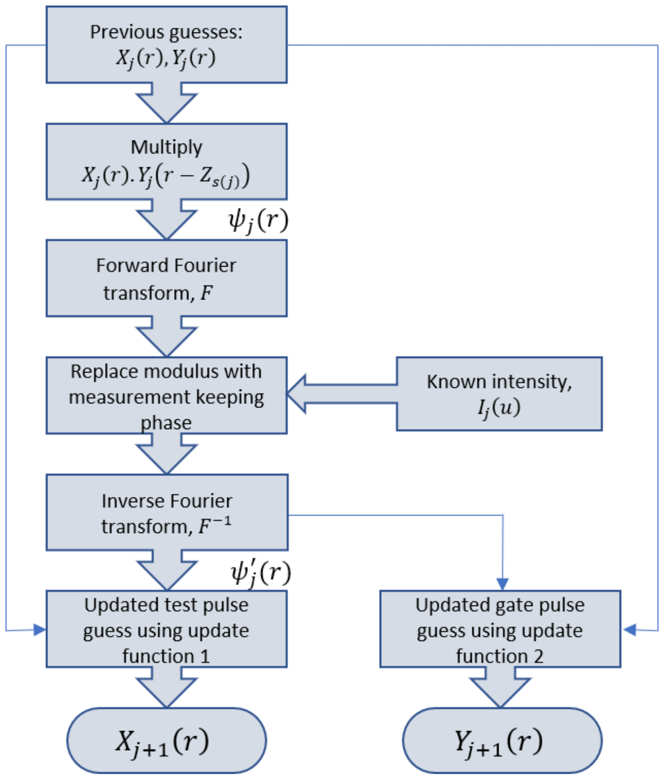

Figure 2.11. The flow chart of the extended ptychographic inversion engine (e-PIE) used for XFROG retrieval.

2.8 Relative intensity noise measurements

The fluctuations in the output power of the laser are defined by relative intensity noise (RIN). This can be thought of as the pulse-to-pulse intensity variation, these intensity variations arise due to several factors including beam pointing, optical stability, and electrical noise. The measurement of RIN serves as a quality indicator of laser and amplifier devices. RIN is a type of inverse carrier-to-noise-ratio measurement and it can be defined as the ratio of the mean-square optical intensity noise to the square of the average optical power in a certain frequency bandwidth.

$$RIN_{lin} = \frac{<\delta P(t)^2>}{P_{ave}^2 \cdot \Delta f}[1/\text{Hz}] \qquad (2.22)$$

where $< \delta P(t)^2 >$is the time-averaged optical intensity fluctuations, P_{ave} is the average optical power, and Δf is the noise bandwidth. For convenience, RIN is always normalized to a 1 Hz bandwidth so that it is easier to compare the intensity fluctuations of different systems. The ratio of the squared optical powers is equivalent to the ratio of the measured electrical powers. Thus, RIN can be expressed in terms of detected electrical powers as

$$RIN = \frac{N_L}{P_{ave(ele)} \cdot \Delta f}[1/\text{Hz}] \qquad (2.23)$$

where N_L is the electrical power noise, coming from optical power fluctuations averaged in time, and $P_{ave(ele)}$ is the average power of the photocurrent power (DC) and Δf is a bandwidth of noise. Noise measured by spectrum analyzer consists of 3 components

$$\Delta P_{ave(ele)} = N_L + N_q + N_{th} \qquad (2.24)$$

N_L is laser noise, N_q is shot (quantum) noise of photocurrent, N_{th} is thermal noise. N_q is provided by the quantum nature of photons arriving at the detector and defined as $N_q = 2qI_{DC}R_L$, where q is the elementary charge, I_{DC} is the DC current, and R_L the load resistance. N_{th} is produced by the detector as well as the accompanying electronics after photodetection and can be measured under a dark condition. N_L is the desired RIN term that refers to the laser under test, which can be obtained by subtracting the shot and thermal noise contributions from the total measured noise.

Chapter 3. Characterization of commercial ultra-high numerical aperture fibers and photonic crystal fibers

The crucial role of GVD in ultrafast optics systems motivated following the design work on ultrafast fiber amplifiers in this dissertation, with the characterization of linear properties of custom or specialty vendor-available optical fibers intended for use in the work. In this chapter firstly, I present and discuss results of broadband GVD measurements of commercially available ultra-high numerical aperture fibers (UHNA) from Coherent-Nufern [142,143]. These fibers are attractive for dispersion management in ultra-fast fiber laser systems in the 2000 nm wavelength range, but experimental dispersion data in the literature is scarce and inconsistent. Secondly, I characterized the polarization-maintaining (PM), highly nonlinear photonic crystal fibers intended for femtosecond pumping at a wavelength of 1560 nm, to validate their applicability in seed sources in the amplifier systems investigated in my dissertation. The dispersion profile is significant during the investigation of supercontinuum (SC) generation in photonic crystal fibers (PCF), as it determines nonlinear interactions during SC formation. After outlining the principles of these measurement techniques and describing the experimental setup, results for various UHNA fiber and PCFs are presented and discussed.

Some of the experimental results contained in this chapter are published in [43] and [70] where I am the co-author.

3.1 Dispersion of commercial UHNA fibers

Devices based on the ultra-fast fiber technology including fiber oscillators operating under various conditions like solitonic [144,145], dissipative solitonic [146], stretched pulse [147–149], self-similar [150,151], all-normal dispersion [152,153], or noise-like regimes [146,154], strongly rely on the accurate balance of dispersion inside the cavity to facilitate high pulse energies, wide bandwidths, or both. Here, I discuss coherently seeded erbium and thulium amplifiers based on the fiber chirped-pulse amplifier (FCPA) scheme [14]. An important factor is to manage the chirp in the setup. A series of commercially available UHNA fibers developed by Coherent-Nufern [142,143], has found application in intracavity dispersion control tool, especially in ultra-fast oscillators working at wavelengths near 2000 nm [149]. These fibers have normal GVD in the above mentioned spectral range, i.e., they can be used to compensate for the anomalous GVD of standard active and passive fibers. UHNAs were originally designed for increasing the coupling efficiency to waveguides by splicing short sections (ie. “bridge fibers”), and for dispersion compensation.

In addition to their numerical aperture matching and chirp management functionalities, small mode areas of UHNA fibers support nonlinear optics applications like SC generation, which has been demonstrated in some of these fibers [40,155–157]. For example, an all-normal dispersion profile facilitates the formation of SC with a high degree of pulse-to-pulse coherence, compressible to short pulse widths using standard ultra-fast techniques [158]. Despite these emerging applications, experimental dispersion data on UHNAs is usually not freely accessible from the manufacturer and the values found in the literature are available for a single wavelength only, and on top of that, this data is often inconsistent.

In scope of my work, I performed measurements of chromatic dispersion using the spectral interferometry technique covering the typically used erbium, thulium, and holmium emission bands. Results were obtained for UHNA1, UHNA3, UHNA4, UHNA7, and PM2000D fibers from the company Coherent-Nufern. These results are used in the design of ultra-fast fiber amplifiers that will be presented and discussed in the following chapters.

3.1.1 Principles of the technique

For short fiber samples, direct chromatic dispersion measurement methods like the phase shift technique [159] are not viable. Spectral interferometry is widely used which is based on the Mach-Zehnder interferometer, with the fiber under test placed in one arm and the other arm serving as the reference, as shown in figure 3.1. The measurement reveals the spectral phase difference between the two interferometer arms, which in an ideal scenario comes only from the fiber under test. Chromatic dispersion can then be obtained indirectly by subsequent differentiation.

In my work I employed a spectral interferometric method based on Hlubina et al. [160], with modifications to calculate the dispersion of commercial fibers. Optical path length in the reference arm and the fiber arm was adjusted to obtain the high visibility of the fringes and equalization wavelengths at which the group delay observed in both arms was equal.

This method is suitable when I have high visibility fringes as shown in figure 3.1. Here it depends on assigning the order of the spectral interference fringe versus its wavelength position. A bright fringe on a spectral interferogram satisfies the following formula

$$L - l - n(\lambda)z = m\lambda \,, \qquad (3.1)$$

where L is the length of the (empty) reference arm of the interferometer, l is the length in the air of the test arm in which the fiber to be measured is placed, $n(\lambda)$ is the refractive index of the fiber (wavelength-dependent) and z is the fiber sample length, m is the order of interference of the fringes. Counting i bright fringes in the direction of blue-shifted wavelengths yields

$$[L - l - n(\lambda)\mathrm{z}] / \lambda = m + i \qquad (3.2)$$

By assigning the interference order i to the positions of peaks and valleys on an interferogram as shown in figure 3.1, one can retrieve the spectral phase shape unambiguously under the following conditions. Firstly, the interference orders shall be numbered in such a way that they go through extrema at equalization wavelengths to reflect the vanishing of group delay differences. Secondly, it should be known whether a given equalization wavelength fringe is in the normal or anomalous dispersion region. This information was easily accessed by observing the direction of spectral shift of the equalization point upon the change of optical path difference between the interferometer arms, determines whether a given extremum in the fringe order function should be a minimum or a maximum. If these conditions are met the constructed interference order function i(λ) will satisfy equation. (3.2) and reflect the shape of the spectral phase. For example, if the shortest equalization wavelength is in the normal dispersion region, then going towards longer wavelengths the fringe order should increase up to the first equalization wavelength, decrease until the second equalization wavelength, then increase once again in the direction of longer wavelengths and so on, depending on the number of equalization points visible in the interferogram.

Subsequent operations enable us to retrieve the dispersion parameter D either by direct numerical differentiation [161] or by approximating the refractive index with polynomials. Hlubina et al. [160] used a modified Cauchy dispersion formula in the form of below mentioned equation

$$n(\lambda) = A_1\lambda^{-4} + A_2\lambda^{-2} + A_3 + A_4\lambda^2 + A_5\lambda^4 \qquad (3.3)$$

Inserting (3.3) into (3.2) yields a function which is found to fit the interference order function satisfactorily even for relatively complicated phase profiles,

$$i = a_1\lambda^{-5} + a_2\lambda^{-3} + a_3\lambda^{-1} + a_4\lambda + a_5\lambda^3 - m, \qquad (3.4)$$

where $a_1=-A_1/z$, $a_2=-A_2/z$, $a_3=L-l-A_3/z$, $a_4=-A_4/z$, $a_5=-A_5/z$, and m are the fitting parameters. Dispersion D can then be calculated as

$$D(\lambda) = \frac{1}{c}\frac{\mathrm{d}N(\lambda)}{\mathrm{d}\lambda} = \frac{1}{c}(-20A_1\lambda^{-5} - 6A_2\lambda^{-3} - 2A_4\lambda - 12A_5\lambda^3), \qquad (3.5)$$

where c is the velocity of light in vacuum, N(λ) is the group index, given by

$$N(\lambda) = n(\lambda) - \lambda\frac{\mathrm{d}n(\lambda)}{\mathrm{d}\lambda} \qquad (3.6)$$

The method is convenient for two ZDWs provided that there is a sufficient number of spectral fringes present in the measured spectral range.

3.1.2 Experimental setup for dispersion measurement

To measure the dispersion of fiber, I use an unbalanced Mach-Zehnder interferometer setup as shown in figure 3.1. Collimated SC having broad bandwidth (450 - 2400 nm) is used as a light source, which has high brightness and spatial coherence. Beam splitter with 1 - 6 µm anti-reflection coating (BS_1) divides the light into the two arms of an interferometer. Neatly cleaved test fiber is placed in the test arm. An aspheric lens (L_1) couples the SC into the test fiber and another aspheric lens (L_2) at the output end collimates the light. Coupling of light into fiber was monitored by imaging the output end of the fiber on to an infrared camera which also confirmed excitation of the fundamental mode in the investigated fiber in all measurements. The gradient filter (G) in the reference arm allows us to maintain equal intensity in both arms. The two mirrors (M_3 and M_4) on the linear stage in the reference arm helps to compensate for the optical path of the measurement arm. In the case of PM fibers, a broadband linear polarizer was placed before and after the fiber as shown in figure.3.1. The polarizer and analyzer are rotated to excite either the fast or slow axis, at a time. The geometry of the setup and range of linear stage allowed for the fiber of length 10 to 20 cm with a typical length of about 15 cm.

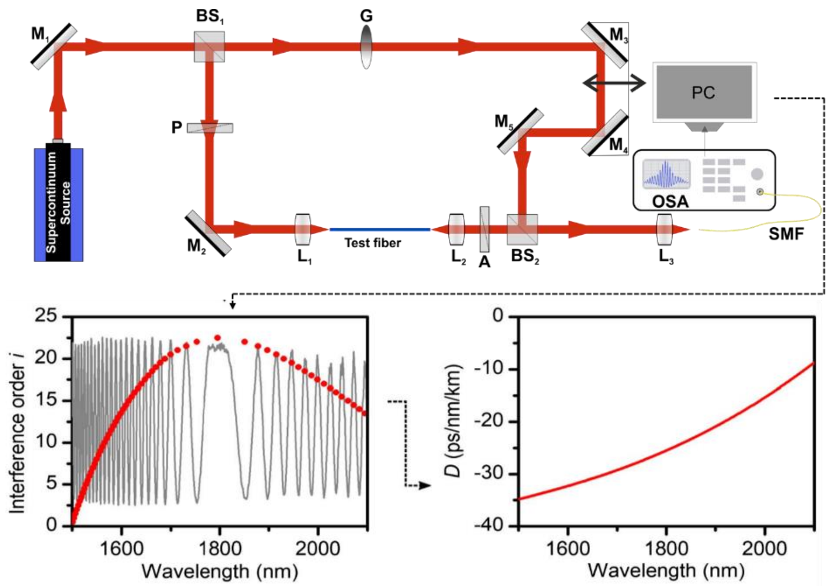

Figure 3.1. Mach-Zehnder interferometer experimental setup and workflow for obtaining dispersion by assigning the interference order i to the positions of peaks and valleys of the spectral interferogram. M - silver mirrors, P - polarizer, BS - beam-splitter, G - gradient neutral-density filter, L – aspheric lenses, A - polarization analyzer, SMF - single-mode fiber OSA - optical spectrum analyzer, PC - personal computer.

Light from both arms was combined in a beam splitter (BS_2) and collimated. A lens (L_3) is used to couple the light from the interferometer output into single-mode fiber patch cord (SMF) to an optical spectrum analyzer (OSA) (Yokogawa AQ6375) capable of recording spectra spanning wavelength range from 1200 nm to 2400 nm. It was ensured that the width of the finest fringe on each recorded interferogram was much greater than the spectral resolution of OSA set at 0.5 nm. Integration time of 3 ms was allowed for multiple SC pulses to be combined to form the signal at each measurement point. The length of the reference arms is adjusted to find the optical path difference between the test and reference arm. The parasitic dispersion of two thin aspheric lenses used for coupling and collimating the light in the test arm was partially compensated by the neutral-density gradient filter placed in the reference arm for equalization of the intensities of the interfering fields. Nevertheless, the effective dispersion of those elements was determined from the Sellmeier coefficients and subtracted from the experimental results.

3.1.3 Results and discussion

In this section, the five Coherent-Nufern's UHNA fibers including UHNA1, UHNA3, UHNA4, UHNA7, and PM2000D are discussed. The PM2000D fiber is specially designed for the ~2000 nm region. Dispersion spectra of the fibers are plotted and presented in terms of dispersion parameter *D* expressed in ps/nm/km, as widely used in the fiber community, GVD β_2 is expressed in ps^2/m, common in the ultrafast science, and TOD β_3 is expressed in ps^3/m. The β_2 is especially useful in judging the amount of higher orders of the spectral phase by observing the slope of the dispersion curve. The exact wavelength range for which the dispersions were obtained for different fibers depended on the visibility of the fringes. However, the typical erbium, thulium, and holmium emission bands were covered in each case.

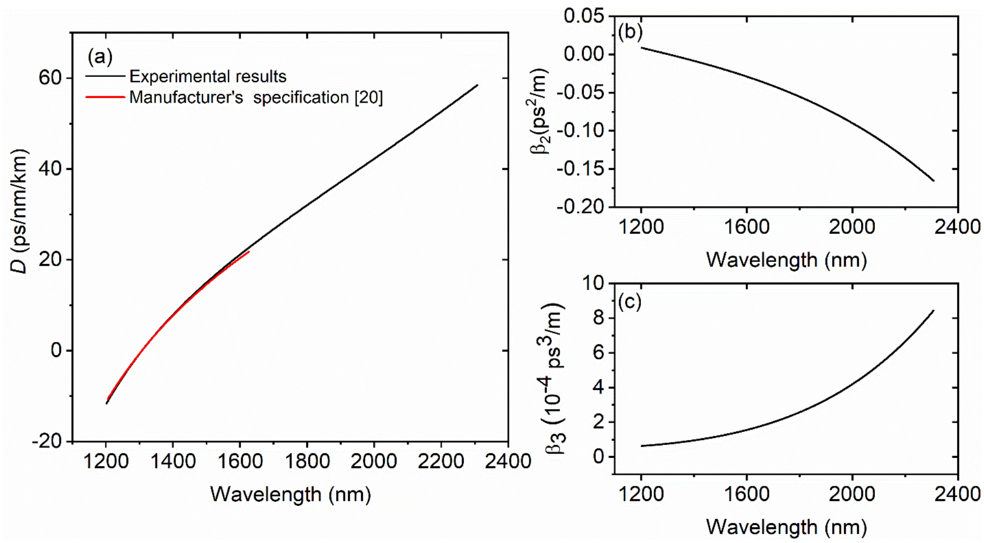

Figure 3.2. (a) Measured dispersion D of a standard single-mode fiber SMF-28 ultra compared with the manufacturer's specification available in the 1200–1625 nm region [80]. (b) group velocity dispersion β_2 and (c) third-order dispersion β_3.

The overall performance of the setup and method was verified by measuring the spectrum of the dispersion parameter *D* of a standard single-mode fiber SMF-28 ultra fiber. The results in figure 3.2(a) show good agreement with the manufacturer's specification [80] in the region of 1200–1625 nm. The zero dispersion is located at 1308 nm, with *D* varying between (15) – (42) ps/nm/km in the range 1500–2000 nm. Figure 3.2 (b) and (c) represents the GVD varying from -0.017 ps^2/m

to -0.089 ps^2/m, and TOD varying from 1.2×10^{-4} ps^3/m to 4.1×10^{-4} ps^3/m in the range of 1500–2000 nm respectively. Most of the commercial component's fiber pigtail has SMF 28 fiber in non-PM version and PM1500 fiber in PM version. So, it is very crucial to have known the dispersion in a broad wavelength range and higher order dispersion for dispersion compensation in ultrafast fiber systems.

Table 3.1. Geometrical and Optical specification of ultra high numerical aperture fibers provided by manufacturer* Coherent Nufern along with SMF28 Ultra.

Fiber	Core diameter (µm)	Numerical aperture	Operating wavelength (Catalogue)
SMF 28 Ultra	8.2	0.14	1200–1625 nm
UHNA 1	2.5	0.28	1100 – 1600 nm
UHNA 3	1.8	0.35	960 – 1600 nm
UHNA 4	2.2	0.35	1100 – 1600 nm
UHNA 7	2.4	0.41	1500 – 2000 nm
PM2000D	2.1	0.37	1500 – 2100 nm

* Data obtained from manufacturer catalogue [80,142,143]

In single mode UHNA fibers, I measured high visibility fringes in the range of 1200 to 2400 nm range, which helped to obtain dispersion in full spectral range. In Ciąćka et al. [70] only the results of dispersion in the range which verified with the results from direct numerical differentiation of the spectral phase [161] are presented with standard deviation for each fiber. Here, I present and discuss the results in full spectral range solely based on dispersion measurements.

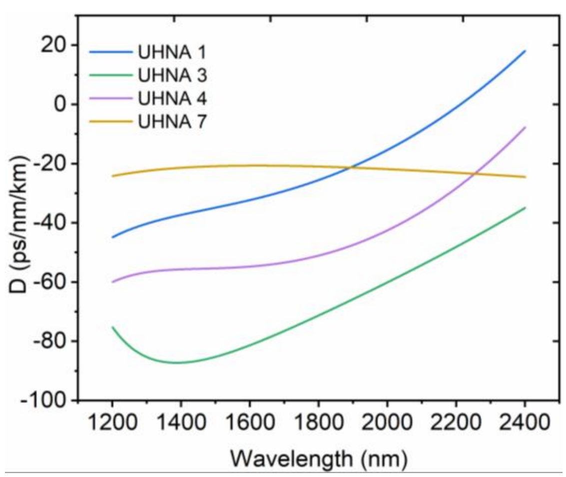

Figure 3.3. Dispersion of all single mode UHNA (1,3,4,7) fibers are presented in terms of the dispersion parameter D.

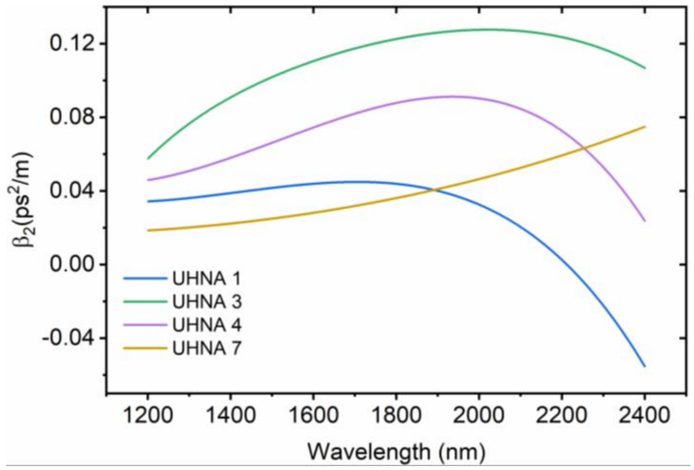

Figure 3.4. Group velocity dispersion β_2 of all single mode UHNA (1,3,4,7) fibers.

UHNA1 is one of the first fibers measured in these series displaying a ZDW around 2210 nm within the measured spectral range as shown in figure 3.3. UHNA1 has 2.5 μm fiber core and is designed to operate in the range of 1100 - 1600 nm from table 3.1 obtained from Coherent Nufern catalogue. The dispersion is generally low and flat, with D varying only between (−44) - (−32) ps/nm/km in the range 1200 - 1600 nm and -15 ps/nm/km at 2000 nm. The group velocity dispersion β_2 is plotted in figure 3.4. This fiber has been used in soliton laser operating at 2000 nm in Kadel et al. [149]. They used UHNA1, UHNA4, and UHNA7 to study the compression in the negatively chirped output of a soliton laser operating at 2000 nm by observing the autocorrelation traces. No significant compression was observed using UHNA1. Certainly, from figure 3.3 I can observe UHNA1 fiber exhibiting the lowest normal dispersion value at 2000 nm. Kadel et al. also calculated β_2 value theoretically by using the formula for step-index fibers and the core diameter and numerical aperture values were used as provided by the manufacturer. The calculated GVD at 2000 nm was -0.081 ps^2/m [149], which is more than two times bigger than the one measured here -0.033 ps^2/m (figure 3.4). Also calculated GVD values provided by Kadel et al. for UHNA1, UHNA4, and UHNA7 seems regularly overestimated. A normal dispersion fiber matching the specification of UHNA1 was also employed in the design and development of a Thulium fiber laser operating around 1930 nm [153]. The total cavity dispersion was measured before and after inserting a 6.6 m length of UHNA1, and from the difference, the fiber GVD was estimated to $\beta_2 = 0.036$ ps^2/m, very close to our measured value $\beta_2 = 0.038$ ps^2/m at 1930 nm (figure 3.4). Wienke et al. [148] also estimated the dispersion of the same fiber as 0.0474 ps^2/m at 1900 nm is in good agreement with results presented in this chapter of 0.041ps^2/m.

UHNA3 displays a much larger normal dispersion than UHNA1 and shows a steeper dispersion slope between 1600 - 2400 nm as shown in figure 3.3. UHNA3 has 1.8 µm core diameter, which is the smallest core in this UHNA series and is designed for typical operation in the range of 960 - 1600 nm. The dispersion parameter D = (−75) - (−81) ps/nm/km varying with only 6 ps/nm/km between 1200 - 1600 nm with a dispersion minimum of -87 ps/nm/km at 1388 nm. The GVD flattens around 2000 nm, with maximum of 0.12 ps^2/m at 2024 nm and has zero third-order dispersion (TOD) near 2020 nm. With the existing literature on dispersion values, there are only two values, both of which refer to ~1000 nm wavelength [40,157] not accessible with our setup.

The core diameter of UHNA4 was 2.2 µm with operating range of 1100 - 1600 nm as shown in table 3.1. The UHNA4 dispersion slope has the similar trend compared to UHNA1 and lies between UHNA1 and UHNA3 in the measured spectral range as shown in figure 3.3. The dispersion of UHNA4 has been reported by several groups around 2000 nm. Wang et al. [146] obtained β_2 = 0.09323 ps^2/m at 1900 nm from spectral interferometry measurements, which is close to the GVD value of 0.090 ps^2/m at 1900 nm as shown in figure 3.4. Subsequently, Kadel et a [149]. presented three values of dispersion at 2000 nm, the calculated value was 0.17 ps^2/m, estimated from autocorrelation pulse width measurements was ~0.09 ps^2/m, and from the influence of cavity, GVD resulted in ~0.12 ps^2/m in Thulium oscillator. Similar to earlier observations, the calculated dispersion values for UHNA fibers yield an overestimation, but the autocorrelation-based measurements showed excellent agreement. Wang et al. [146] also reported the value of third-order dispersion $\beta_3 = 1.536\cdot10^{-4}$ ps^3/m, which differs from our result of about $-2\cdot10^{-5}$ ps^3/m. At 2000 nm, the fiber exhibits a dispersion parameter of D = −42 ps/nm/km, which almost exactly cancels the dispersion of SMF-28 while not adding a significant amount of TOD.

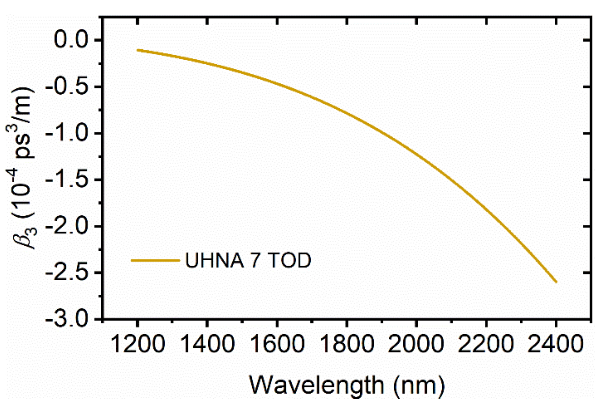

Figure 3.5. Third order dispersion β_3 of all single mode UHNA 7 fiber.

UHNA7 with 2.4 μm core diameter and 0.41 numerical aperture was typically designed for operation in 1500 – 2000 nm range. UHNA7 exhibits a low and flat normal dispersion with only 5 ps/nm/km variation over the entire measured spectral range compared to other UHNA's as shown in figure 3.3. I also present the TOD for this fiber which displays a significant negative TOD near 2000 nm as shown in figure 3.5. Hence the detailed dispersion measurement for UHNA7 fiber is provided in the broad spectral range in this chapter. As described in figure 3.4, GVD measurement result yields β_2 = 0.0464 ps^2/m and figure 3.5 shows the TOD $\beta_3 = -1.22\cdot10^{-4}$ ps^3/m at 2000 nm. It is also interesting to note that both its 2nd and 3rd dispersion orders are opposite in sign to those of SMF-28 fiber. This is a useful property for compensating higher-order dispersion in an ultrafast laser cavity or amplifier system. Hence, this fiber is used in an amplifier system for stretching the SC pulses to amplify the 2000 nm region in the thulium/holmium-doped fiber amplifier [63,162].

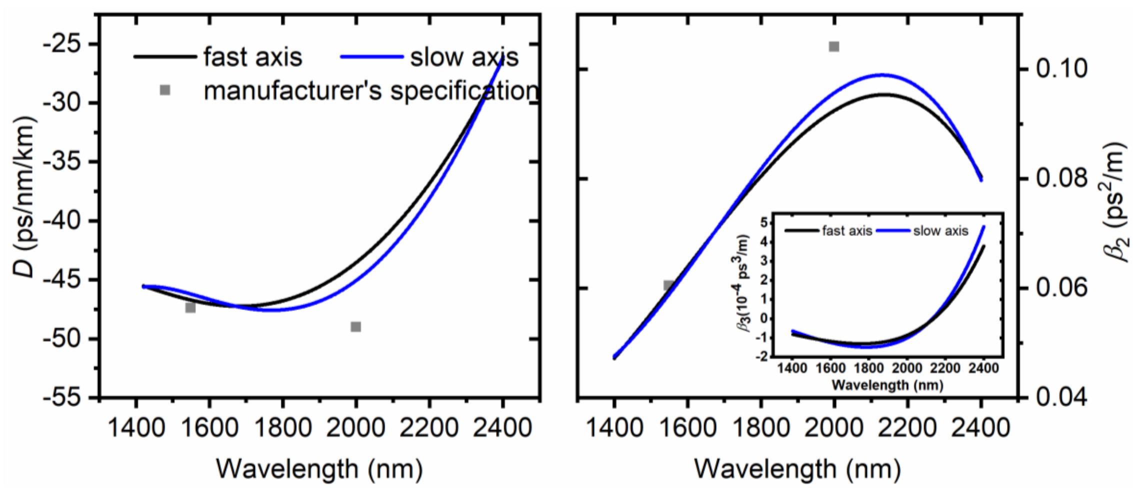

Figure 3.6. Dispersion of PM2000D fiber (black line - fast axis, blue line - slow axis) given as the dispersion parameter D (left), group velocity dispersion β_2 (right), and third order dispersion β_3 (left inset) and squares designate the manufacturer specified values.

Coherent-Nufern's has recently added a panda-type PM fiber with a tailored dispersion specifically designed for the 2000 nm wavelength region. PM2000D fiber has 2.1 μm core diameter and 0.37 numerical aperture and operating wavelength range in 1500 - 2100 nm. Figure 3.6 presents the measured dispersion characteristics of the PM2000D fiber. To date, this is the only commercially available PM, normal dispersion fiber in this wavelength range. Dispersion is measured in both the polarization axes. Figure 3.6 displays the dispersion curves for both polarization axes in terms of D, β_2, and β_3. The manufacturer specifies the dispersion as -47.4 ps/nm/km at 1550 nm and −49 ps/nm/km at 2000 nm as displayed in figure 3.6. These values compare well with our measurements. We also included the manufacturer's general specification on dispersion in figure 3.6. According to Coherent-Nufern, the fiber is designed to exhibit a very low slope of the dispersion parameter D in the 2000 nm region, a feature that is well backed by our measurements. *D* varies only by ~10 ps/nm/km in the range of 1420 - 2100 nm around a central value of −45 ps/nm/km. TOD is flat to slightly negative, the measured zero TOD wavelength is located near 2130 nm as shown in the inset of figure 3.6. Therefore, the fiber seems indeed well suited for dispersion control in ultrafast fiber laser systems in both 1550 nm and 2000 nm wavelength region. This fiber was used in building all PM thulium and erbium fiber amplifiers [163], which will be discussed in chapter 5 and chapter 6.

Table 3.2 shows the fitting coefficients A_1–A_5 used to generate the plots of the dispersion parameter *D* shown in figure 3.3 and specifies the wavelength range of applicability of the results. Depending on the application and requirements, dispersion data can be directly reproduced using the coefficients.

Table 3.2. Fitting parameters for reproducing the measured dispersion parameter D using Eq. (3.5)[a]

Fiber	A_1	A_2	A_4	A_5	Applicability range
UHNA1	1.132·10−6	−2.059·10−6	6.734·10−6	−2.239·10−7	1200–2400 nm
UHNA3	−5.855·10−6	17.273·10−6	5.029·10−6	−1.186·10−7	1200–2400 nm
UHNA4	1.982·10−6	−5.01·10−6	10.433·10−6	−2.798·10−7	1200–2400 nm
UHNA7	1.161·10−9	1.093·10−6	1.443·10−6	−3.453·10−10	1200–2400 nm
PM2000D (slow axis)	3.766·10−6	−9.296·10−6	9.677·10−6	−2.143·10−7	1420–2400 nm
PM2000D (fast axis)	1.102·10−6	−3.015·10−6	7.752·10−6	−1.706·10−7	1400–2400 nm

[a]To obtain D in ps/nm/km, express the speed of light c in km/ps, and the wavelength λ in μm.

3.2 Dispersion of soft glass PCF

As shown in chapter 2, PMI is one of the limiting factors for generating coherent SC. PMI leads to significant pulse-to-pulse fluctuations and coherence degradation of SC pulses, particularly in weakly birefringent fibers. However, PMI can be efficiently suppressed in highly birefringent ANDi PCF, which eliminates the last remaining noise amplification process in femtosecond pumped ANDi SC generation.

Dispersion of a PCF plays a central role in determining pulse propagation dynamics and SC spectral formation. For this reason, accurate characterization of PCF is of utmost importance. Numerical calculation of PCF dispersion based on geometrical analysis of SEM cross-section of the PCF provides reasonable approximation of the physical chromatic dispersion profile. However, in a real PCF, the diameter of microstructures and pitch of the photonic lattice may vary across the microstructure, as well as along the PCF. Therefore, the actual experimental results are very important from the amplifier system design point of view.

In the following section, I discuss the results of chromatic dispersion measurements in one non-PM ANDi PCF and two PM ANDi PCF designs, which later found application in the amplifier setups in my work.

3.2.1 Principles of the technique

In the previous section, Mach-Zehnder interferometer set-up was used to measure the dispersion. The dispersion is retrieved by direct cosine fitting of the interferogram to obtain spectral phase. The drawback of this method is that it requires high-quality (high contrast) interference fringes. In the case of the silicate glass ANDi PCFs, I observed attenuation at levels exceeding the commercial UHNA fibers. Due to this fact, I did not observe high contrast, clear interferogram fringes in full measurement bandwidth (i.e. in the sensitivity range of the OSA). Therefore, the characteristic wide interference fringes over a wide spectral range are recorded step by step. Firstly, the position of the equalization wavelength is set to one of the extreme edges of the OSA sensitivity wavelength range. Then position of this equalization wavelength is then recorded for every small step $\Delta x(\lambda)$ of the translation stage movement in the reference arm for entire measurement bandwidth.

This data was used to obtain the relative group index $N_{rel}(\lambda)$ using the below mentioned equation (3.7)

$$N_{rel}(\lambda) = \frac{2\cdot\Delta x(\lambda)}{L} + 1 \qquad (3.7)$$

where L is the length of the fiber.

Measured $N_{rel}(\lambda)$ was fitted with a 5th order polynomial, that is Cauchy dispersion equation, as follows:

$$N_{rel}(\lambda) = A_1\lambda^{-4} + A_2\lambda^{-2} + A_3 + A_4\lambda^2 + A_5\lambda^4 \qquad (3.8)$$

From this, I can obtain A_1-A_5 parameters to further calculate the chromatic dispersion as:

$$D(\lambda) = \frac{1}{c}\frac{\mathrm{d}N_{rel}(\lambda)}{\mathrm{d}\lambda} = \frac{1}{c}(-4A_1\lambda^{-4} - 2A_2\lambda^{-2} + 2A_4\lambda^2 + 4A_5\lambda^4) \quad (3.9)$$

The data obtained during measurements are fitted with equation $N_{rel}(\lambda)$ as mentioned in equation (3.8). In the case of PM fiber, N_X and N_y represented the relative group index for X and Y polarizations respectively. The fitting parameters of $N_{rel}(\lambda)$ are used to calculate the chromatic dispersion (D) from equation (3.9).

3.2.2 Results and discussion

In this section, I describe the PM PCF structure used for coherent, polarized seed SC signal generation and the results of measurement of chromatic dispersion of one non-PM ANDi PCF and two PM ANDi PCF designs. The PM ANDi PCFs were specially designed fiber for pumping with 1560 nm (center wavelength) femtosecond lasers. The dispersion characteristics of the fibers presented in terms of dispersion parameter D are expressed in ps/nm/km. The fitting coefficients A_1–A_5 are provided, to reproduce the dispersion. In the following presentation, investigated fibers are labelled accordingly to their original labels used in respective literature.

3.2.2.1 NL38 fiber

NL38 is an all-normal dispersion fiber, which has already been demonstrated in coherent SC generation experiments [51,52] and more recently in the coherent seeding of ultrafast, Tm-Ho fiber amplifier seeding. The fiber structure as shown in the scanning electron microscope (SEM) (figure 3.7), referred to as the ‘base structure’. It has a hexagonal lattice, in which the air-holes are filled with a different type of glass rods at the preform assembly stage, to form glass inclusions in the final fibers. This design was realized in an all-solid configuration using two thermally compatible silicate glasses. Schott SF6 is used as core and lattice glass, Schott F2 for lattice inclusions, and tube glass.

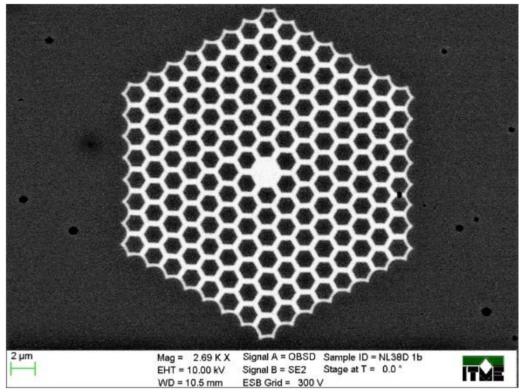

Figure 3.7. SEM image of the NL38 fiber structure here referred to as the 'base structure'.

The refractive index of the core is higher than that of the surrounding lattice. Therefore, the structure supports index-guided propagation. This all-solid glass photonic crystal fiber approach enables engineering of flattened normal chromatic dispersion profiles. Chromatic dispersion of the fiber is influenced by the contributions of both the waveguide (lattice topology) and the two glass types (material dispersion contribution).

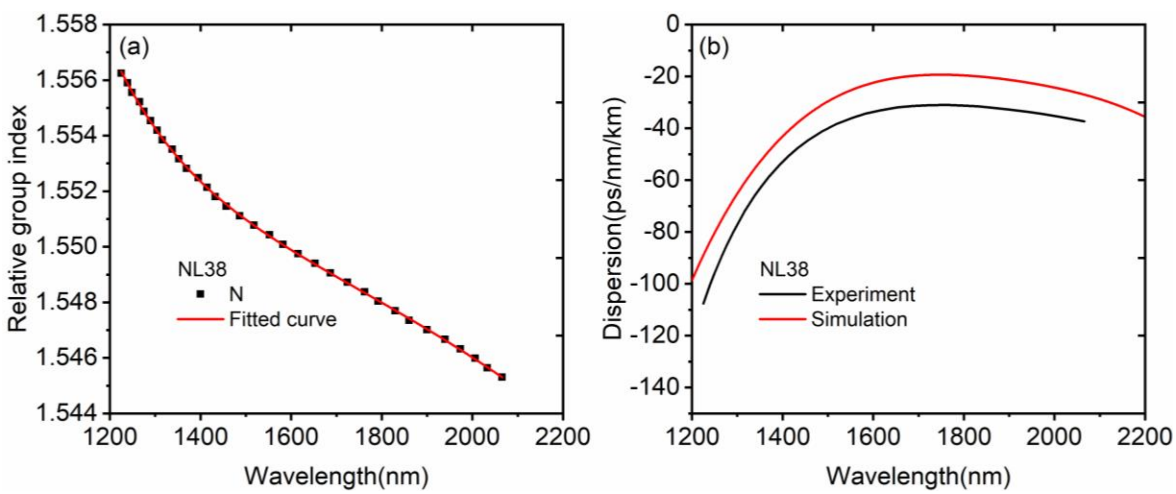

Figure 3.8. (a) Relative group index obtained from measurements for NL38 fiber. Solid dots are measured points and the line obtained by fitting (b) Dispersion comparison between the calculated (Black curve) and simulation (red curve).

The relative group index of the NL38 fiber obtained from measurements is shown in figure 3.8 (a). By fitting the $N_{rel}(\lambda)$ data with the 5th order polynomial, the chromatic dispersion (D) is obtained from equation (3.8) as shown in figure 3.8 (b) (Black curve). The NL38 has flat dispersion in the range of 1500 nm and 2000 nm within ±5 ps/nm/km around -20 ps/nm/km at the intended pump wavelength of 1560 nm obtained from numerical results. From the experiment, I obtain local maximum dispersion of -31 ps/nm/km at a wavelength of 1724 nm. Dispersion remains at normal values for the whole considered wavelength range. Hence, the comparison with results of numerical simulations reported by Dobrakowski et al. [43] revealed very good agreement between theoretical and experimentally obtained dispersion profiles, thus supporting the accuracy of measurement. A 10 ps/nm/km small difference between the numerical simulation and the measurement is related to diffusion during drawing not being considered in the simulations.

Numerical simulations were performed using the finite element method, operationalized in COMSOL Multiphysics software. I am not discussing the designing of PCF and its numerical results since it is out of the scope of thesis. Details on the design, numerical simulations, material properties, and fabrication technology are discussed by Dobrakowski et al. [43] in. Here I mainly discuss the experimental results which are crucial in understanding SC generation and building of the amplifier systems investigated in this work.

3.2.2.2 NL48 fiber

The NL38 fiber structure was the starting point in the design and fabrication of a polarization-maintaining variant. The fiber was developed by D. Dobrakowski, in collaboration with author of this dissertation [43]. The design with bow-tie modification of the original base structure is shown in figure 3.9 labelled NL48. Compared to the base structure, this design has one less outer honey-comb ring in the photonic lattice. The lattice constant is $\Lambda = 1.73$ µm, the width of the hexagonal inclusion is $d = 1.35$ µm, and $d/\Lambda = 0.77$. The outer diameter of the whole designed structure was 125 µm. The structure consists of three glasses with different refractive indices. Two of them are again Schott SF6 and F2 glasses with similar mechanical properties (identical set as in the NL38 fiber) while the third is a modified F2 glass, with increased thermal expansion coefficient for introducing of stress into the lattice.

The geometrical parameters of ”bow-tie” fiber from the real structure as shown in figure 3.9: the core size was equal to 2.5 x 2 µm, lattice widths were of $d = 24.5/18.7$ µm, average lattice constant of $\Lambda = 1.68$ µm and stress applying zones of the size of 38.6 x 21.5 µm.

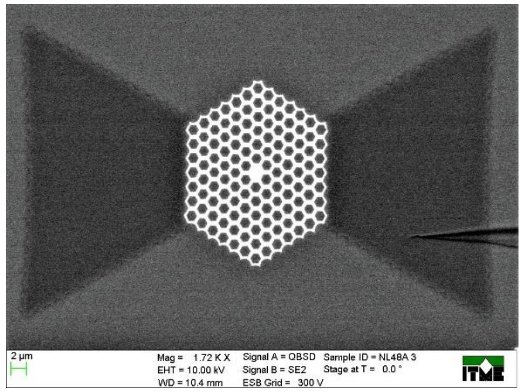

Figure 3.9. SEM image of NL48 fabricated fiber structure with stress-inducing components ('bow-tie' structure) [43].

The fiber has slightly elliptical microstructure, as shown in the SEM image in figure 3.9. Dobrakowski et al [43]. have revealed with numerical simulations and experimental data, that this ellipticity introduced larger birefringence than the stress bow-tie structure, which motivated the final fiber structure discussed in the following section, which had simply a squeezed lattice.

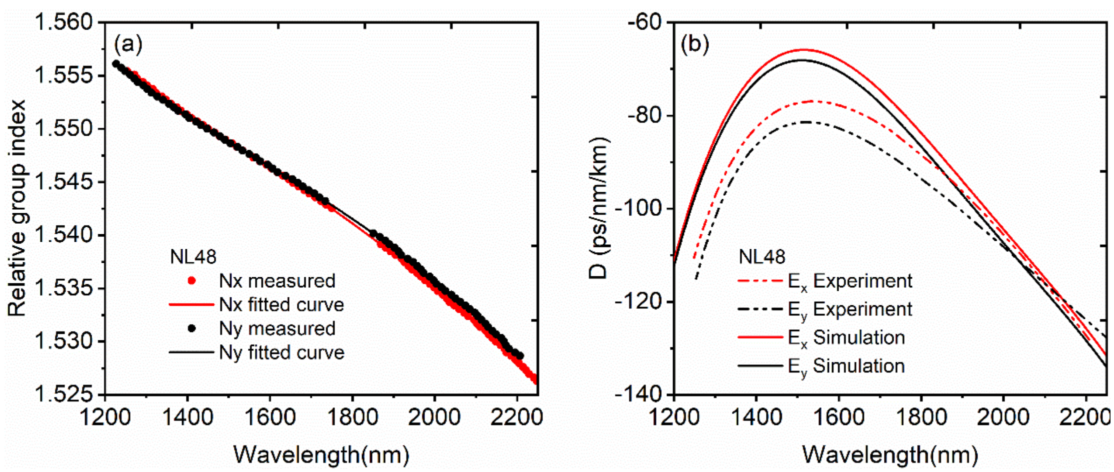

Figure 3.10. (a)Relative group index obtained from measurements for NL48 fiber X polarization (Red) and Y polarization (black). Solid dots are measured points and the lines are curve obtained by fitting (b) Comparison between the calculated [43] (solid line) and measured (dot-dashed line) dispersion of both polarization modes.

From figure 3.10 (a), N_X and N_y represent the relative group index for X and Y polarizations respectively obtained from the measurement. The bow-tie infused fiber structure NL48 has dispersion profile as shown in figure 3.10 (b). The dispersion obtained by simulation results in [43] as D = (−70) – (−128) ps/nm/km in the X-axis and D = (−72) – (−125) ps/nm/km in the Y-axis between 1400–2200 nm. The dispersion obtained from measurement shows a similar trend to calculated results with X-axis dispersion D = (−82) – (−128) ps/nm/km with local maximum of -51.7 ps/nm/km at 1645 nm and Y-axis D = (−86) – (−124) ps/nm/km with local maximum of -56.3 ps/nm/km at 1653 nm between 1400 - 2200 nm. The gap between the measurements in figure 3.10 (a) is due to water absorption and noise structure made it difficult to measure the equalization wavelength precisely in the interferometer setup during the dispersion measurement.

3.2.2.3 NL46 fiber

A different method of introducing birefringence to the hexagonal photonic crystal fiber structure is to make the lattice elliptical, which introduces birefringence. The base structure NL38 can be modified to accomplish this be transverse squeeze of the honeycomb lattice, e.g. by collapsing of two laterally placed air holes during fiber drawing [43]. The fabricated elliptically deformed fiber used in my research is shown in figure 3.11.

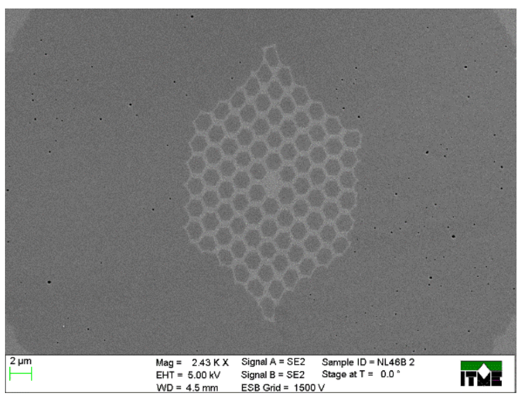

Figure 3.11. SEM image of NL46 fabricated fiber structure with elliptical deformation [43].

The dimensions of the structure's core were equal to 2.7 × 1.9 µm, which means that the structure was more squeezed than the discussed 'bow-tie' fiber. The lattice widths at the diagonals were d = 25.8/16.3 µm and the lattice constant was Λ = 2 µm.

From figure 3.12 (a), N_X and N_y represent the relative group index for X and Y polarizations respectively obtained from the measurement. The elliptical deformed fiber structure NL46 has a dispersion profile as shown in figure 3.12 (b). The dispersion obtained by simulation [43] results in D = (−50) – (−51) ps/nm/km in the X-axis and D = (−52) – (−55) ps/nm/km in the Y-axis between 1400 - 2000 nm. Similarly, dispersion obtained from the experiments shows a similar trend to calculated results with X-axis dispersion D = (−66) – (−73) ps/nm/km with local maximum of -76.9 ps/nm/km at 1533 nm and Y-axis D = (−68) – (−75) ps/nm/km with local maximum of -

81.3 ps/nm/km at 1520 nm between 1400 - 2000 nm. The difference of chromatic dispersion between the X and Y axis is around 3 to 5 ps/nm/km in the range between 1500 nm and 2000 nm. Due to the decrease of lattice rings and elliptical deformation, the core dimensions were 2.7 x 1.9 µm and can observe the slight stepping of dispersion compared to non-PM design. The experiments allowed us to confirm, that the dispersion remains normal in the whole considered spectral range even after the modification to the base fiber design.

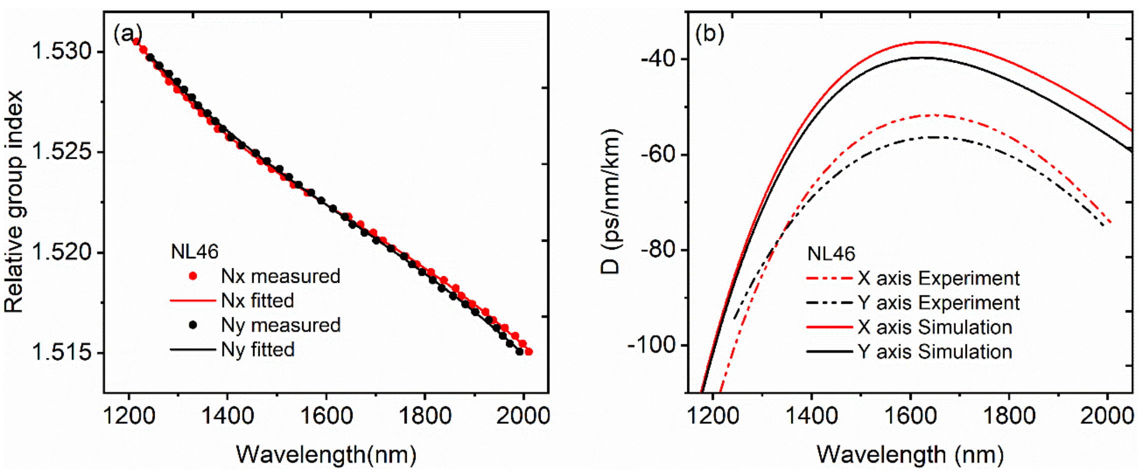

Figure 3.12. (a)Relative group index obtained from measurements for NL46 fiber X polarization and Y polarization. Solid dots are measured points and the lines are curve obtained by fitting (b) Comparison between the calculated [43] (solid line) and measured (dot-dashed line) dispersion of both polarization modes of NL46 fiber

Fitting parameters of $N_{rel}(\lambda)$ obtained for both polarization modes in the elliptical and "bow-tie" fibers are presented in Table 3.3. From these parameters, chromatic dispersion (D) was calculated from equation (3.9).

Table 3.3. Fitting parameters for reproducing the measured dispersion parameter D

Fiber	A1	A2	A3	A4	A5
Bow-tie (E_x pol)	4.83E-02	-5.21E-02	1.58E+00	-0.01009	2.81E-05
Bow-tie (E_y pol)	3.39E-02	-2.71E-02	1.57E+00	-0.0053	-4.07E-04
Elliptical (E_x pol)	8.19E-03	2.34E-02	1.51E+00	0.0058	-1.20E-03
Elliptical (E_y pol)	-2.36E-03	3.54E-02	1.50E+00	0.00574	-1.16E-03

To obtain *D* in ps/nm/km, express the speed of light *c* in km/ps and the wavelength λ in µm.

The values of estimated nonlinear coefficient are provided in table 3.4, calculated using the formula (3.14):

$$\gamma = \frac{2\pi n_2}{\lambda A_{eff}} \qquad (3.14)$$

and the parameters were taken from sources referred in table 3.4.

With the effective mode area at the level of 3.7 μm^2 corresponding to nonlinear refractive index (n_2) of 21×10^{-20} m^2/W (at wavelength of 1500 nm) [52], the soft glass fibers reported here constitute an alternative to silica-based fibers, because of the potential to decrease requirements on the peak pump power for efficient operation in the nonlinear regime. At a wavelength of 2000 nm, they allow for nonlinear coefficients even of the order of 10^2 W^{-1}km^{-1} (Table 3.4).

Table 3.4. Geometry, linear and nonlinear properties of all-normal dispersion PCFs

No.	Fiber (type, material, way of introducing birefringence)	n2 [×10-20 m2/W]	Aeff [μm2]	Estimated nonlinear coefficient (γ) [1/W/km]	core / photonic cladding dimensions (μm)	local maximum of dispersion	Ref.
1	NL38, F2/SF6 all solid glass PCF	21	4 (1550 nm)	213.7 (1550 nm)	2.6×2.6 / 27.6×24.2	-31.0 ps/nm/km, 1724 nm	[52]
2	NL48, F2/SF6 all solid glass PCF with stress areas	21	5.8 (2000 nm)	113.7 (2000 nm)	2.5×2 / 24.5×18.7	-76.9 ps/nm/km, 1533 nm, -81.3 ps/nm/km, 1520 nm	[43]
3	NL46, F2/SF6 all solid glass PCF with elliptical core	21	5.4 (2000 nm)	122.2 (2000 nm)	2.7×1.9 / 25.8×16.3	-51.7 ps/nm/km, 1645 nm, -56.3 ps/nm/km, 1653 nm	[43]

3.3 Birefringence of Polarization maintaining PCFs

Strong birefringence is the key parameter controlled at the design stage of many PM fibers. In a highly birefringent fiber, the two orthogonal polarization modes $\beta_x(\lambda)$ and $\beta_y(\lambda)$ experience different propagation constants due to slightly varying refractive indices n_x and n_y respectively. When the light is launched into the fiber leading to the excitation of one of the fiber's polarization modes, the coupling between two modes is greatly reduced and the state of polarization is maintained along the fiber. The magnitude of the birefringence is characterized by the beat length $L_B(\lambda)$ of two polarization modes, which is defined as

$$L_B(\lambda) = \frac{2\pi}{\beta_x(\lambda) - \beta_y(\lambda)} \quad (3.10)$$

the phase birefringence $B(\lambda)$ can be expressed as

$$B(\lambda) = n_x - n_y = \frac{\lambda}{L_B(\lambda)} \quad (3.11)$$

and the group birefringence $G(\lambda)$ as

$$G = B(\lambda) - \lambda \frac{dB(\lambda)}{d\lambda} \quad (3.12)$$

3.3.1 Experimental setup for Birefringence measurement

My work for preparing of the amplifier setups discussed in the following sections involved assessment of the group birefringence for generation of polarized SC seed signals. For these measurements, I used a simple experimental setup based on the standard crossed polarizer method as shown in figure 3.13.

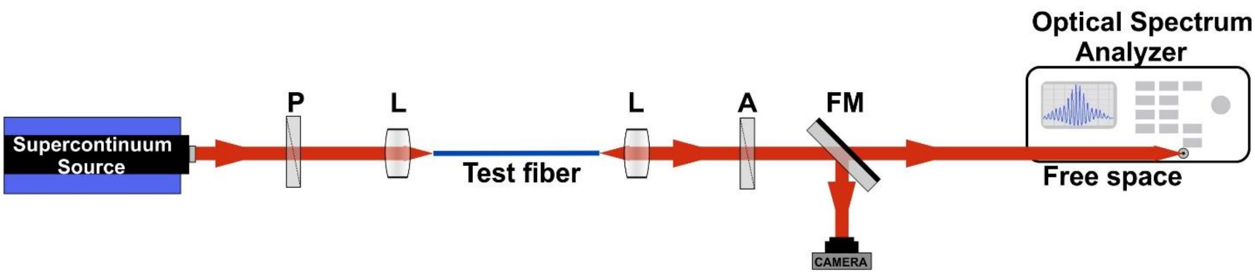

Figure 3.13. Experimental setup for group birefringence measurement P – polarizer, L – lenses, A – polarization analyzer, FM – Flip mirror.

Similar to the dispersion measurement, a SC source was used, and the light was coupled into the fiber with an aspheric lens. The output light from the fiber is collimated with a similar aspheric lens as used in input and light is coupled into the OSA over free space. The coupling efficiency into the fiber and the mode structure was monitored using an IR camera and a flip mirror. The broadband linear polarizer at the input was adjusted in such a way to excite both polarization modes in the fiber and analyzer at the output was oriented to obtain the interference birefringence pattern.

3.3.2 Results and discussion

Group birefringence (G) is obtained from the recorded interferogram using the following formula:

$$G = \frac{{\lambda_0}^2}{\Delta\lambda . L} \quad (3.13)$$

Where λ_0 and $\Delta\lambda$ are the average wavelength and the distance between the two successive fringes, respectively, and L is the length of the fiber sample used in the measurement.

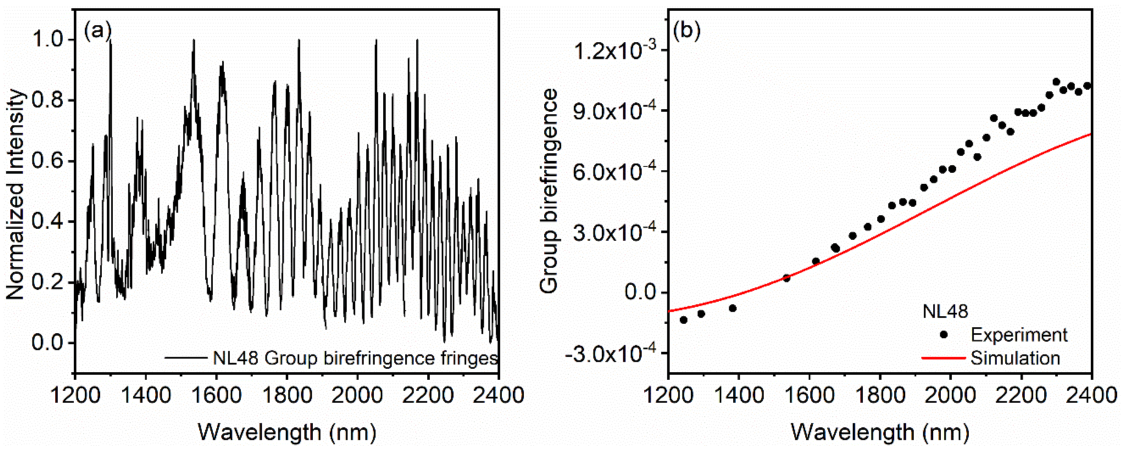

Figure 3.14. (a) Interference fringes for group birefringence (b) Group birefringence comparison between simulated [43] (solid) and experimental (dots) obtained for an NL48 fiber in the range of 1200 to 2400 nm.

Figure 3.14 (a) presents interference fringes obtained in group birefringence measurement of the "bow-tie" NL48 fiber. Coupling to the PCF was adjusted to observe the highest possible contrast fringes. The intensity in the y-axis was normalized and fringes from different spectral regions were stitched. The wide fringe around 1400 nm is the zero-group birefringence wavelength. Figure 3.14 (b) shows the close agreement of group birefringence results with the results of numerical simulations obtained by D. Dobrakowski [43]. The sign of group birefringence cannot be determined experimentally, so it was established by comparing it with the profile obtained from numerical simulations.

Figure 3.15 (a) presents interference fringes obtained for group birefringence of the NL46 fiber. The birefringence characteristic measured for the elliptical fiber, shown in figure 3.15 (b). The measurements, in agreement with theoretical data obtained from simulations in [43] revealed, that group birefringence changed sign around roughly 1500 nm and increased with wavelength up the order of 10^{-3} at about 2000 nm, as shown in figure 3.15 (b). (b). This result obtained with the NL46 fiber was favorable for the design of all-PM ultrafast fiber amplifier discussed in a later chapter of this dissertation, because it provides the broad spectrum and reasonable polarization extinction ratio of the SC seed signal generated in this fiber.

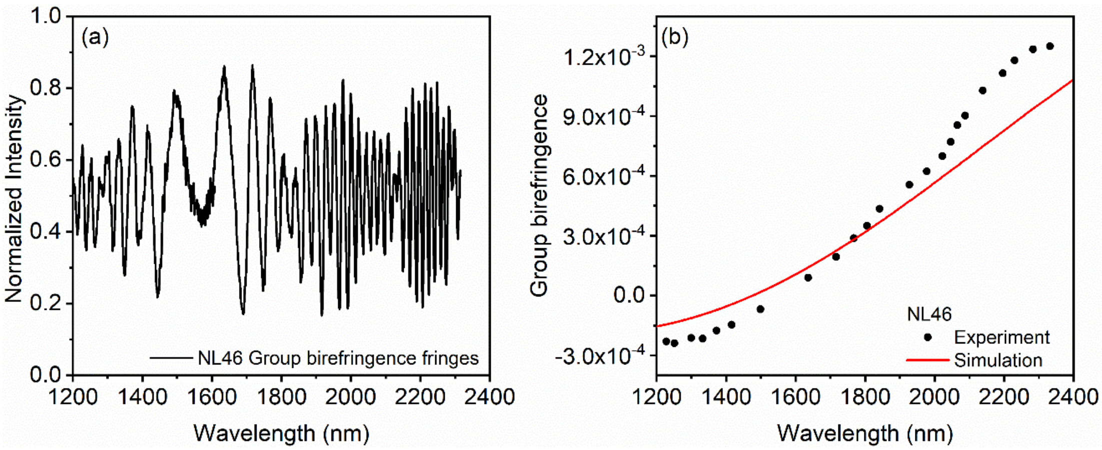

Figure 3.15. (a) Interference fringes for group Birefringence (b) Group birefringence comparison between simulated [43] (solid) and experimental (dots) obtained for an NL46 fiber in the range of 1200 to 2400 nm.

A summary of birefringence parameters of the soft glass fibers examined in my work for application in coherent SC generation for seed signals for Erbium and Thulium doped ultrafast fiber amplifiers is shown in table. 3.4, in comparison with literature results of birefringence in all-normal dispersion PCFs.

Table 3.5. Birefringence results obtained in all-normal dispersion PCFs for wavelength ranges of the three rare-earth-doped fiber-based femtosecond lasers.

No.	Fiber (type, material, way of introducing birefringence)	ca. 1000 nm (Yb^{3+} fs laser)	ca. 1560 nm (Er^{3+} fs laser)	ca. 2000 nm (Tm^{3+} + Ho^{3+} fs laser)	Reference
1	ANDi PCF optimized for 1000 nm, silica glass, bow-tie (NKT Photonics, NEG-1050-PM)	$4.2 \cdot 10^{-4}$	-	-	[39]
2	ANDi PCF opt. for 1500-2000 nm, Ge: silica, stress rods	-	$1.4 \cdot 10^{-4}$	$1.7 \cdot 10^{-4}$	[43]
3	ANDi PCF opt. for 1500-2000 nm, silicate soft glass, elliptical NL46, used in experiments described in chapter 5	-	0 (group)	$6.6 \cdot 10^{-4}$ (group)	[43]
4	ANDi PCF opt. for 1500-2000 nm, silicate soft glass, bow-tie, NL48	-	$1 \cdot 10^{-4}$ (group)	$6.1 \cdot 10^{-4}$ (group)	[43]

3.4 Summary

In the first part of this chapter, I presented and discussed the measurement results of chromatic dispersion in a series of commercially available ultra-high numerical aperture fibers. Widely used for dispersion management in ultra-fast fiber laser cavities, the dispersion values of these fibers were previously estimated based on calculations with measurement data scarcely available. To address this shortcoming, I employed a spectral interferometry-based dispersion measurement method. I validated my measurement procedures by measuring dispersion in a standard SMF-28 fiber with a good agreement with the catalog values in a wide spectral range. The results are presented in terms of the dispersion parameter D and the group velocity dispersion β_2. The results were compared with the values available from the literature, with the focus on the 2000 nm wavelength range. The published theoretical dispersion values generally overestimate the dispersion compared to the results from my work. However, I observed good agreement with previously published narrowband or single-wavelength experimental values based on autocorrelation, interferometry, or total cavity dispersion measurements, where available [146,148,149,153]. These results are also important for the fact that the available literature dispersion data on the UHNA series of fibers was provided at single wavelengths. The main focus of my dissertation is coherent seeding of ultrafast fiber amplifiers. This involves operation over a wide bandwidth and the thulium-doped fiber amplifiers possess the widest gain band among the three main fiber amplifiers (alongside ytterbium and erbium fiber amplifiers). Thus, results obtained in this study fill an important gap in the background designing of the fiber amplifier setups investigated in my dissertation.

In the last part of this chapter, I presented results of the characterization of the physically developed all-solid glass, all-normal dispersion, non-PM, and weakly-PM photonic crystal fibers. As shown in later sections of my dissertation, the application of ANDi SC as a seed signal to a 2000 nm gain band fiber amplifier enables a remarkable improvement of noise performance over soliton-seeded systems. Replacing a non-PM ANDi fiber at the seed signal generation stage with an even weakly-PM ANDi PCF enabled further enhancement in that regard. The measured dispersion of non-PM ANDi PCF and two PM ANDi PCF fibers with bow-tie stress and elliptical core show very good agreement with numerical results, which were obtained in collaboration with D. Dobrakowski [43]. The developed fibers confirm the feasibility of obtaining weakly-PM functionality by group birefringence measurements while preserving a normal dispersion characteristic over wavelengths matching the mature and emerging optical fiber amplifiers based on erbium and thulium and holmium dopants.

The measured dispersion data of commercial fibers and the developed ANDi PCFs has been applied directly in building ultrafast fiber amplifiers, which use a thulium/holmium fiber amplifier and a non-polarized, femtosecond pumped ANDi SC seed [63,162]. In chapters 5 and 6, I further discuss the importance of PM ANDI PCF and dispersion of PM2000D utilized in building all PM Thulium and Erbium fiber amplifiers.

Chapter 4. Spectro-temporal characterization

Optical fibers with engineered, normal chromatic dispersion characteristics take a special place in ultrafast fiber optics due to their applications in chirp management in mode-locked fiber laser oscillators [164] and in coherent SC generation [64]. In nonlinear fiber optics, normal dispersion fibers bring the advantage of suppressing modulation instability and Raman effect at sufficiently short pulse durations [65], which are associated with quantum noise amplification in the anomalous dispersion region [28]. Therefore, fibers exhibiting ANDi profiles are capable of producing spectrally broadband and coherent SC over a wide range of pump pulse parameters [32,65]. Light pulses with spectra spanning a full octave, obtained in ANDi fibers pumped with femtosecond Titanium:Sapphire lasers, have been compressed down to the single optical cycle regime [68], and have also been used as seed signal for high repetition rate single-cycle optical parametric chirped-pulse amplifier systems [165], enabling high harmonics generation and isolated attosecond pulse generation at high average powers [166]. Broadband and temporally uniform ANDi SC pulses in the near-infrared, pumped by ultrafast Ytterbium:fiber lasers, have found applications in various fields of ultrafast photonics, e.g. nonlinear bio-photonic imaging, micro-spectroscopy, optical coherence tomography, and multidimensional ultrafast spectroscopy [167–170]. Using fibers made from chalcogenide glasses and using optical parametric amplifiers as pump source, several implementations of ANDi SC sources with spectral coverage in the mid-IR up to 12 µm have recently been demonstrated for application in vibrational spectroscopy [44,171]. However, especially promising is the combination of ANDi fibers with femtosecond pump sources based on Erbium- (Er):fiber technology as this allows the construction of compact and robust all-fiber coherent SC sources [45,172]. Applied as a broadband coherent seed, such systems have recently formed the basis for the realization of ultra-low noise frequency combs and ultrafast fiber amplifier systems in the 2 µm spectral range [63,162,163].

Many of these applications benefit from SC with uniform and smooth spectral and temporal intensity profiles. ANDi SC pulses are often assumed to fulfill these requirements, backed up by many numerical simulations available in literature covering various fiber designs and pump wavelengths (e.g. [33,44–48]). However, detailed experimental data on the spectro-temporal characteristics of ANDi SC pulses is scarce [49,50], yet such measurements are necessary to evaluate the properties of ANDi SC and its suitability for specific applications under real pumping conditions. In contrast to numerical simulations, which typically assume ideal Gaussian or hyperbolic secant pulse shapes, femtosecond pulses emitted by real lasers often exhibit imperfections. While it is known that non-ideal pulse shapes can have a significant effect on the spectro-temporal properties of the generated ANDi SC [173], their impact has not been assessed experimentally so far. The often complex spectro-temporal correlations of SC pulses can be conveniently visualized using spectrograms created via cross-correlation optical gating. The analysis of such experimentally recorded or numerically simulated spectrograms has contributed significantly to the understanding of the nonlinear dynamics involved in SC generation under various pumping conditions [65,125,174,175]. More recently, measurements of spectrograms have been used to optimize fiber SC generation for specific applications [176], for dispersion measurements of birefringent photonic crystal fibers (PCF) [177], and the characterization of optical rogue waves [130].

In this chapter, I present and discuss the spectro-temporal characterization of coherent supercontinuum pulses obtained in microstructured PM and non-PM ANDi PCFs using XFROG. Experimental spectrograms were recorded and analyzed using time-domain ptychography (TDP) [132], which is especially suitable for the measurement of complex, spectrally broadband ultrashort pulses [138–140]. ANDi fibers compatible with pumping from 1560 nm femtosecond lasers are of practical importance for coherent, broadband seeding of ultrafast fiber amplifiers. The reason for this is that the investigated SC pulses overlap spectrally the gain bands of erbium- and thulium-doped optical fibers, while the all-positive chirp of investigated SC seed signals facilitates chirp management in pair with these gain fibers, which are typically negatively chirping.

Significant parts of the results presented in this chapter were published in the form of a research paper, which appeared in Optics Express [178].

4.1 Experimental setup

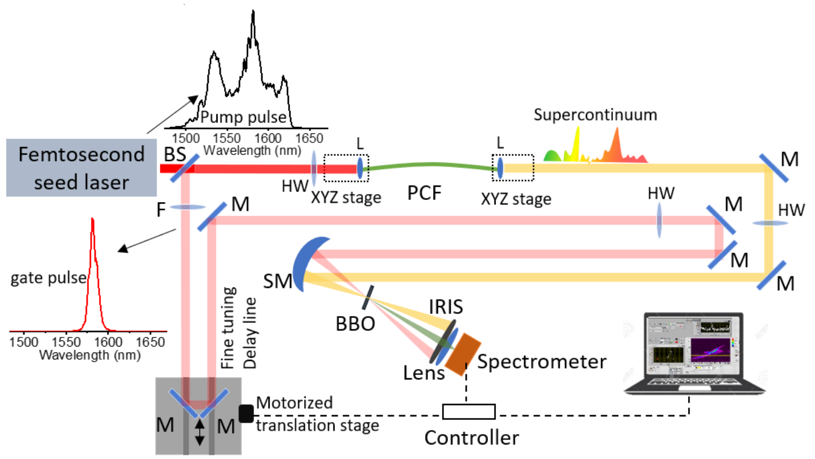

Figure. 4.1. Experimental setup for ptychographic pulse characterization: femtosecond seed laser: 1560 nm, 100 MHz, 350 mW, 75 fs (Menlo Systems C-fiber HP); BS: beam splitter; F: 1580 nm bandpass filter; PCF: photonic crystal fiber; M: highly reflective mirror; HW: half-wave plate; L: aspheric lens; SM: spherical mirror; BBO: β- barium borate crystal.

Spectro-temporal characterization of the SC pulses was performed using TDP [132]. The required spectrograms for ptychographic reconstruction of the pulses are recorded with the use of a standard, in-house built sum-frequency generation-based cross-correlation optical gating setup shown in figure 4.1 [30,114,125,138,140]. As a pump source, I used a commercially available Er:fiber-based laser (Menlo Systems C-fiber HP), operating at a central wavelength of 1560 nm, with a 100 MHz repetition rate, delivering 75 fs pulses with an average power of 350 mW, which corresponds to around 40 kW of peak power. The pump signal was split into two beams with a 90:10 ratio beam splitter (BS). The 90% part of the pulse energy was used to pump SC generation in the PCF, while the other 10% was used as gate pulse.

The femtosecond pump laser spectrum is depicted in the setup figure 4.1 in the pump arm. The light was coupled into the fibers through an aspheric lens with a focal length of 4 mm and an anti-reflection coating compatible with the pump laser spectrum. In the case of the PM fibers, a 1560 nm half-wave plate was used to match the linearly polarized pump pulses to one of the principal axes of the fibers. The PCFs were mounted onto a 3-axis translation stage for precise control of the input condition. The generated SC is collimated using an outcoupling lens. A polarizer was placed at the output of these PCFs to assess the state of polarization of light exiting the fibers. Polarization extension ratio (PER) was measured by analyzing the average power and spectrum differences at the end of fiber by pumping PCFs in one axis and measuring output signal in the same and opposite axes. An optical spectrum analyzer (OSA, operating wavelength 1200 -2400 nm) was used to record independent SC spectra, which is required to correct the measured spectrograms.

The gate pulse was formed by filtering 10% of energy from the pump pulse using a 14 nm bandpass filter of 1580 nm central wavelength, which coincides with the main peak of the pump spectrum. In comparison to the unfiltered pump pulse, the filtered gate pulse with its quasi-Gaussian spectrum results in much simpler and cleaner spectrograms, facilitating their interpretation and reconstruction. It as to be noted that in TDP the obtainable temporal resolution is independent of the gate pulse duration such that spectral filtering does not result in the loss of any information [132,140]. A motorized piezo-driven delay stage is used for precise control of the time delay between gate pulse and SC pulse.

Spectrally broad and chirped SC pulses from the PCFs and the filtered gate pulse were focused on the BBO crystal by a spherical mirror. Here I used a 0.5 mm β-barium borate crystal (BBO) with type I phase-matching for sum-frequency generation (SFG). The SFG signal was recorded as a function of the time-delay between SC and gate pulse using a compact Czerny-Turner spectrometer (Ocean Optics, 350 – 1000 nm sensitivity range, 2.0 nm resolution). The polarization state of both pulses was controlled with broadband half-wave plates. Any unconverted SC and reference pulse light transmitted through the BBO crystal was filtered with an iris before the spectrometer. The large phase-matching bandwidth required to generate an SFG signal for all frequencies contained in the SC pulse is a challenge that was addressed by recording three spectrograms with different BBO tuning angles and overlapping them in order to obtain an SFG signal with sufficient signal-to-noise ratio at the extremes of the SC spectrum. The measured spectrograms were corrected for all frequency-dependent effects, including the BBO phase-matching efficiency, by comparing the spectral marginal to the cross-convolution of independently measured SC and probe pulse spectra and enforcing agreement of these two quantities [179]. Standard background correction and noise filtering were applied.

Extended ptychographic iterative engine (e-PIE) was used for the extraction of the full amplitude and phase information of both the SC pulse and the gate pulse simultaneously from a single spectrogram [139,140].

4.2 Characterization of the pump laser pulse and gate pulse

I characterized both the pump and gate pulses using second-harmonic frequency-resolved optical gating (SHG-FROG) and a retrieval algorithm based on generalized projections [114,131]. The pump pulse temporal amplitude and phase are required as input for numerical simulations as described in Section 4.3.1, while the measurement of the gate pulse serves as an additional independent measure of accuracy for the subsequent, more demanding SC spectrogram reconstructions using e-PIE. As the e-PIE algorithm reconstructs both SC pulse and gate pulse, I can then easily determine the accuracy and convergence of the reconstruction by ensuring the equivalence of e-PIE and SHG-FROG results for the gate pulse.

The results for the pump laser are shown in figure 4.2. The retrieved spectrogram accurately reproduces the experimental data with an error of 1.9×10^{-3}. The temporal and spectral full width at half maximum (FWHM) of the pump pulse were determined to be 75.3 fs and 92 nm, respectively. The pump pulse also displays pre- and post-pulses with peak intensities of about 10% of the main pulse, and a pedestal on the -20 dB level especially pronounced on the trailing edge of the pulse reaching out to about 1 ps, as highlighted in the logarithmic scale plot in figure 4.2. Such features are common in high pulse energy, sub-100 fs Er:fiber amplifier systems [180].

The SHG-FROG results of the gate pulse filtered with the 1580 nm bandpass filter are shown in figure 4.3. The retrieval error was 1.1×10^{-3}. The gate pulse had 337.5 fs FWHM duration and a 14 nm spectral width. Spectral filtering removed side pulses and the low-level pedestal, also pulse shape in both temporal and spectral domain were quasi-Gaussian. This corresponded with the low value of retrieval error. Compared to the original output pulses of the laser, the filtered pulses are more suitable to use as gate pulses, because they generate clearer cross-correlation spectrograms, in which any complex features can uniquely be attributed to the SC pulse. In addition, the longer gate pulse duration does not have any negative impact on the obtainable temporal resolution of the TDP technique [132,140].

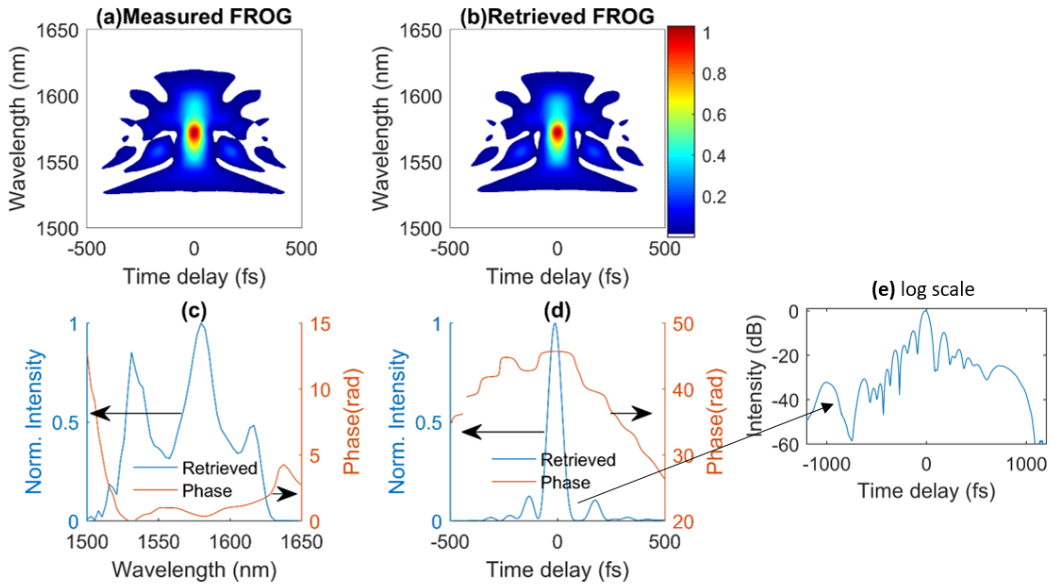

Figure 4.2. Characterization of the pump pulse using SHG FROG. (a) Measured FROG trace, (b) retrieved FROG trace, (c) retrieved spectrum (blue) and phase (orange), (d) retrieved pulse shape (blue) and phase (orange), and (e) temporal intensity in logarithmic scale.

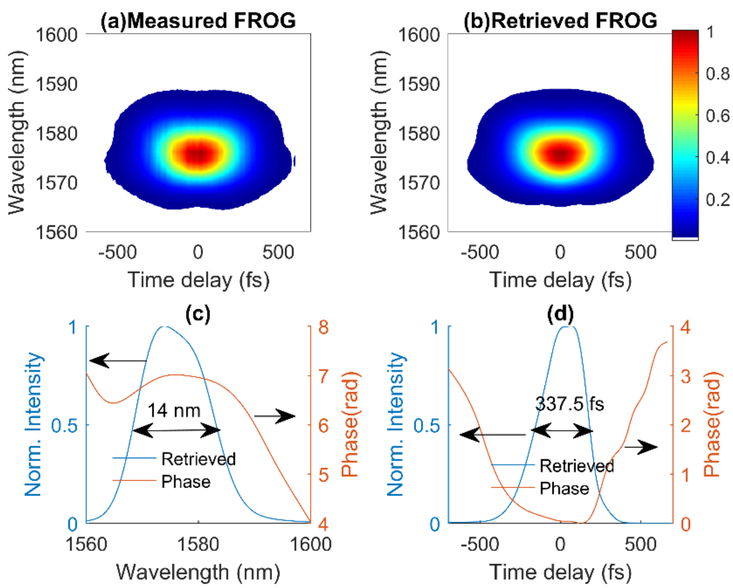

Figure 4.3. Characterization of the gate pulse after the bandpass filter using SHG FROG. (a) Measured FROG trace, (b) retrieved FROG trace, (c) retrieved spectrum (blue) and phase (orange), (d) retrieved pulse shape (blue), and phase (orange).

4.3 Spectro-temporal characterization of SC pulses

In this section, I discuss the spectro-temporal characterization of coherent SC pulses generated in two sets of microstructured ANDi PCF pumped by a commercial ultrafast Er:fiber amplifier system. (i) all-solid silicate glass PM and non-PM PCFs labelled NL46, NL48, and NL38, the detailed chromatic dispersion, and birefringence properties were discussed in the previous chapter. (ii) silica/Ge:silica core PM PCFs labelled NLs1, NLs2 developed at the Laboratory of Optical Fiber Technology, Maria Curie-Sklodowska University in Lublin, Poland. All PCFs are pumped by Er:fiber-based laser (Menlo Systems C-fiber HP), as described in section 4.1 The coupling efficiency estimated based on the ratio of the incident pump power to the SC output average power and considering the attenuation of the used fiber section, was in the case of the silicate PCFs labelled NL46, NL38, and NL48 around 46%, 36%, and 26%, respectively, while in the silica PCFs labelled NLs1 and NLs2 it was around 65%.

4.3.1 Soft-glass PCF: NL46 fiber (PM)

I first characterized the SC pulse generated in NL46 PM PCF using a 10.4 cm long sample. Here I used one of the fibers from NL46 series which has a similar chromatic dispersion profile to the NL38 series fibers. Because of this, I expected similar performance in terms of SC spectral width, with the added benefit of a determined polarization state of light. The NL46 fiber sample used enabled SC generation covering wavelengths up to 2150 nm as shown in figure 4.4. SC spectra measured in both polarization axes are similar in broadening and PER is around 10 dB. Taking longer samples did not enable a wider spectrum under the available pumping conditions, which is attributed to a combination of factors including the increasing slope of normal dispersion and increasing mode area (decreasing nonlinear response of the fiber) similar to what had been discussed for the NL38 fibers [52].

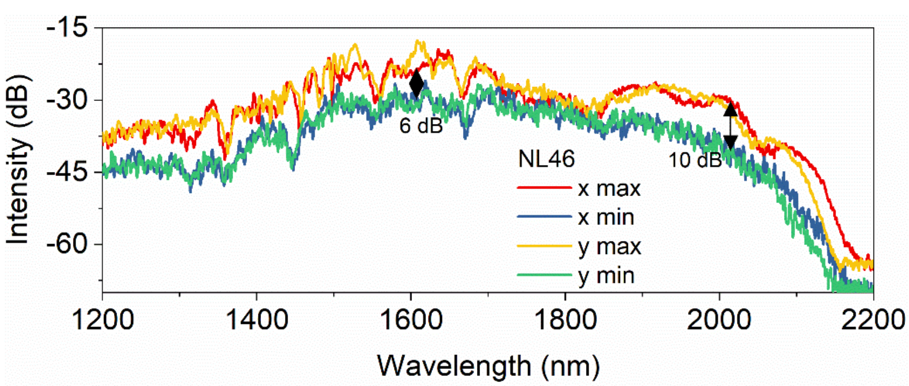

Figure 4.4. Supercontinuum generated in NL46 fibers in both x and y-axes; max -pumped and observed in the same axis, min -pumped and observed in the opposite axis.

Figure 4.5 summarizes the measurement results and the excellent quality of the pulse retrieval achieved by the e-PIE algorithm. All intricate details of the measured spectrogram shown in figure 4.5 (a) are very well reproduced in the retrieved spectrogram shown in figure 4.5(b), resulting in minimal errors not exceeding ±0.2% across the entire, nearly octave-spanning width of the SC pulse spectrum as shown in figure 4.5 (c). The high fidelity of the reconstruction is underlined by the excellent agreement of the retrieved spectrum with an independently measured SC spectrum using the OSA, as shown in figure 4.5(d).

The general shape of the spectrogram confirms nonlinear broadening dynamics, which is typical for SC generation in normal dispersion fibers under femtosecond pumping. These are dominated by self-phase modulation (SPM) and optical wave breaking (OWB), preserving the temporal integrity of the SC pulse [32,64]. In our pumping conditions, the optical wave breaking length scale (L_{WB}) is < 1 cm in this fiber, i.e. SC generation dynamics are concluded and the spectrum fully developed at the exit of our fiber sample [64]. L_{WB} is of similar magnitude also in the other investigated soft-glass PCF discussed below. This also supports the selection of the fiber sample length, which is longer, than the length required for the SC broadening process to complete. Therefore, roughly 10 cm sample length selected for this and the following experiments in this work, was also motivated by convenience of handling. Going back to the group delay characteristics shown in figure 4.5 (a), it can be observed, that the chirp of the SC pulse is positive and predominantly linear from 1300 nm to 2100 nm.

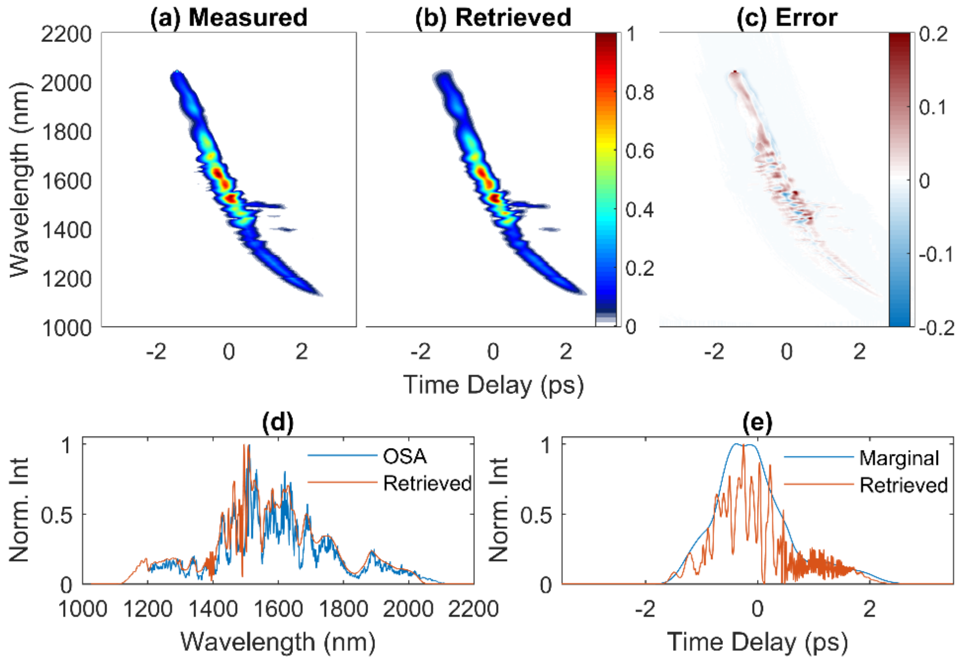

Figure 4.5. Spectro-temporal characterization of SC pulses generated in the NL46 PCF. (a) Measured spectrogram. (b) retrieved spectrogram using e-PIE. (c) Error calculated by subtracting (a) from (b). (d) Retrieved spectrum compared to an SC spectrum independently measured with the OSA (linear scale). (e) Retrieved temporal pulse shape with marginal.

Figure 4.5(e) shows the SC pulse shape retrieved by e-PIE, which was characterized by substantial modulation, fine structure, and fast oscillations on time scales much shorter than the original pump pulse. In contrast, in the temporal marginal, which is directly accessible from the spectrogram measurement, these features are masked since any structure shorter than the gate pulse duration (340 fs) cannot be resolved. In this situation, the ptychographic pulse reconstruction can be used to reveal these temporal fine details. The modulated pulse shape and the complex features observed in the spectrogram differ considerably from the smoothness and simplicity typically obtained in numerical simulations (e.g. [33,44–48,64]), and also from observed in previous spectro-temporal characterizations of ANDi SC pulses [32,50].

Since the similar temporal fine structure was observed in all investigated fibers in this work, as discussed in the following sections, we performed numerical simulations in order to clarify the origin of these features. The simulation is based on the generalized nonlinear Schrödinger equation (GNLSE) [29,84] using the measured dispersion profile and nonlinear properties of NL46 given in the figure 3.12 and table 3.4 as well as the real pump pulse amplitude and phase obtained from the FROG measurements (figure 4.2(d)).

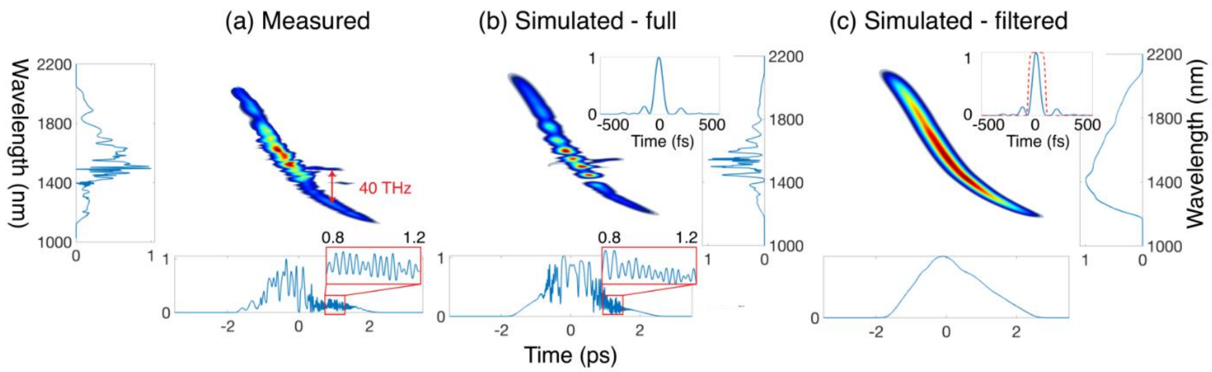

Figure 4.6. Projected axes spectrograms of SC pulses generated in NL46 PCF. (a) Measured; (b) simulated considering full amplitude and phase of measured pump pulse; (c) simulated considering temporally filtered pump pulse without side-peaks or pedestal. The projected axes show the retrieved or simulated spectral and temporal profiles, respectively, both in linear scale. Top insets in (b) and (c) show the pump pulse shape considered in the respective simulations.

In figure 4.6 (a), (b) the measured and simulated spectrograms are compared. The projected axes show the retrieved and simulated spectral and temporal profiles, respectively. The simulation, which included the measured spectro-temporal characteristics and the retrieved phase profile of the pump pulse reproduced the observed complexity of the spectrogram and temporal profile of the generated supercontinuum pulses with very high accuracy, which also serves as an additional independent confirmation for the validity of the ptychographic pulse reconstruction used in my work. Minor differences between the simulated and measured spectrograms are attributed to uncertainties of the measured fiber properties and the propagation of the measured SC pulse through several dispersive optical elements after exiting the fiber. The shortest temporal features in both measured and simulated temporal pulses are oscillations at time delays of 0.8-1.2 ps shown in the insets. These fast oscillations are due to the beating caused by the temporal overlap of the SC spectrum with a long and spectrally narrow feature around 1530 nm. Using the simulation, this feature can be traced back to the unconverted low-level pedestal of the pump pulse, which was identified in the characterization of the pump pulse in Section 4.2 and is well visible in figure 4.2(e). The beat frequency is equal to the spectral separation of pump pedestal and overlapping SC spectrum, which from the spectrogram can be determined to be ~ 40 THz. The resulting expected oscillation period is 25 fs, which matches well with the simulated results.

In fact, all the observed modulation and fine structure of the SC pulse in both spectral and temporal domains can be traced back to the pump pulse. In figure 4.6(c) simulations was repeated using exactly the same parameters but applied a super-Gaussian filter to the measured pump pulse isolating the main peak and suppressing side pulses and pedestal. In this way, all the complexity disappears, and the smooth temporal and spectral profiles usually associated with ANDi SC can be recovered. Hence, the non-ideal pulse shape emitted by the Er:fiber pump laser can be clearly identified as the origin of the temporal (and spectral) fine structure of the SC pulse observed in our measurements.

We note that there is a low-level noisy feature in the measured spectrogram at coordinates of approx. 1400 nm / +1-2 ps, which is not reproduced by the simulation. This proves that this feature cannot be explained by single-polarization nonlinear dynamics. Instead, in section 4.3.2 we link this feature to the occurrence of PMI, which is associated with the depolarization of the SC pulse.

4.3.2 Soft-glass PCF: NL48 (PM) and NL38 (non-PM) fiber

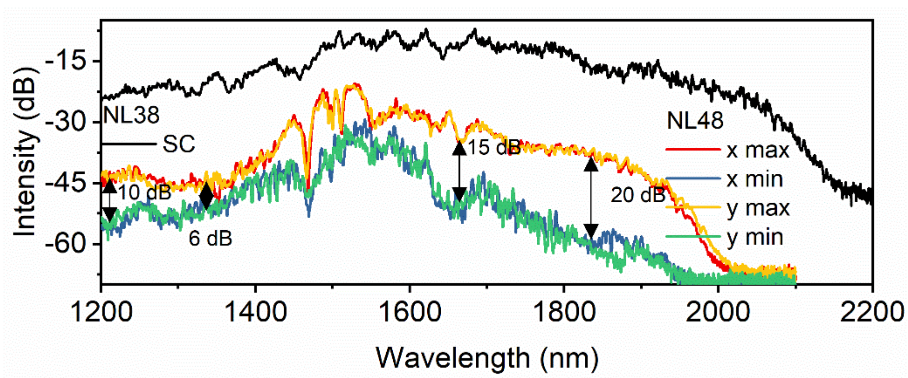

Figure 4.7. Supercontinuum generated in both NL48 and NL38 non-PM fiber, In PM case SC is measured both x and y-axis; max -pumped and observed in the same axis, min -pumped and observed in the opposite axis

SC was measured in both NL48 PM and NL38 non-PM fiber with roughly similar length of the fiber samples and respective spectrum broadening is as shown in figure 4.7. The NL38 fiber is the base design as discussed in the previous chapter with the SC spectrum spanning from 1100 to 2150 nm. The modified structure NL48 with bow-tie stress areas enabled SC generation up to 2000 nm measured in both the axes. This fiber exhibits 15 dB PER, which is better compared to NL46 design. But the reduced spectral broadening during SC is assigned to much higher normal chromatic dispersion than the NL38 and NL46 designs.

Figure 4.8(a) shows the measured spectrogram of the SC pulse generated in a 10.1 cm sample of NL48 PM PCF. The spectral projection contains the spectrum retrieved by e-PIE compared to an independent OSA measurement, confirming a high fidelity pulse reconstruction. The temporal projection displays the marginal of the spectrogram as well as the intensity and phase retrieved by e-PIE. The temporal modulation and beating effects due to the non-ideal pump pulse shape discussed above for the NL46 fiber are also clearly visible. The pulse duration is longer (5.9 ps) and the spectrum narrower compared to the measurements using the other soft-glass PCF, which is in agreement with the stronger chromatic dispersion of the NL48. The spectrogram also highlights an almost perfectly linear chirp of the pulses without significant higher-order dispersion contributions.

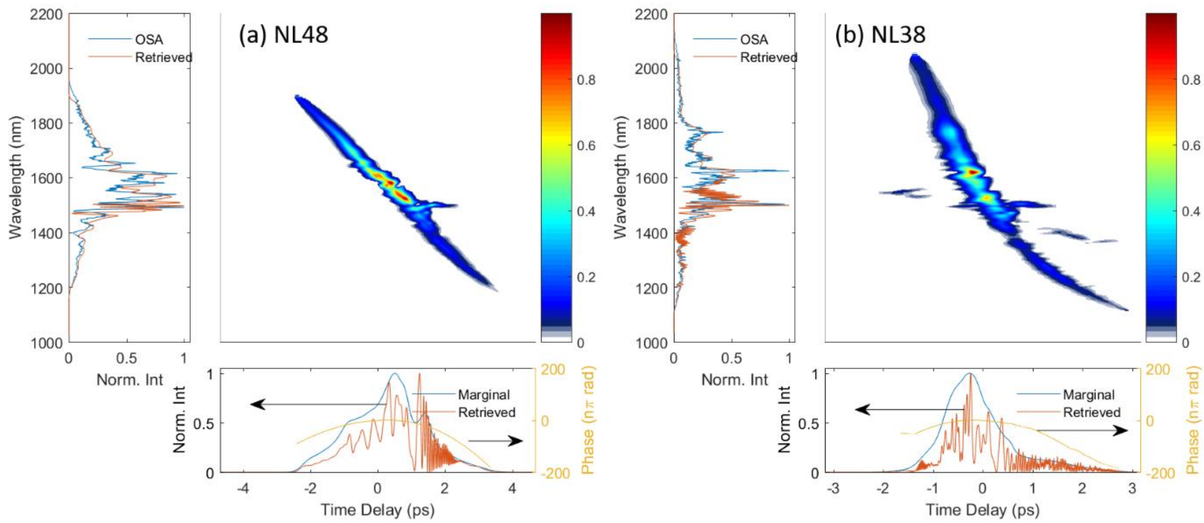

Figure 4.8: Measured projected axes spectrograms of SC pulses generated in soft-glass PCF. (a) NL48 – polarization maintaining. (b) NL38 – non-polarization maintaining. The spectral projection displays the spectrum retrieved by e-PIE compared to an independent OSA measurement (linear scale). The temporal projection displays the marginal of the spectrogram as well as the intensity and phase retrieved by e-PIE.

I performed similar spectro-temporal characterization measurements with a 14.4 cm sample of NL38, which is non-PM. The results are shown in figure 4.8(b). With this fiber, I observe considerably more fine structure in both spectral and temporal domains than with the corresponding PM fibers. The spectrogram trace of the main pulse is not as well defined as in the case of highly birefringent fibers and exhibits quite noisy contour lines. Additionally, spectral and temporal beating effects are caused by the appearance of low-level features at wavelength/delay coordinates of around 1600 nm / -2 ps and 1400 nm / +2 ps. Similar but weaker features were only observed in the weakly birefringent NL46 (Figure 4.5) but were completely absent in all other investigated fibers that exhibit higher birefringence. It was recently shown that nonlinear dynamics in ANDi fibers with weak or unintentional birefringence are much more susceptible to quantum noise amplification by PMI [38,41]. Hence, I believe that the noisy contour of the main trace in the spectrogram and the additional low-level features are signatures for the onset of noise amplifying nonlinear dynamics due to PMI and the nonlinear coupling of FWM and SRS, as described previously in Ref. [65].

Interestingly, a similar low-level noisy feature at the coordinates 1400 nm / +1-2 ps was also observed in the spectrogram measurements of the SC pulse generated in the NL46 fiber (Figures 4.5 and 4.6), which is the PM version of NL38. In contrast, the noisy feature at 1600 nm / -2 ps is absent in NL46. Detailed wavelength-dependent birefringence measurements of NL46 (Figure 3.15) show that the birefringence drops to zero around 1400 nm such that noise amplification by PMI is indeed possible. On the other hand, at 1600 nm NL46 exhibits a birefringence of approx. 1×10^{-4} [43], effectively suppressing PMI. These observations provide further evidence that the observed low-level noisy features are indeed caused by nonlinear dynamics related to PMI.

4.3.3 Silica/Ge:silica PM PCF: NLs1 and NLs2

Microstructured silica fibers with an elliptically shaped, germanium-doped core and birefringence induced by squeezed lattice labeled NLs1 and NLs2 are discussed here. The chromatic dispersion of NLs1 and NLs2 fiber measured in both x and y-axis is shown in figure 4.9. The measured group birefringence was around 1.65×10^{-5} and 4.46×10^{-5} for NLs1 and NLs2, respectively. At a wavelength of 2 μm, estimated nonlinear coefficient (γ) was 4 W^{-1} km^{-1}. The NLs1 fiber has an almost perfectly flat ANDi profile and NLs2 effectively exhibits zero-dispersion over a very wide wavelength span around 1600 - 2200 nm. The dispersion measurement with the balanced Mach-Zehnder interferometer yields a local maximum of 0.64 ps/nm/km (± 0.1 ps/nm/km) at 1834 nm and two ZDWs around 1660 nm and 2050 nm. The error of the ZDW positions in the dispersion measurement is approx. ± 12 nm.

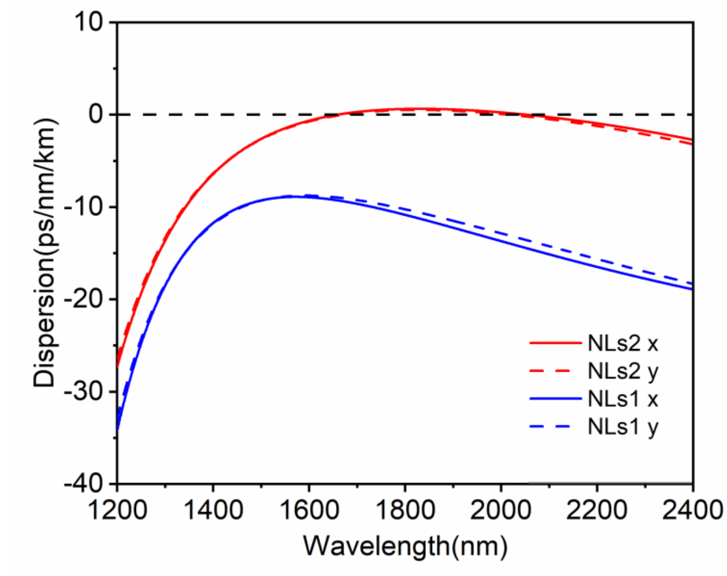

Figure 4.9 Chromatic dispersion of NLs1 and NLs2 fiber measured in both x and y-axis.

The silica PCF exhibit much lower nonlinearity than the tested soft-glass PCF (Table 3.4). This is partly offset by a remarkably low loss estimated below 0.1 dB/m around 1.75 µm [42] (compared to about 20 dB/m in the case of the soft-glass PCF) as well as weaker and flatter dispersion. The latter facilitates spectral broadening and efficient transfer of energy from the central pump wavelength to the SPM and OWB sidebands [33]. In addition, fibers with low chromatic dispersion avoid excessive pulse broadening and maintain high peak powers for longer propagation distances. Therefore, the silica PCFs in this work produce SC spectral bandwidths comparable to the investigated soft-glass PCFs.

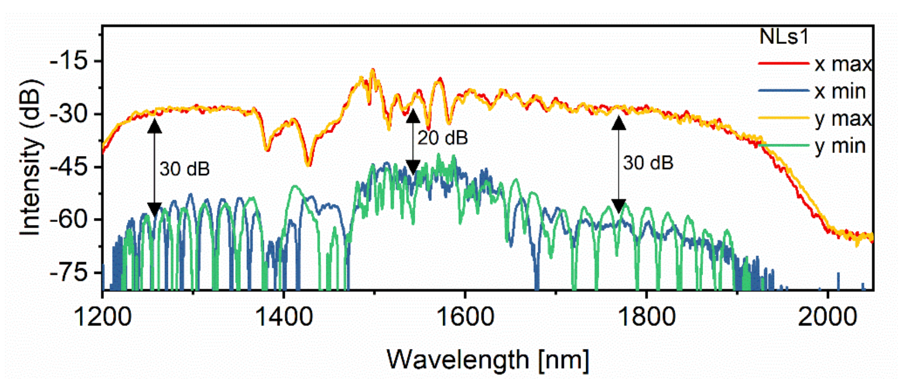

Figure 4.10. Supercontinuum generated in NLs1 fiber and measured in both x and y-axis; max - pumped and observed in the same axis, min -pumped and observed in the opposite axis.

The NLs1 fiber generates flat SC profile and maintains an excellent PER of 20-30 dB as shown in figure 4.10, but compared to the lead-silicate PCF, the spectral broadening during SC generation is reduced due to a significantly smaller nonlinearity of the base glass and reduced modal confinement at longwave near-infrared wavelengths [181].

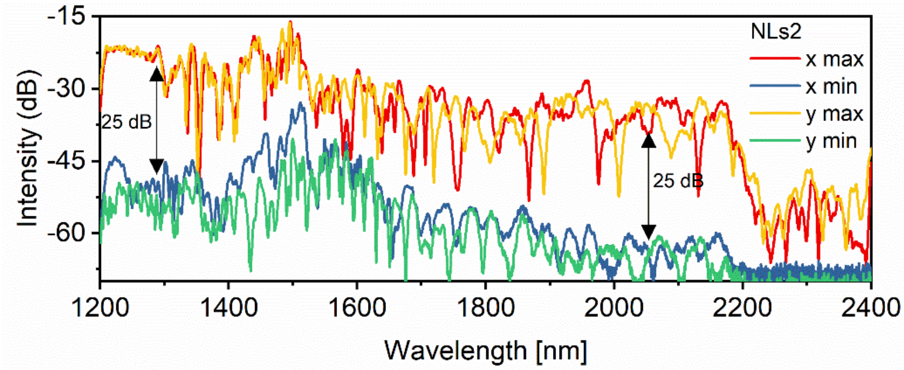

Figure 4.11. Supercontinuum generated in NLs2 fiber and measured in both x and y-axis; max - pumped and observed in the same axis, min -pumped and observed in the opposite axis

The second silica fiber labeled NLs2, I used a 1.7 m long sample to verify the SC generation and its polarization properties. The measured SC spectrum is the broadest of all investigated fibers and reaches up to 2400 nm as shown in figure 4.11. The spectrum is very complex but exhibits quite different and pronounced spectral features compared to the other fibers in this work, although PER is very high at 20-25 dB. The structured spectrum is explained by the presence of zero-dispersion wavelengths in the fiber's chromatic dispersion profile and the interplay of normal and anomalous dispersion broadening dynamics present in the fiber. Measured spectra of SC pulses generated in 10.8 cm and 30 cm long samples (and the initial 1.7 m sample measurement) are shown in figure 4.12 for one of the polarization mode components. The SC spectrum obtained from the short fiber of length 10.8 cm and 30 cm are similar. The nonlinear length scale computed for this fiber was $L_{NL} < 2$ cm and dispersion length scale L_D was in the order of 2.5 m. Hence a long piece of fiber was required for soliton formation, which can be clearly seen in figure 4.12, therefore we performed the spectro-temporal characterization with a relatively short piece of fiber.

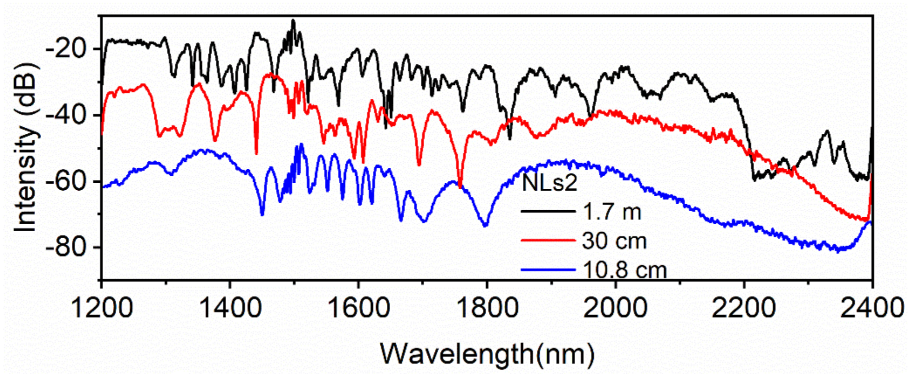

Figure 4.12. Supercontinuum generated in different lengths (shown in legend) of NLs2 fiber.

The spectro-temporal measurements of both investigated silica PCF were summarized in figure 4.13. To be directly comparable with the soft-glass PCF measurements, the spectrogram traces, spectra, and pulse shapes for these fibers were obtained for approx. 10 cm long samples. Both fibers emit much shorter SC pulses than the investigated soft-glass PCF, as the measured pulse durations were below 0.5 ps. Such pulses with broad spectral bandwidth and low chirp values are convenient for ultrafast applications, e.g. for nonlinear imaging or compression to few-cycle pulse durations. However, it is also evident from these measurements that any imperfections of the pump pulse were directly translated to the SC pulse, such as the unconverted low-level pedestal at 1530 nm which is very prominent in both measurements as shown in figure 4.13.

The NLs1 fiber exhibits all-normal chromatic dispersion, leading to a positive, practically linear chirp across the SC spectrum (Figure 4.13(a)). L_{WB} in this fiber is estimated at 7 cm, i.e. comparable to the length of the fiber sample. Consequently, the spectrum would slightly broaden and flatten with increased fiber length. Nevertheless, it is clear that spectral broadening is reduced compared to the soft-glass PCF as the dispersion is not quite low enough to completely offset the lower glass nonlinearity.

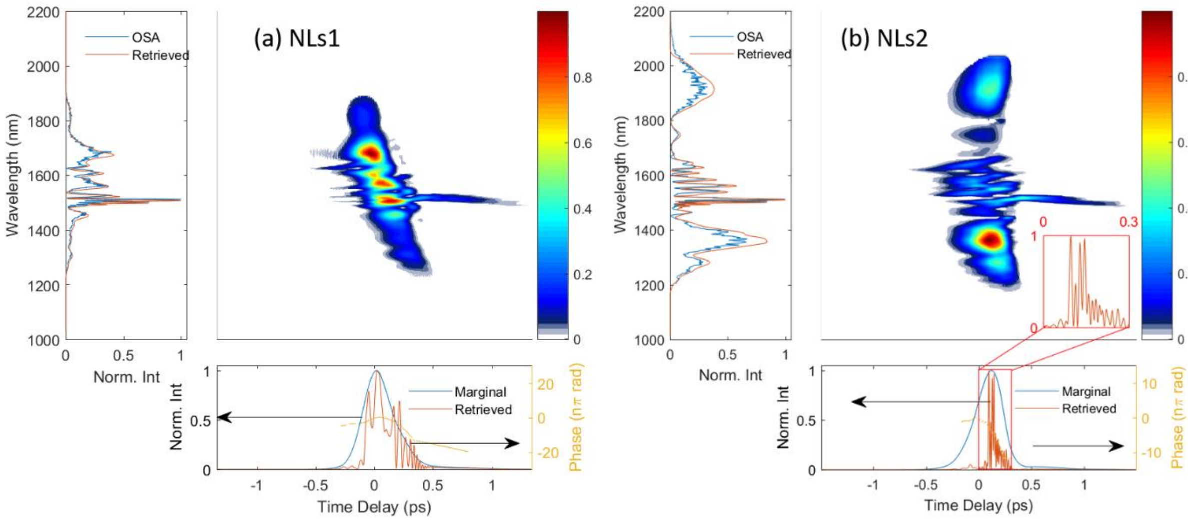

Figure 4.13. Measured projected axes spectrograms of SC pulses generated in polarization-maintaining silica PCF. (a) NLs1. (b) NLs2. The spectral projection displays the spectrum retrieved by e-PIE compared to an independent OSA measurement (linear scale). The temporal projection displays the marginal of the spectrogram as well as the intensity and phase retrieved by e-PIE. The inset in (b) shows a magnified section of the temporal intensity profile.

This is different in the case of the NLs2 fiber (Figure 4.13(b)). The very low, near-zero dispersion profile of this fiber facilitates spectral broadening equivalent to the investigated soft-glass PCFs. According to the measured dispersion profile discussed in figure 4.9, the fiber exhibits very low anomalous dispersion in the range of 1650 – 2050 nm. This is confirmed by the change of slope of the spectrogram trace around 1650 nm. The low absolute value of chromatic dispersion leads to a temporal overlap of spectrally widely separated components, resulting in high-frequency temporal beating with peak durations of ~ 6 to 8 fs, as seen in the inset of figure 4.13(b). The spectrogram is dominated by two broad peaks located at 1350 nm and 1900 nm. Simulations confirm that both peaks are generated by SPM and not by soliton fission, even the structure at 1900 nm cannot be considered a soliton although it is located in the anomalous dispersion region. The spectrogram clearly shows a chirp across its spectrum, while a soliton would exhibit a flat spectral phase. The non-formation of a soliton can be understood by considering nonlinear and dispersive length scales [79]. Soliton formation requires a certain balance of dispersion and nonlinearity [79], which is not given in our conditions. Hence, although the fiber does not strictly exhibit an ANDi profile, the SC pulse should possess the typical low-noise, high stability properties usually associated with ANDi SC generation [64,65].

4.4 Conclusions

I reported detailed experimental spectro-temporal characterization of coherent SC pulses from all-solid silicate glass and silica/Ge:silica core microstructure PCFs. Both PM and non-PM fibers investigated in this work were pumped by a commercial ultrafast Er:fiber laser/amplifier system. I used TDP to reconstruct the measured spectrograms of the SC pulses. Our measurements revealed that the SC pulses emitted from all the investigated in ANDi PCF exhibit intricate pulse shapes. Using e-PIE, we retrieved a considerable amount of temporal fine structure and fast oscillations on at the scale of 6 to 8 femtoseconds. Simulations also related the origin of the complex SC features to imperfections of the input pump pulse, such as side pulses and low-level pedestals, which are common in high energy femtosecond Er:fiber amplifier systems. In addition, I observed spectro-temporal structures in weakly birefringent fiber samples that are consistent with signatures of incoherent noise amplification due to PMI and the nonlinear coupling of parametric four-wave mixing (FWM) and stimulated Raman scattering (SRS) discussed in recent numerical studies [41,65]. These results highlight the importance of the pump source and highly birefringent, PM fibers for high-quality SC generation and provide important guidance for the design and application of ANDi SC sources in ultrafast photonics.

I have confirmed that positively and near-linearly chirped pulses are readily available from different structures of lead-silicate soft glass fibers, including variants that are PM. Here we extended this work with results on silica/Ge-doped silica PM fibers, which served to confirm that similar characteristics can be obtained from fusion splicing-compatible fibers. However, engineering of flat, ANDi profiles in silica fibers across both near-infrared gain bands of trivalent erbium and thulium ions are challenging.

All-solid silicate glass ANDi PCF enabling all-normal dispersion nonlinear dynamics with sufficient spectral coverage of the Tm-doped fiber gain band with an OWB spectral wing and with reasonable PER encouraged application in coherent, broadband seeding of ultrafast Tm-doped fiber amplifiers. The details of the design are discussed in the next chapter.

Chapter 5. Ultra-low noise coherently seeded Thulium fiber amplifier

Ultrashort pulse sources operating in the 1.9–2.1 μm are currently in demand for many applications in various scientific fields and industries. The main interests in such sources stem from their properties like wide spectral bandwidth, ultra-low noise, and high robustness. Efficient and compact laser sources operating around the wavelength of 2000 nm are widely used, for mid-infrared SC generation in photonic crystal fibers [182], pumping of optical parametric oscillators [183], as well as in spectroscopy and precision metrology. Most commonly, 2 μm femtosecond laser pulses are based on Tm- or Ho-doped silica fibers which are operated in kilowatt power level, but with limited spectral bandwidths [184,185].

Many reported ultrafast fiber amplifier systems operating in the 2 μm spectral region are coherently seeded by modelocked Erbium (Er)-fiber systems, which are spectrally broadened to the 2000 nm region via the generation of Raman-shifted solitons, four-wave mixing, or SC generation in the anomalous dispersion region of a highly nonlinear fiber [10,59–62,82,182,186,187]. This allows the straightforward extension of the maturity and excellent performance parameters of Er:fiber technology to longer wavelengths and easy power scaling. The drawback of this solution is that nonlinear dynamics pumped in the anomalous dispersion regime suffer from high sensitivity to quantum noise, leading to white-noise fluctuations of amplitude and phase of the spectrally broadened seed signal usually associated with modulational instability (MI) [28,29,66,188]. As a result, the noise performance of the 2 μm system is inherently degraded compared to the Er-fiber seed due to the introduction of excess amplitude and phase noise at the nonlinear broadening stage. The resulting intensity noise and phase fluctuations are then further increased in the subsequent amplifier system.

The reported relative intensity noise (RIN) values of such systems operating in the 2 μm waveband are in the range 0.2 – 0.7%, depending on implementation details and noise frequency integration range, which is about an order of magnitude larger than the driving Er:fiber seed [10,60,184,186,187,189]. In case of a Thulium-Holmium (Tm/Ho) co-doped fiber amplifier seeded by a solitonic SC, a RIN value of 0.23% was reported, integrated over the narrow frequency range 1 kHz – 1 MHz, corresponding to an increase of the seed signal noise by a factor of 57 times [189]. Similar RIN values were reported for a Tm/Ho co-doped amplifier seeded with a Raman soliton signal (0.6%, 1 Hz to 10 MHz) [60], a SC-seeded hybrid Er/Tm fiber frequency comb source (0.7%, 1 Hz to 1 MHz) [186], and a frequency comb system operating in the 2 – 2.15 µm wavelength range seeded by Raman solitons (0.3%,1 Hz to 10 MHz) [187]. Recently, amplification of white noise during the nonlinear broadening of the Er-fiber seed system in the anomalous dispersion region of a highly nonlinear fiber has been identified as one of the major performance limitations for further evolution of high power frequency combs around the 2 µm wavelength, leading to 0.5% of integrated RIN (10 Hz – 30 MHz) at the amplifier output [10]. Direct amplification schemes of Tm-doped mode-locked fiber lasers using anomalous dispersion nonlinear dynamics for pulse shortening, such as nonlinear self-compression face similar noise challenges (e.g. 0.34% RIN in a frequency range from 10 Hz to 11 MHz in a recently reported 50 fs system) [190].

In this part of my work, I aimed to overcome these soliton-related limitations by completely eliminating the noise-sensitive anomalous dispersion nonlinear dynamics from the spectral broadening stage. I employed an all-normal dispersion photonic crystal fiber (ANDi PCF) for coherent SC generation [33,64], extensively studied in the previous chapters of this dissertation research. The fiber served to generate a broadband coherent seed signal for an all-PM Tm-doped fiber amplifier. In fact, many nonlinear noise amplifying effects, such as scalar modulation instability or the Raman effect, are effectively suppressed by the ANDi design and the associated nonlinear dynamics [65]. Normal dispersion nonlinear dynamics were recently reported to have a factor of 50 higher threshold for the onset of noise-driven decoherence compared to equivalent spectral broadening in the anomalous dispersion regime [65]. Besides, all-normal dispersion nonlinear processes also minimize the temporal jitter between different wavelength components [69] that can exhibit lower RIN than the pump laser [45,48] to produce flat, smooth, and stable spectra that can be compressed to high quality single-cycle pulses [67,68]. Hence, ANDi SC is ideally suited for the coherent seeding of ultra-low noise, broadband, ultrafast fiber amplifier systems. ANDi PCFs, compatible with pumping at the wavelength of around 1560 nm, offer the potential for pulse-preserving SC generation covering amplification bands of all the three major fiber amplifiers [51]. Coherent seeding of a Tm/Ho co-doped fiber amplifier system with this type of SC was recently demonstrated. The set up resulted in 66 fs pulses, centered at 1940 nm with

100 nm of 3 dB width and 70 kW of peak power and RIN of 0.07% (10 Hz - 20 MHz) [63]. However, this work has also revealed the additional problem that is PMI, which becomes the major performance limiting factor in ANDi SC seeded amplifiers, as it occurs both in normal and anomalous dispersion regimes. PMI leads to significant pulse-to-pulse fluctuations and coherence degradation of SC pulses specifically in weakly birefringent fibers, as reported in detail [38,41,191]. In the amplitude noise spectrum, the occurrence of PMI is associated with the generation of a significant white-noise component [39,63] However, PMI can be efficiently suppressed in highly birefringent, polarization-maintaining (PM) fibers, eliminating the last remaining noise amplification process in femtosecond pumped ANDi SC generation [39].

In this chapter, I demonstrate the combination of SC generation in a PM ANDi fiber and its amplification in a fully PM fiber system indeed eliminates all major sources of nonlinear noise amplification and enables ultra-low noise performance of ultrashort pulse amplifiers and frequency comb sources in the 2000 nm spectral region. This is evidenced with results of RIN measurements between the driving femtosecond Er:fiber laser front-end, the ANDi SC, and the Tm-doped fiber amplifier revealing virtually identical integrated RIN figures. Therefore, neither the SC generation nor the amplification process introduces significant excess noise. The integrated RIN of our system is an order of magnitude lower than previous reports employing anomalous dispersion nonlinear dynamics for seeding ultrafast fiber amplifiers at 2 µm.

Significant parts of the research, which I did in the scope of this chapter were published in a journal paper in Optics Express, in which I am the first and corresponding author [163]

5.1 Construction of 1565 nm fiber amplifier as a pump source for thulium amplifier

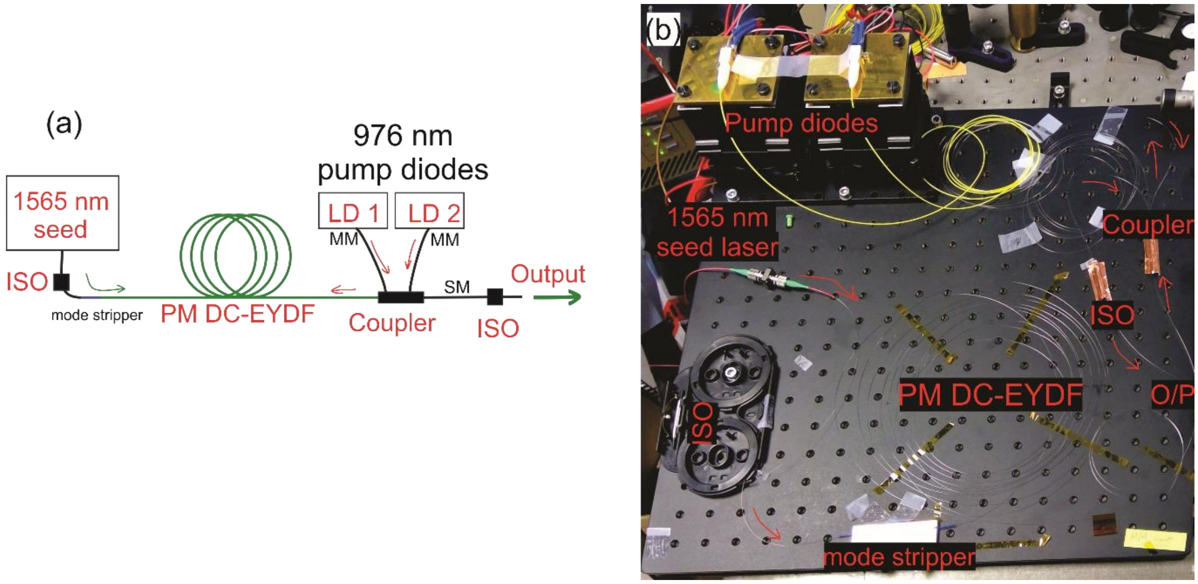

Figure 5.1. An in-house built PM 1565 nm fiber amplifier. (a) Schematic of the fiber amplifier. (b) A photograph of the fiber amplifier setup, which was built in the scope of this work. PM DC-EYDF: double clad erbium/ytterbium co-doped fiber; LD: laser diode; ISO: isolator.

For Tm fiber amplifier development, a pump source operating at the wavelength of 1565 nm is preferred due to overlap with Tm^{3+} ion absorption. During my PhD, I had to work on different configurations of building Tm fiber amplifier systems. Firstly, I built 1565 nm source using a PM double clad Er/Yb co-doped fiber (DC-EYDF) from CorActive (DCF-EY-6/128-PM, 6.25/128 µm core/cladding diameter, 0.2 NA, 60 dB/m core absorption at 1535 nm [192]) and commercially available components as shown in figure 5.1. The gain medium was about 5 m of PM DC-EYDF fiber. I used a relatively long piece of fiber to ensure full absorption of the pump power. Two multimode (MM) laser diodes, each emitting 10 W at 976 nm were used as a pump source. A (2+1) ×1 multimode Gooch Housego power combiner with active PM signal feed-through was used to connect MM pump and DCF active fiber. The two didoes had output coupling fibers with 105/125 µm core/cladding diameter and 0.22 NA spliced to the MM inputs of a pump power combiner. The PM DCF active fiber is spliced to the active fiber port of pump combiner and SM port is used as the output. The PM DC-EYDF amplifier is seeded by a 1565 nm CW laser diode (Fitel, 40 mW) with SM fiber pigtail, which is spliced to other end of the DC-EYDF fiber by employing mode stripper.

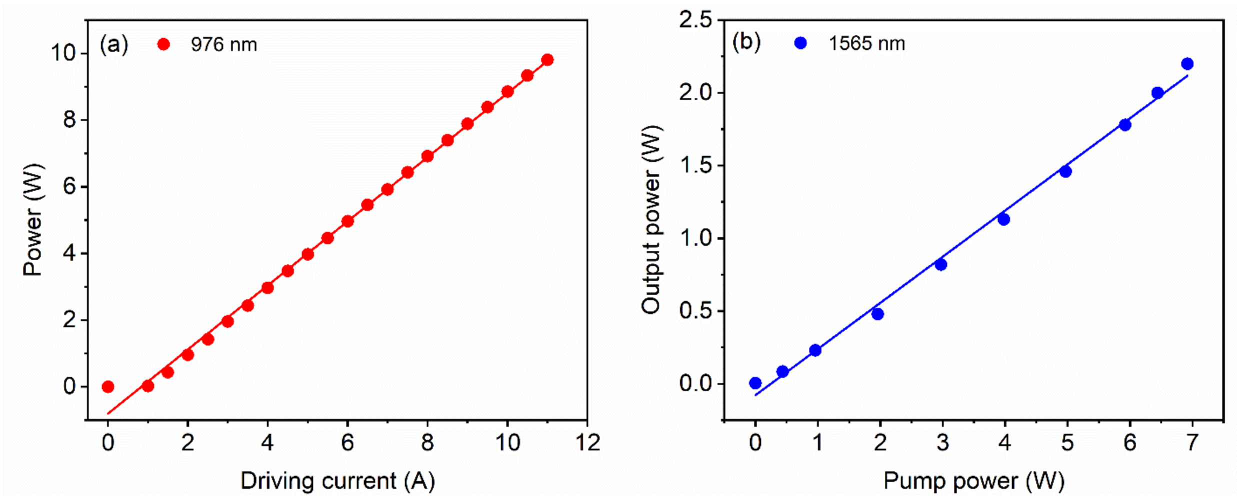

Figure 5.2. Power characteristics of 976 nm laser diode used to pump the in-house built 1565 nm amplifier. (a) Output power as a function of driving current of 976 nm laser diode (b) Output power of 1565 nm amplifier as a function of total launched pump power.

Figure 5.2 summarizes the output power characteristics of the 976 nm laser diode used to pump the in-house built 1565 nm fiber amplifier. Figure 5.2(a) plots the output power of the laser diode as a function of the driving current. The threshold current is ~1.4 A. The output power grows linearly with the driving current until about 9.7 W at 11 A (maximum current). Figure 5.2(b) plots the output power as a function of total launched pump power of 976 nm laser diode. During the experiments, only one of the laser diodes with the maximum launched power of 7 W, was used. The corresponding CW amplifier maximum output power, fed to the ultrafast Tm-fiber amplifier was 2.2 W. The output power of the 1565 nm amplifier increases linearly with the pump power with a slope efficiency of 31.7 %. Figure 5.3 depicts the output spectra of the 1565 nm in-house built fiber amplifiers at the different drive current levels. The output wavelength of the amplifier practically does not change with increasing current of the pump laser diode.

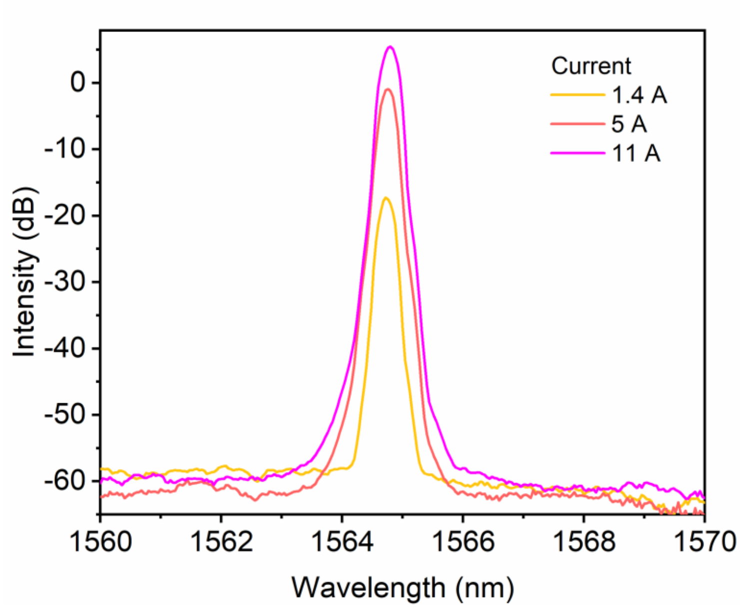

Figure 5.3. Spectral characteristics of in-house built 1565 nm fiber amplifier at different driving current levels. OSA resolution was 0.2 nm.

5.2 Experimental setup of coherently seeded, ultrafast thulium fiber amplifier

I employ the fiber chirped pulse amplification (FCPA) scheme as illustrated in figure 5.4. The experimental setup consists of a spectral broadening stage based on ANDi SC generation followed by a dispersive pulse stretching and Tm doped fiber amplifier stage, and finally a fiberized pulse compression stage.

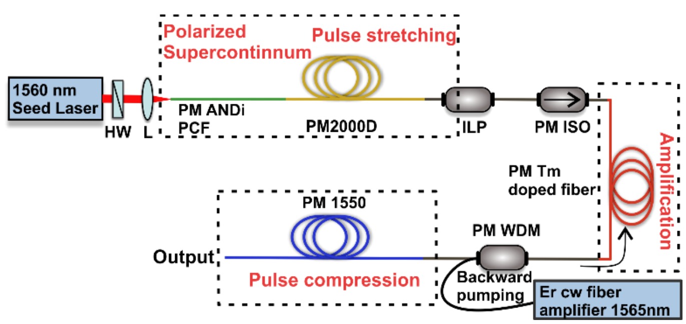

Figure 5.4. Experimental setup of the coherently seeded ultrafast all-PM thulium fiber amplifier. HW – half-wave plate, L - aspheric lens, PM ANDi PCF - polarization maintaining all normal dispersion photonic crystal fiber, ILP - inline polarizer, PM ISO - polarization maintaining isolator, PM WDM - polarization maintaining wavelength division multiplexer, Er CW– Erbium-doped continuous wave fiber amplifier.

At the front end, there is a 15 cm long PM ANDi PCF NL46. Its dispersion and group birefringence were discussed in detail in chapter 3. The GDD curves are shown in figure 5.5. In chapter 4, I discussed SC generation and spectro-temporal characterization. The PM ANDi PCF was pumped by a commercial Er:fiber-based laser (Menlo Systems) operating at a central wavelength of 1560 nm with a 100 MHz repetition rate, delivering 80 fs long, 3.5 nJ Gaussian pulses. The pulse energy coupled into the PM PCF is estimated to be 2 nJ.

A half-wave plate at the input and a polarizer at the output of the PCF was used to differentiate between the polarization components of the fundamental mode at the output of PCF in order to match the polarization to that of the active fiber of the amplifier. The PM PCF generates spectrally broad (1100 - 2150 nm) and coherent SC with 40 mW of average output power. I fixed the position of the half-wave plate to the axis with the broadest available spectrum. The SC is linearly polarized with around 10 dB of polarization extinction ratio. The SC spectrogram recorded using XFROG is shown in figure 4.5.

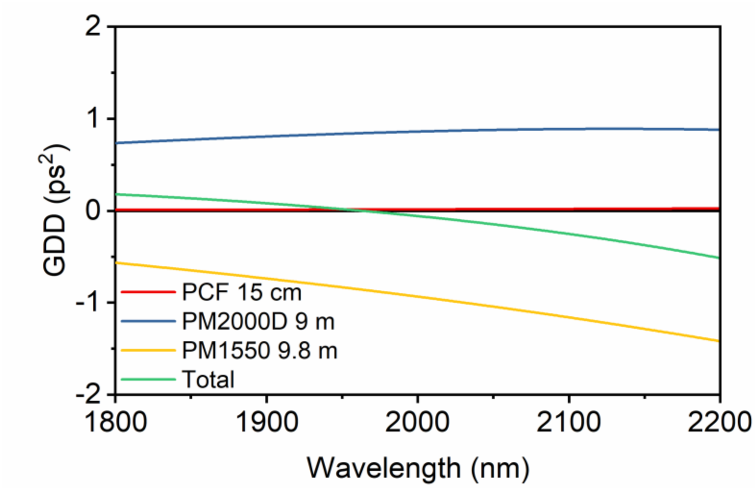

Figure 5.5: Measured group delay dispersion of PM ANDi PCF, PM2000D, and standard PM1500 fiber and total left-over dispersion in the setup.

In the following experiment, the polarizer at the output of the PM ANDi PCF was removed and butt-coupled to 9 m long polarization maintaining PM2000D fiber (Coherent Nufern) in order to further temporally stretch the seed pulse before amplification, which has normal dispersion in Tm amplification window. Hence this fiber helps to compensate for the anomalous dispersion of active and passive fibers in the subsequent amplifier section. The measured GDD curve of this fiber is shown in the figure 5.5 and compared to the GDD of the standard PM1550 used as pigtail fiber for the passive components in the amplifier. Due to the mismatch of core diameters and thermal expansion coefficients between the PCF and PM2000D fibers, standard fusion splicing was not implemented here. Instead, I placed the PM2000D fiber on a rotation mount to match its polarization axis with the PM ANDi PCF axis. PM2000D can also act as an efficient mode field adapter between PM ANDi PCF and PM1550 fiber (including end of standard components). As the small core of PM2000D with high NA efficiently collects the light exiting the PCF, the expansion of core under fusion splicing can be used to minimize splice loss to PM1550 to < 0.2 dB. This allows seeding the amplifier with approximately 2 mW of average power contained in the relevant spectral range of 1750-2200 nm of the SC pulse. All the remaining fibers in the setup were fusion spliced with a standard PM fiber compatible splicer (Ericsson FSU-995). I point out that cold splicing of the silicate glass ANDi PCF used here to a silica single-mode fiber is generally possible by moving the splicing arc away from the PCF to heat up the silica fiber only. This, however, limits the seed signal average power due to a lossy splice and was not implemented in this work.

An in-line fiber polarizer (ILP) was used to remove any remaining depolarized components before the seed was forwarded to the Tm-doped fiber. The amplification stage consisted of a 8 m long section of PM single-mode Tm-doped silica fiber (Coherent Nufern PM-TSF-9/125, 9 μm core diameter, 0.15 NA, 9 dB/m core absorption at 1180 nm and 27 dB/m core absorption at 793 nm [193]), emission and absorption cross section is as shown in figure 5.6. The absorption and emission peaks are at 1665 nm and 1835 nm respectively. The amplification stage is operated in backward core pumping by a continuous-wave (CW) signal. The pump signal was delivered through a PM wavelength division multiplexer (PM WDM) by an in-house built CW EYDF fiber amplifier as described in section 5.1. GDD of the standard single-mode PM1550 fiber and PM2000D fiber is shown in figure 5.5. Tm-doped PM-TSF-9/125 fiber's GVD is assumed as that of PM1550 fiber, having a negative slope of around -0.15 to -0.01 ps^2/m in the range 1420–2000 nm.

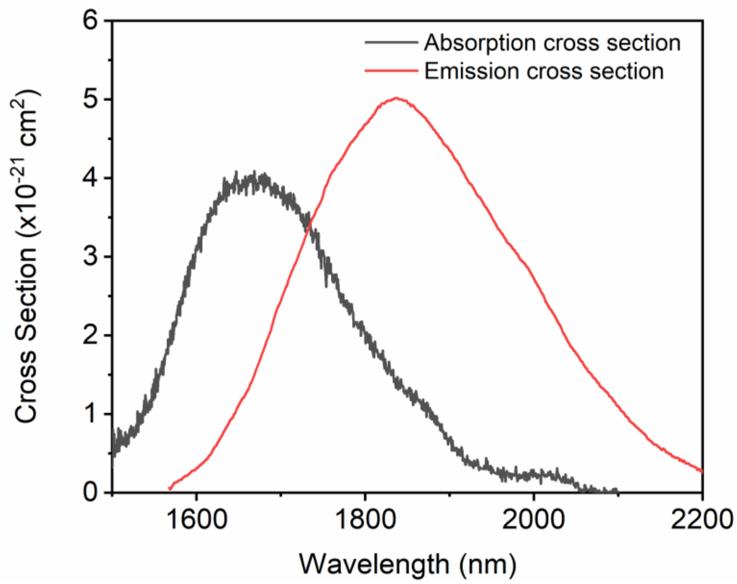

Figure 5.6: Absorption and emission spectra of the Nufern Tm-doped silica fiber [194]

A polarization maintaining isolator (PM ISO) was used to ensure the unidirectional operation of the amplifier. Since these commercial fiber components were available in the "fast axis blocked" variant as standard, the developed system was designed to operate in the slow axis. The PM architecture of the setup did not require any polarization controllers. Further, the pulses temporally compress during propagation in the amplifier due to the anomalous dispersion of the active and passive fibers (ie. the WDM pigtails), but it remains positively chirped at the exit of the amplifier due to pre-chirping over the section of PM2000D fiber between the nonlinear PCF and the Tm-doped fiber. The final temporal recompression was simply achieved by splicing an appropriate length (about 1 m) of the PM1550 fiber to the amplifier. In figure 5.5, the 9.8 m fiber length of PM1550 is a total length from Tm-doped fiber, passive fiber at the end, and from the commercial components. The amplifier output and pulse compression were monitored with an OSA and an in-house built second harmonic generation frequency-resolved optical gating (SHG-FROG) setup respectively. Additionally, I measured the relative intensity noise of PM Tm amplifier and the SC seed pump laser using a 12.5 GHz, 2 µm InGaAs photodiode and an RF spectrum analyzer (Agilent E4443A) employing the standard procedures outlined in the literature [195].

5.3 Results and discussions

I started by measuring the amplified pulse spectrum at the output of the Tm amplifier. Figure 5.7(a) shows the output spectra measured for different driving currents of the pump laser diode in the

CW Er-fiber amplifier, which used as pump source for the ultrafast Tm fiber amplifier. The corresponding driving current versus pump power is displayed in figure 5.2. I observed the shaping of the output spectrum at the Tm amplifier with increasing the pump power. The output power of the Tm amplifier increased linearly with the pump power with a slope efficiency of 27.3 % as shown in figure 5.7(b).

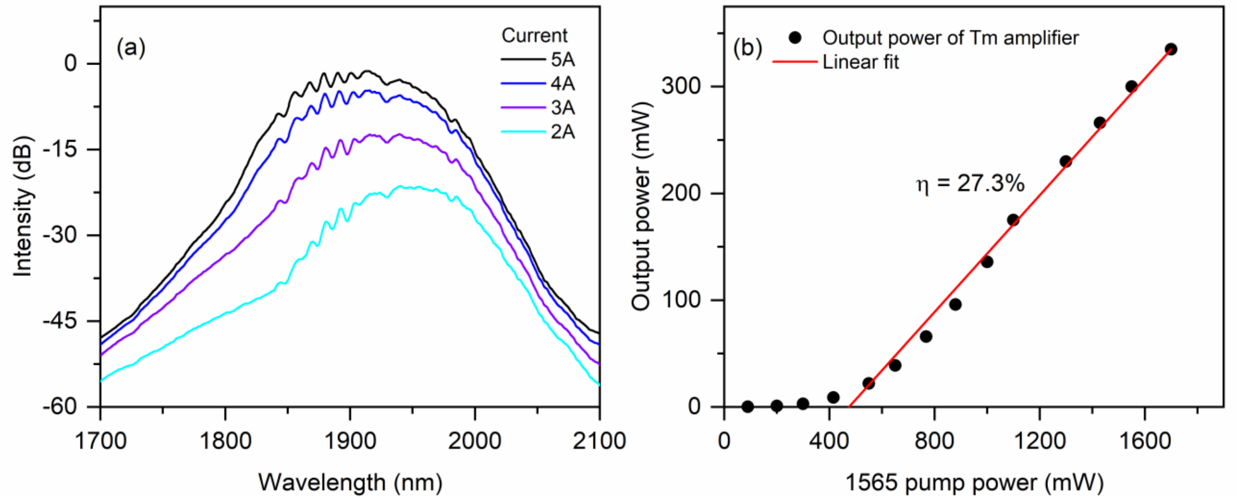

Figure 5.7. Spectral and output power characteristics of the Thulium amplifier. (a) Output spectra measured for different driving currents. (b) Output power of the Thulium amplifier as a function of total launched pump power at 1565 nm.

Figure 5.8(a) shows the spectrum measured at the output of the amplifier at different conditions. The yellow line spectrum shows the unabsorbed seed at the output when compared to full SC seed in figure 5.8(b). It also represents the Tm fiber absorption region. The blue line represents the amplified signal with SC seed and red spectrum without the SC seed, which is amplified spontaneous emission (ASE). Hence, the pulse spectrum at the amplifier output is shaped majorly by the SC seed and Tm-doped fiber gain profile, but also by the filtering effect of the PM WDM. Figure 5.8(b) shows the long wavelength part of the SC seed signal (black), the amplified spectrum at the output of the Tm fiber amplifier (dark blue), and signal (light blue) measured in the opposite axis. At the amplifier output, I obtained 350 mW of average output power with 84 nm of 3 dB spectral width, centered at 1880 nm, and 16 dB polarization extinction.

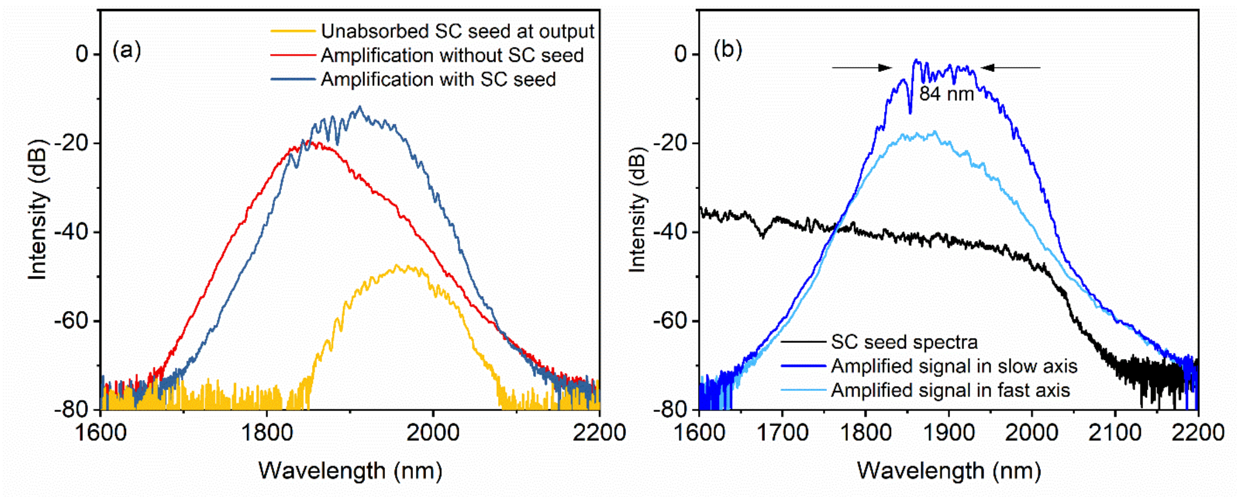

Figure 5.8. (a) Output spectra before and after amplification, along with and without seed signal. (b) Output spectra of the Thulium amplifier: the seed pulse spectrum, the amplified signal in slow axis (dark blue trace), the fast axis spectrum (light blue trace) demonstrates polarization extinction.

In the following steps, I purposefully did not drive the amplifier to high output powers and focused on the feasibility of all-fiber compensation of the output pulse chirp and the noise performance of the system. It is important to note that the octave spanning SC seed is first stretched to 286 ps along the 9 m long, positive GVD PM2000D fiber to avoid the nonlinearities and to avoid the switch of chirp sign during amplification.

Figure 5.9 shows the SHG-FROG traces retrieved using an algorithm based on generalized projections [135]. At the output of the amplifier before recompression, the retrieved pulse duration was 3.6 ps as shown in figure 5.9(a). Figure 5.9(b) shows the FROG trace measured at the end of 2 m of PM1550 fiber spliced to the output of the amplifier for pulse compression. I obtained 1.7 ps retrieved pulse duration with a flip in symmetry, indicating that dispersion was over-compensated due to excessive length of the PM1550 compensating fiber at the amplifier output. FROG traces in Figure 5.9(a) and 5.9(b) show the characteristic flip in the symmetry, which helps to distinguish the cross over point during compression. From this point, I used the cut-back method to compensate for the GVD and monitored the output group delay profile for each cut length to find the optimum PM1550 fiber length corresponding to the best compression point.

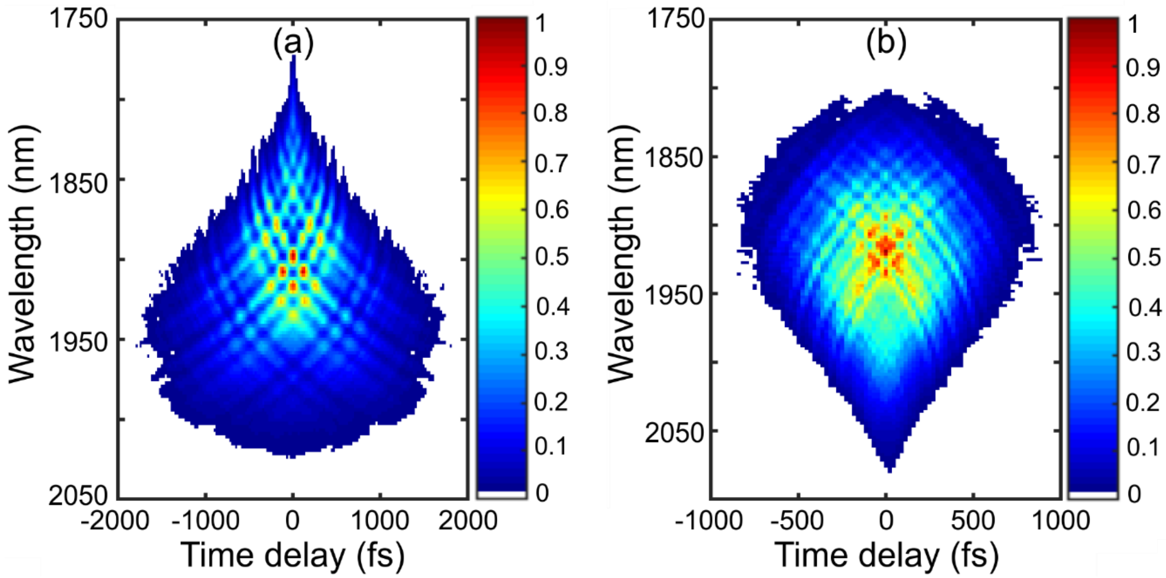

Figure 5.9. Retrieved output pulse spectrograms (a) at the output of the Tm fiber before recompression (b) after 2 m of additional PM1550 fiber.

Figures 5.10(a) and 5.10(b) show the measured and retrieved FROG traces for the optimal length of the PM1550 fiber used to recompress the output pulse. Wavelength scale is converted back to the original from the SHG wavelength. The FROG retrieval error was $5.4\text{x}10^{-3}$ over a 512 × 512 grid size. There was only a small mismatch between the FROG-reconstructed spectrum and experimental spectrum measured with OSA, as shown in figure 5.10(c) is assigned to spectrometer calibration. The fine structure observed in the spectrum of the compressed pulse at the system output is likely due to a birefringent filtering effect, caused by a slight misalignment of the fiber polarization axis before a polarization sensitive element. I verified that the amplifier output signal is mechanically robust in a sense, that manual disturbing (e.g. bending) the spliced fibers does not affect its operation. The color map of the FROG trace revealed that more than 60% of the total energy was concentrated in the main part of the pulse. The pulse duration was 96 fs (blue curve) considering the Gaussian pulse shape, as shown in figure 5.10(d). The calculated transform-limited pulse length is 69 fs (black curve). The compressed pulse has a time-bandwidth product (TBP) of 0.697, which is 1.6 times larger than the transform-limited pulse. This is due to the accumulation of significant third-order dispersion (TOD) over the length of the all-fiber system, as the simultaneous compensation of GVD and TOD using only optical fibers is not possible. Moreover, the small mode field diameter of the PM1550 fiber used as a compressor distorts the pulse at high pulse energies due to nonlinear effects. Large mode area (LMA) fibers or external compression using bulk optics, such as gratings or chirped mirror pairs, could be used for pulse compression even at high pulse energies.

The amplified pulse at the end of the Tm-doped fiber is recompressed to 96 ± 0.56 fs with an average output power of 350 mW and pulse energy of 3.5 nJ, which corresponds to a peak power of approximately 36.2 kW considering Gaussian pulse shape.

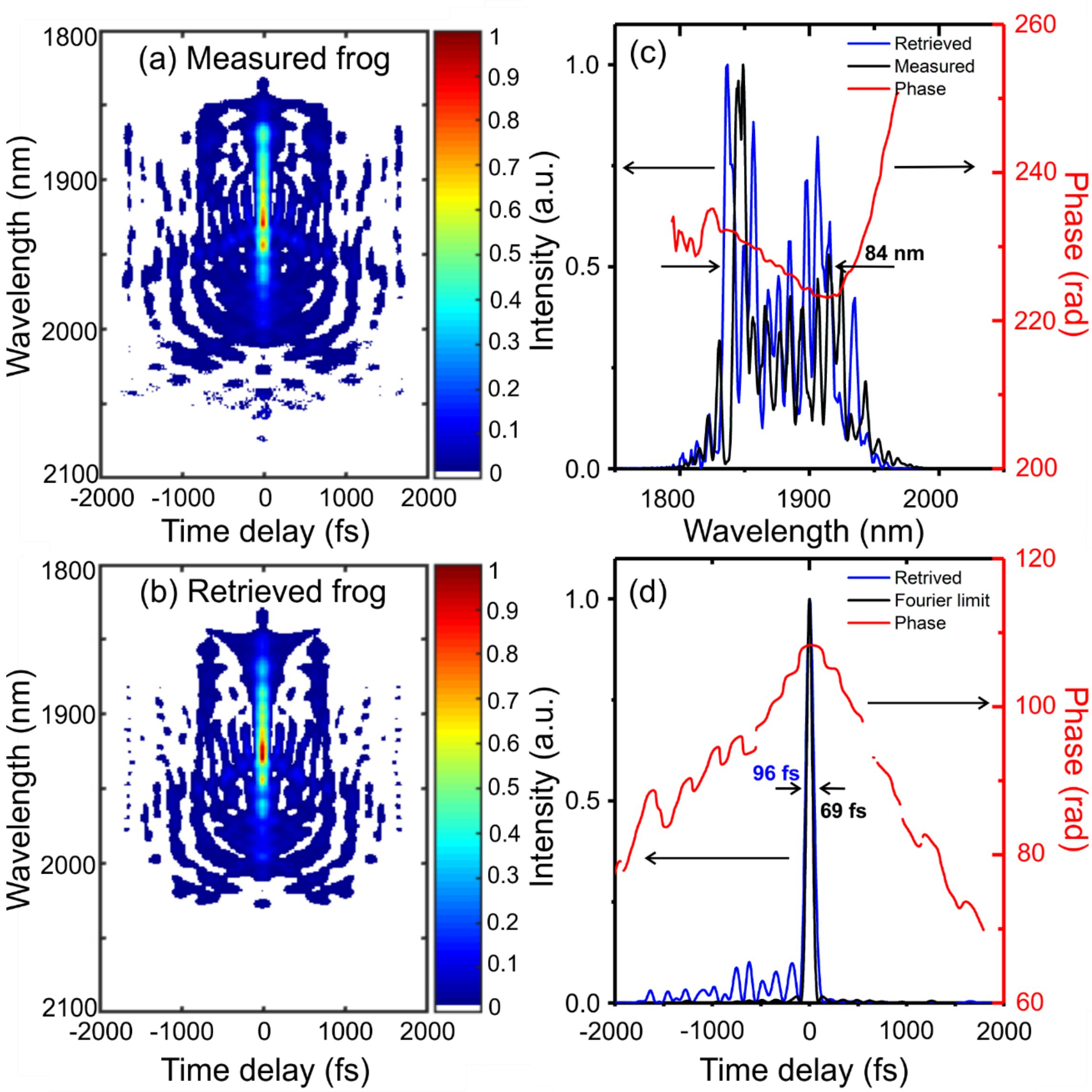

Figure 5.10. Characterization of the compressed pulse at the output of the PM1550 fiber using SHG FROG. (a) Measured FROG trace, (b) Retrieved FROG trace, (c) FROG-retrieved spectrum (blue) compared to spectrum independently measured with an OSA (black) and phase profile (red), (d) FROG-retrieved pulse shape (blue) compared to the Fourier limit (black) and phase profile (red).

Finally, I performed noise characterization of the developed amplification system. RIN measurements were performed using a 12.5 GHz InGaAs broadband fiber coupled photodiode (PD) sensitive over the entire spectral bandwidth of interest (responsivity larger than 0.8 A/W in the wavelength range from 1400 nm to 2100 nm, ET-5000F from Electro-Optics Technology). Agilent E4443A electronic spectrum analyzer (ESA) was used to record the Radio Frequency (RF) spectrum. The light from the amplifier system was first coupled to SM fiber patch cord to measure power before coupling to PD fiber input. In order to assure linear operation of the PD, the power incident on the PD's pigtail input facet was maintained around 1 mW and the DC photocurrent was monitored at the output of photodiode using a digital multimeter. The DC power is obtained using the formula $P_{DC} = (I_{DC})^2 \cdot R_L$, where I_{DC} stands for the DC current, and R_L is the load resistance of the ESA. Figure 5.11 shows the measured intensity noise of the Er: fiber seed laser, the SC, and the Tm-doped fiber amplifier. The relative intensity shot noise level of the PD was calculated for the seed laser and for the Tm amplifier as using the formula P_{shot}/P_{DC}, where P_{shot} is shot noise power $2qI_{DC}R_L$, and q is the elementary charge. Therefore, the RIN (shot) is determined by $2q/I_{DC}$. In my measurements, the shot noise limit was equal to -154.13 dB/Hz, -153.85 dB/Hz, and -154.08 dB/Hz for the Tm amplifier, ANDi SC, and the Er: fiber seed laser, respectively. The RIN (shot) levels are slightly different due to different I_{DC} values for the amplifier, SC, and the seed laser.

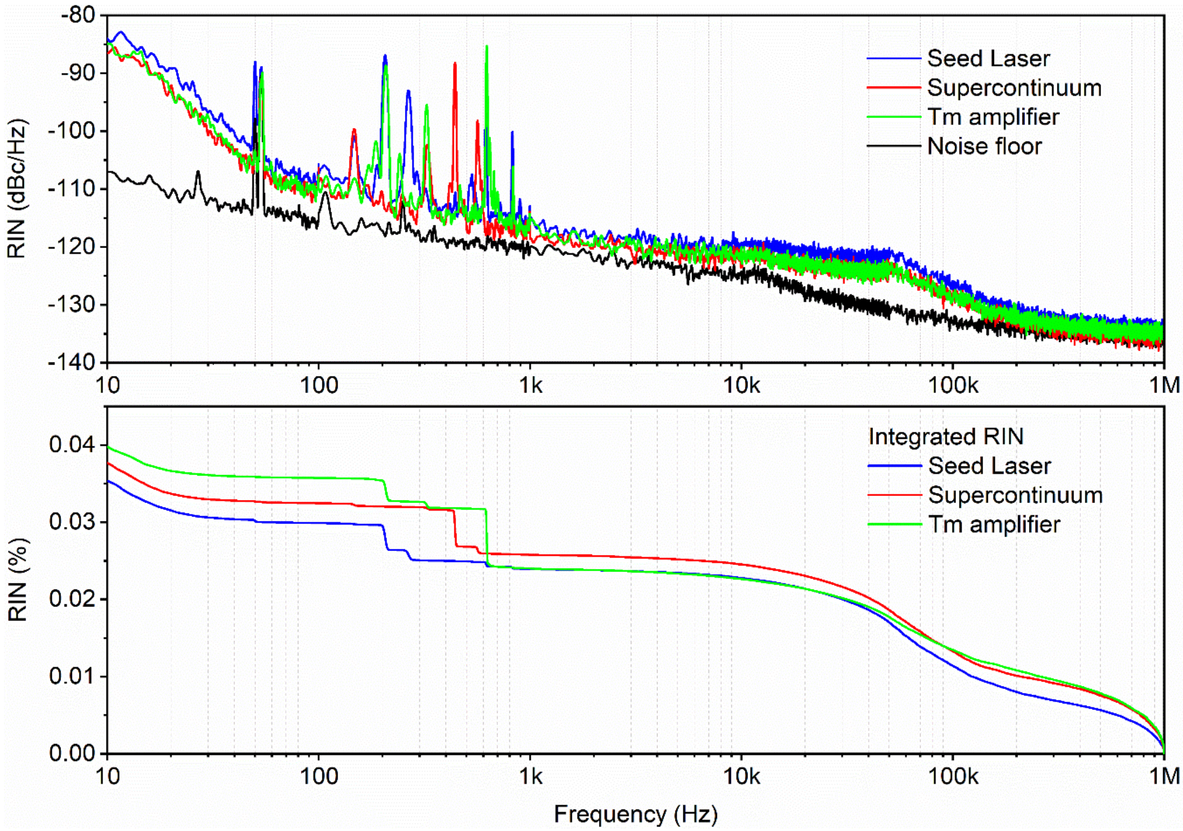

Figure 5.11. Amplitude noise measurements at different positions along with the amplifier. The top shows the spectrally resolved amplitude noise in a range 10 Hz - 1 MHz, while the bottom shows the total integrated RIN in percent. Shown are the noise of the Er-fiber seed laser before spectral broadening (blue), the spectrally broadened supercontinuum seed after the ANDi PCF (red), and the amplified and compressed output of the Tm amplifier (green). The noise floor of the measurement system is shown in black (top plot).

Results of the RIN measurements are shown in figure 5.11. The sensitivity limit given by the noise floor of the photodiode is indicated by the black trace in the top plot of figure 5.11. Remarkably, the RIN levels of both the ANDi SC and the amplifier are very close to the RIN level of the Er: fiber seed laser. Apart from some additional low-frequency noise peaks < 1 kHz which are attributed to mechanical vibrations at the free-space optics at the PCF coupling port and to the pump diode noise from the CW amplifier (used to pump the Tm-doped fiber amplifier). These results confirm that neither the nonlinear spectral broadening nor the subsequent amplification process introduce significant excess noise. Most importantly, I do not observe any signatures of noise-amplifying nonlinear effects such as scalar or polarization MI, which have been linked in previous reports to the occurrence of white-noise high-frequency components in the amplitude noise spectrum [10,39,63,66].

The integrated RIN is calculated from 10 Hz to 1 MHz and represented in the bottom plot of figure 5.11. For the Er: fiber seed laser, the RIN is 0.035%, while for the ANDi SC it is 0.037% and for the Tm-doped fiber amplifier it is 0.04%. This corresponds to less than 20% excess noise introduced by the nonlinear broadening stage and by the ultrafast thulium amplifier combined. Notably, the integrated RIN at the output of the amplifier developed in this work is in the order of one magnitude lower than the previous results using anomalous dispersion nonlinear dynamics for a spectral broadening of the Er: fiber seed laser [10,60,184,186,187,189].

5.4 Conclusions

To the best of my knowledge, the low amplifier RIN of 0.04% (10 Hz - 1 MHz) and the small noise amplification factor of 1.1 represent the lowest values reported for wideband ultrafast amplifiers operating at 2 μm to date. The amplifier system developed and characterized in the scope of this work is designed in such a way that many of the traditional linear and nonlinear noise amplifying effects are effectively suppressed. The successful amplification and recompression of all-normal dispersion SC pulses provide experimental evidence for the feasibility of ultra-low noise, coherent seeding of ultrafast fiber amplifiers operating at pulse duration below 100 fs in the 2 μm wavelength window. While I did not reach the Fourier transform limit in the current implementation due to the unavailability of fibers allowing simultaneous higher-order dispersion compensation, this could still be worked around at a power amplifier stage with an external compressor. Compared to earlier realizations of ultrafast seeding of fiber amplifiers using anomalous dispersion nonlinear dynamics, the major advance of our system is the elimination of noise amplifying nonlinear effects from the spectral broadening and amplification stages.

The polarization maintaining design of both the nonlinear fiber and amplifier makes the system immune against PMI instabilities, which have recently been identified as major performance limitation in non-polarization-maintaining systems, even when seeded by ANDi SC sources [63]. The exclusion of all decoherence-driving nonlinear effects finds reflection in the RIN measurement results obtained here, which revealed a factor of 10 improvement over systems using anomalous dispersion nonlinear dynamics for seed signal generation [10,60,184,186,187,189].

Noise amplification in our system is limited to only 20%, which is mainly caused by low-frequency noise originating from the pump diodes. Conveniently, these results add up with the improved threshold for transverse mode-instability in Tm-doped ultrafast fiber amplifiers, as compared to Yb-doped systems [196]. The developed amplifier follows an all-polarization maintaining design, including the nonlinear fiber for the generation of coherent SC for the seed signal. Low noise characteristic to this type of SC, combined with a determined state of polarization across the entire setup, contributed to the excellent noise properties of the amplifier, which practically replicated those of the seed femtosecond laser at the front-end of the system. The amplifiers' robustness and environmental stability stemming from the all-PM fiber configuration make it a promising platform for further power scaling and, for example, pulse synthesis using a tandem of simultaneously seeded Er-doped and Tm-doped fiber amplifiers – which in particular is the scope of the following chapter of this dissertation.

Chapter 6. Coherent seeding of all PM Erbium and Thulium amplifier

In this part of work, a new frontier in ultrafast femtosecond fiber-based amplifier systems is explored by broadband seeding of multiple rare-earth doped optical fiber amplifiers in various amplification schemes. Initially, this has been realized in an OPCPA system seeded with a pulse-preserving SC, which enabled CEP stable near single-cycle pulses at energy levels compatible with attosecond technology [165]. Several works has been carried out by seeding Tm-doped fiber amplifiers with solitonic seed signals [59,60,62,82], while ANDi SC pumped by femtosecond Er-doped systems has been reported in the scope of this work [63,163]. Combining the output of Yb and Er amplifiers can be successfully applied to the generation of ultrashort pulses and frequency combs in the mid-infrared light via nonlinear frequency conversion in an external nonlinear crystal [10,83,186,187,189,197]. In combination with a dispersive wave generated at around 1030 nm and soliton at 1900 nm, it opens a route to optical-fiber based single-cycle pulse generation by simultaneous seeding of Yb^{3+} and Tm^{3+} doped amplifiers [198].

In chapter 5, I successfully demonstrated the ultra-low noise, all PM ultrafast Tm-dopedall-fiber chirped-pulse amplifier, seeded by a polarized ANDi SC and driven by an ultrafast Er-fiber laser [163]. The system comprised only PM fibers and delivered 96 fs pulses with 350 mW output average power, with a 100 MHz repetition rate, centered at a wavelength of 1880 nm. Additionally, the RIN was an order of magnitude lower than similar systems previously seeded with Raman solitons. This highlighted the superior noise properties of ANDi SC and their potential as ultra-low noise seed sources for broadband, high power ultrafast fiber amplifiers, and frequency combs.

This additionally induced the interest in amplification of the 1550 nm band, which can be easily achieved by seeding an Er doped fiber amplifier using the same SC seed. The PM ANDi SC seed used in chapter 5 was weakly polarized and had only ~ 40 mW of average output power. Higher SC seed power is required to seed both Er and Tm amplifier systems simultaneously, which I intend to accomplish here using highly birefringent tellurite ANDi PM PCF. This PCF offers improved PER and average power in SC generation in the required spectral range for coherent seeding of the Tm and Er amplifiers, compared to the squeezed lattice PCF used in the previous chapter.

In this chapter, I demonstrate that broadband PM ANDi SC source can be used as a seed to both Tm-doped and Er-doped fiber amplifiers. In particular, the results obtained in the scope of this part of work reveal, how the combination of improved SC seed output power and PER with the all-PM fiber architecture further progressed the output power characteristics and noise performance of the Tm-doped amplifier. Improved average output power of the SC enabled simultaneous seeding the Er-doped amplifier, as well. The rationale behind this is overcoming the power drop at the WDM component dividing the seed signal between the Er-doped and Tm-doped amplifier arms, as will be discussed in detail in the following section of this chapter. Detailed RIN measurements are performed at different positions along with the amplifier system, and at various pump power levels. In the final section, sum-frequency generation signal (SFG) between Er and Tm amplifiers was obtained by using a $\chi^{(2)}$ nonlinear crystal and its RIN is measured and discussed.

6.1 Experimental setup

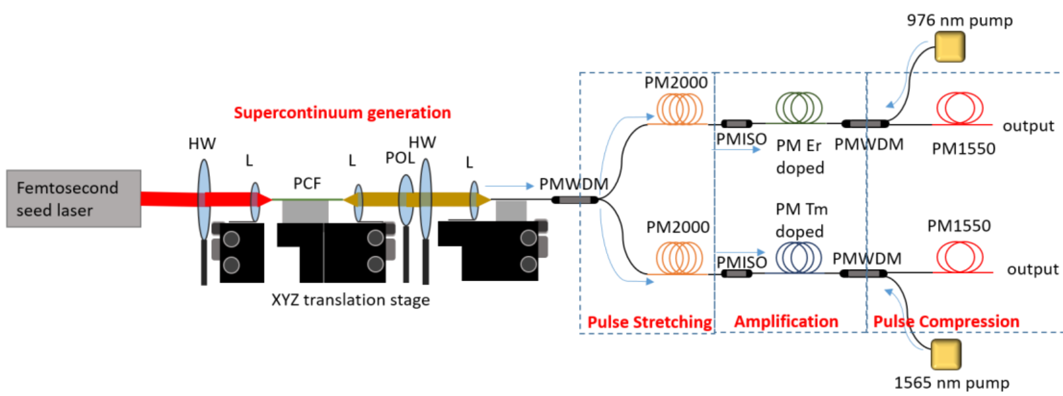

Figure 6.1 Experimental setup of the coherently seeded ultrafast all-PM Erbium and Thulium-doped amplifier system, PCF-Photonic crystal fiber, L- aspheric lens, HW- halfwave plate, POL- polarizer, PMISO- - polarization maintaining isolator, PMWDM- - polarization maintaining wavelength division multiplexer.

The experimental setup is illustrated in figure 6.1. Similar to the previous chapter, I employed the FCPA configuration here. The setup can be divided into 4 stages: SC seed signal generation, PMWDM seed signal splitting between the two amplifier arms, seed pulse stretching, amplification, and pulse compression.

In the first stage for SC generation, a 5.5 cm long PM ANDi PCF was used, and this fiber was selected specifically for broadband seeding of ultrafast Er and Tm fiber amplifiers. The non PM tellurite glass PCF fiber design, fabrication technology, and geometrical characteristics were investigated in earlier work [199], including detailed measurement results of dispersion. Here I employed the PM variant of the tellurite glass PCF and the fiber was designed as described previously [199]. An SEM image of this PCF is shown in figure 6.2.(a). This PCF enables the generation of a broadband SC when pumped by a commercial Er:fiber-based laser (Menlo Systems) operating at a central wavelength of 1560 nm with a 100 MHz repetition rate, delivering an 80 fs long, 3.5 nJ Gaussian pulses. The femtosecond laser light was coupled into the PCF through an aspheric lens (Thorlabs) with a focal length of 4 mm and an anti-reflection coating compatible with the pump laser spectrum. The PCF was mounted on a 3-axis translation stage for precise control of the input condition. A similar, uncoated aspheric out-coupling lens was used to collimate the light out of the PCF. The use of uncoated lens was motivated with avoiding of spectral distortion of the broad spectrum of the SC pulses seeded into the amplifiers. The front-end laser pulse energy coupled into the PM PCF is estimated around 2 nJ, based on the driving femtosecond laser output pulse energy of 3.5 nJ and roughly 60% of coupling efficiency. A half-wave plate at the input and a polarizer at the output of the PCF was used to differentiate between the polarization components of the fundamental mode at the output of the PCF, in order to match the polarization to the next stage - the PMWDM component splitting the seed signal’s respective spectral parts into both amplifier arms, as shown in figure 6.1. Even though the nonlinear dynamics are effectively concluded within the first few millimeters of the PCF (the optical wave-breaking length is about 4 mm), the length of the PCF was chosen to increase the convenience of handling. Use of a system of translation stages and bulk optics to couple the light in and out of the PCF was necessitated by tellurite glass’s incompatibility of softening temperature and thermal expansion coefficient to that of silica glass. Polarization of the seed signal at the output of the PCF was controlled with a half-wave plate (HW in figure 6.1).

In the second stage, I coupled the collimated SC light into a PMWDM using a broadband achromatic lens with a 10 mm focal length. The PMWDM performed well as a bandpass filter by selecting an appropriate range of wavelengths from a broadband SC for Er and Tm amplifier stages. Next, a section of PM2000D fiber (Coherent Nufern; core diameter 2.4 µm, 0.41 NA) was used in order to further temporally stretch the seed pulse before amplification. The dispersion of the fiber was measured, and the results were discussed in chapter 3. Different lengths of the PM2000D were used in the case of the Er and Tm amplifier sections, depending on the dispersion compensation necessity, which will be discussed later. Except for PCF, all the remaining fibers in the setup were fusion spliced with a standard PM fiber compatible splicer (Ericsson FSU-995). In the case of PM2000D, due to its small core and high NA, I used a higher arc time (15 sec) for splicing with commercial PM1550 fiber, in order to match the mode field diameter between. A PM ISO was used to ensure the unidirectional operation of the amplifier. Since these commercial fiber components were available in the "fast axis blocked" variant as standard ones, the developed system operates in the slow axis.

The function realized in the third stage is amplification. A 5.55 m long PM single-mode Tm-doped fiber PM-TSF-9/125 from Coherent Nufern was used in the Tm-doped fiber amplifier arm. This fiber had a birefringence of 2.5×10^{-4} [193]. In the Er-doped fiber amplifier, I used a 1.2 m long, PM single-mode Er-doped fiber IXF-EDF-HD-PM from iXBLUE, with birefringence of 2.7×10^{-4} [200]. Both amplifiers were operated in the backward core-pumped configuration. The Tm-doped fiber was pumped through a PM WDM by an in-house built CW EYDF amplifier operated typically at 2 W of continuous-wave output power at a wavelength of 1565 nm as discussed in chapter 5. The Er-doped fiber amplifier was pumped through a PM WDM by a commercial diode laser at 976 nm from Thorlabs operated at 900 mW of maximum output power. The length of the amplification fibers was optimized for maximum pump power available for the respective fiber amplifier sections.

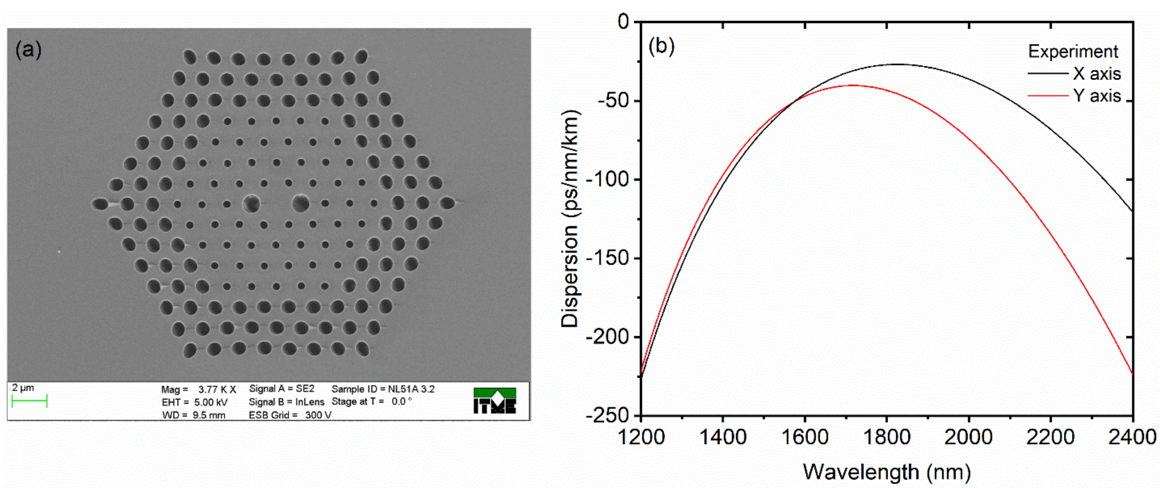

Figure 6.2. (a) Scanning electron microscopy image of the fiber structure. (b) Measured chromatic dispersion along both axes of the telluride PM ANDi PCF.

In the final stage, I used PM1550 fiber for pulse compression in both Er and Tm amplifier sections. The amplifier output and pulse compression were monitored with an OSA and an in-house built SHG-FROG setup, respectively. The SHG-FROG traces were retrieved using an algorithm based on generalized projections [135]. I measured the RIN at the different stages of the amplifier using an InGaAs photodiode with 12.5 GHz bandwidth and 2000 nm sensitivity and an RF spectrum analyzer (Agilent E4443A) by employing the standard procedures as described previously [195]. Additionally, I combined the Er amplifier and Tm amplifier compressed output signals in the XFROG setup and generated the respective SFG signal, for which the RIN was measured and discussed, as well.

6.2 Results and discussions

6.2.1 First stage: Supercontinuum generation

I begin with the description of the ANDi PCF used for polarized seed signal generation. An SEM image of the tellurite PM ANDi PCF is shown in figure 6.2(a) and the measured chromatic dispersion along both axes in figure 6.2(b). Here, birefringence was induced by introducing two larger air holes next to the solid core. The dispersion profile is all-normal in the measured range from 1200 nm to 2400 nm with dispersion maximum of -26.7 ps/nm/km around a wavelength of 1825 nm in the X-axis and -41 ps/nm/km around a wavelength of 1675 nm in Y-axis. The dispersion at the two principal axes takes very similar values in the range from 1200 nm to 1600 nm and thereafter both profiles diverge significantly. Since the Y-axis dispersion profile is steeper at the wavelengths redshifted from 1560 nm (the intended seed signal pump wavelength) it can be anticipated, that aligning the pump laser polarization with the X-axis would return broader supercontinuum spectrum, than intentionally exciting the Y-axis polarization mode component.

Next, I move to analyze the SC spectral broadening under pumping at a wavelength of 1560 nm in a 5.5 cm long sample of fiber as described in the experimental setup. As shown in figure 6.3, the measured spectra generated under femtosecond pumping enabled a broadening of spectrum covering wavelengths from 1100 nm up to 2280 nm in the X-axis and up to 2140 nm in the Y-axis. The broadening process is dominated by SPM and OWB, which also preserves the temporal integrity of the SC pulse. I confirmed that coupling the pump light to the X-axis produces the broadest spectrum compared to light coupled to the Y-axis, which is in line with the earlier prediction based on the dispersion profiles measured for each of the principal axes of the PCF. The reduced spectral broadening is the Y-axis is attributed to much steeper and stronger normal chromatic dispersion at wavelengths corresponding to the red-shifted edge of SC. The PER is greater than 20 dB in most of the spectral range in both the axes, except the pump wavelength region around 1560 nm, where it drops to 5 dB. This is due to the excitation of cladding modes in the pump region which reduces the PER.

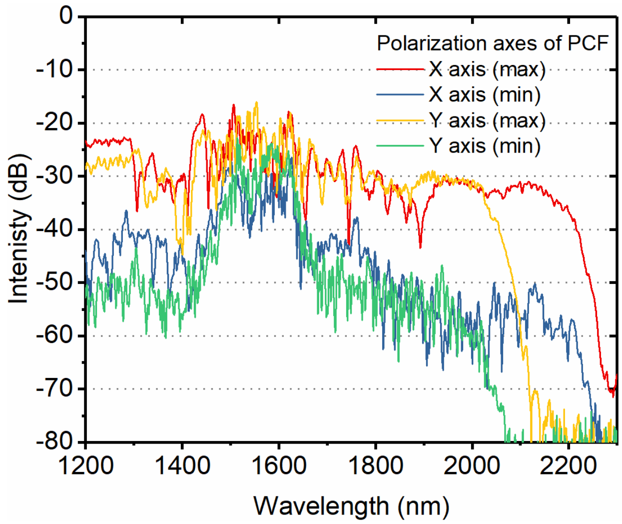

Figure 6.3. Measured spectra of coherent supercontinuum seed signal in both polarization axes of the PM ANDi PCF. The labels "max" represents light coupled and measured in the same axis, while the label "min" represents a case when the light is coupled in one axis and measured in the opposite axis.

I also measured SC broadening with respect to different pump power levels, as shown in figure 6.4. With increasing power (average pump power indicated in the legend), I observed significant spectral broadening up to 2280 nm for maximum available average pump power. The measured maximum average pump power before the coupling lens was 307 mW. These results find an interesting motivation to seed the broadband Tm+Ho-doped fiber amplifier [63] which has remarkable relative intensity noise figures. The absorption and emission cross-section of the Tm-doped fiber is shown in chapter 5, figure 5.6. The emission cross-section extends from 1700 nm to 2100 nm. In this case, I can use the SC generated in X or Y axes to seed the Tm -doped fiber amplifier.

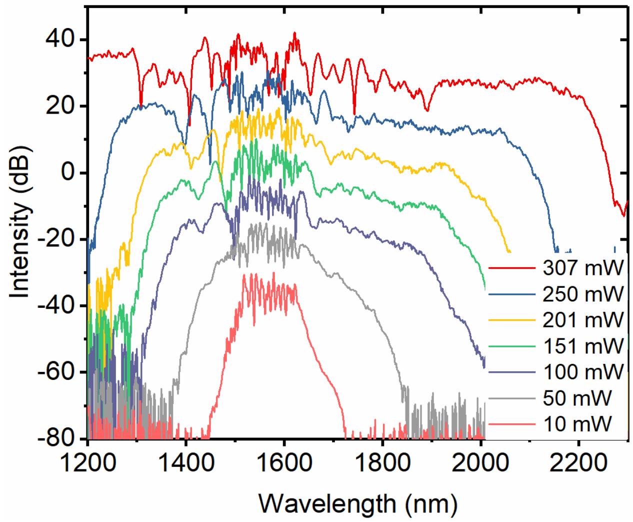

Figure 6.4. Measured spectra of coherent ANDi supercontinuum generation for various average pump powers.

6.2.2 Second stage: Pulse stretching

In this stage, I used the generated SC seed signal from the tellurite PM ANDi PCF to seed the Tm and Er-doped amplifiers. In the beginning, I tested the PMWDM using the broadest PM ANDi SC spectrum available. The spectrum at the output of the two ports are shown in figure 6.5 with the full SC in the background. The 1550 nm port collects the light in the spectral range from 1200 nm up to 2000 nm but its transmission is maximized at 1550 nm. Analogically, the 2000 nm port collects light from 1600 nm and its transmission maximum is around 2000 nm. For the actual seeding of the Tm-doped fiber amplifier, I used the SC from the Y-axis which was sufficiently broad and provided more average power in a small bandwidth of spectrum, than the seed signal obtained in the X-axis of the PCF. Further, the SC pulses were dispersively stretched using a section of a PM2000D fiber, which was 6.55 m long in the Tm-fiber amplifier arm and 4.5 m long in the Er-fiber amplifier arm. The PM2000D fiber has normal dispersion [70] in both the Tm and Er amplification windows and is very well suited to compensate for the anomalous dispersion of the active and passive fibers of the subsequent amplifier system. The measured GVD curve of this fiber is shown in figure 3.6 in chapter 3 and compared to the GVD of the standard PM 1550 used as a pigtail fiber of the passive components in the amplifier. I note that the GVD of the active fibers used in our system was not measured, but based on previous reports, I assumed it to be similar to passive PM1550 fiber in case of a Tm amplifier. In the case of Er active fiber, this assumption proved to be inaccurate.

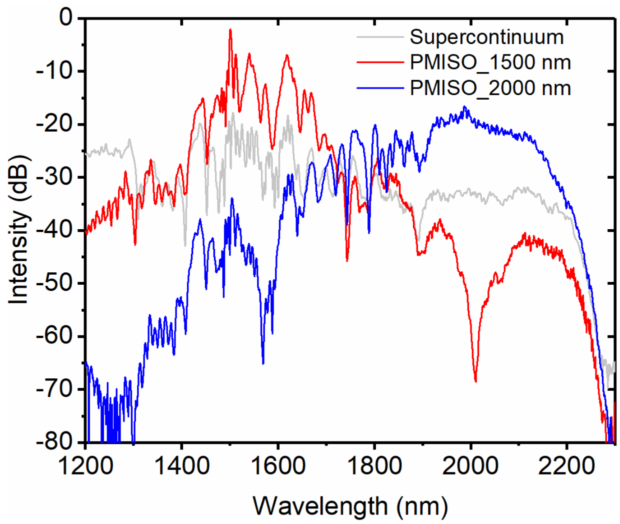

Figure 6.5. Supercontinuum after propagating in PM WDM and PM2000D, measured after passing through a PM ISO. Gray trace represents the input SC pulse spectrum. Red trace is at the spectrum of pulses passing through the 1550 nm port of the WDM, blue trace - at 2000 nm port of the WDM.

At the output of the tellurite PM ANDi PCF, I obtained around 110 mW of average power in the full spectral range covered by the broadened SC spectrum. There is a 20 % loss in the SC power after passing through the output coupling lens, polarizer, and halfwave plate in the experimental setup pictured in figure 6.1. Even though a broadband achromatic lens was used to couple the broadband spectrum into the fiber, still it suffered from chromatic aberrations. Thus the optimum position of the lens was chosen manually so that there was sufficient seed signal power at both the 2000 nm and 1550 nm ports to seed the amplification stages.

6.2.3 Third stage: Pulse amplification

6.2.3.1 PM Tm doped fiber amplifier optimization

The Tm-doped fiber had to be optimized, compared to what was demonstrated in the previous chapter because I desire to have the only required length of fiber to achieve maximum power efficiency and this also reduces the accumulation of higher-order dispersions in the amplifier arm. The emission cross-sections and active fiber properties were introduced in chapter 5. The Tm-doped fiber amplifier section is backward core-pumped by an in -house built EYDF continuous-wave amplifier operated at a wavelength of 1565 nm at 2 W of power. This work begun with a PMWDM temporarily spliced at the input of the active fiber to monitor the leftover pump during the optimization of the active fiber length. The spectrum of the amplified pulses at the output of the amplifier is observed using a spectrometer (Ocean Optics NIRQuest). Figure 6.6 (a) shows the amplified pulses' spectrum at the output of the Tm fiber amplifier (dark blue trace). The spectrum of the pulses at the output of the amplifier is shaped mostly by the Tm-doped fiber gain profile. I obtained 500 mW of average output power with 3 dB bandwidth of 100 nm centered at 1880 nm and 20 dB PER. The fine structure observed in the amplified pulse spectrum at the output of the Tm system is most likely due to a birefringent filtering effect caused by a slight misalignment of the fiber polarization axes before a polarization sensitive element, as discussed in the previous chapter. Figure 6.6 (b) contains results of the measurement of the amplifier output pulses' spectrum recorded for increasing pump powers (driving current of the pump source is shown in the legend). The gray trace represents the unabsorbed SC seed in the Tm fiber amplifier measured at the output before pumping. With the increasing pump power, the amplifier output pulse is shaped by the SC seed signal and the Tm fiber gain characteristic. Since the SC is free-space coupled, I was able to monitor the coupling in each of the fiber amplifying sections by monitoring the seed signal at the output. It is also observed that the coupling of the seed into the Tm or Er amplifier sections depended on the position of the achromatic lens as explained in section 6.1. Either I can choose to have more seed coupled to Tm or Er amplifier section and therefore the output slope efficiency relies on this factor.

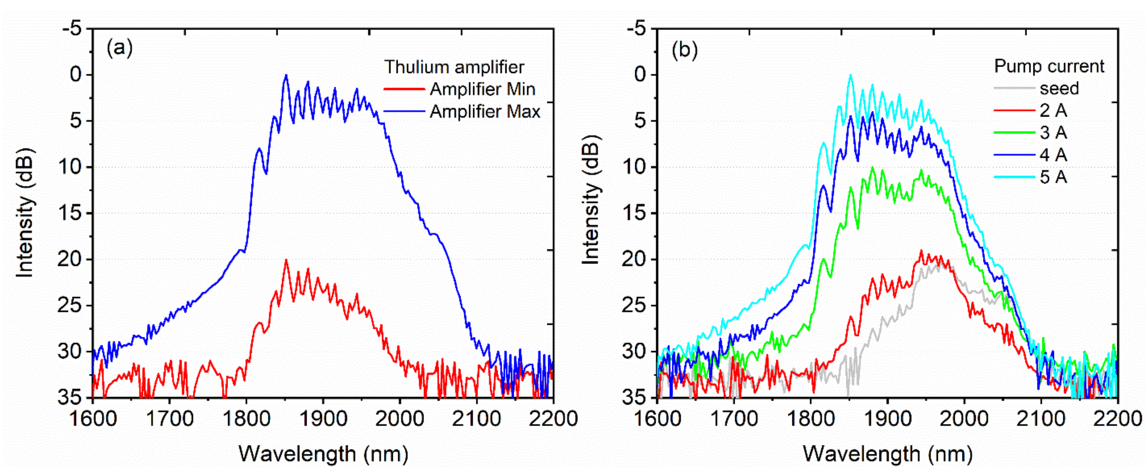

Figure 6.6. (a) Logarithmic scale spectra at the output of the Tm amplifier measured in the slow axis (dark blue) and in the fast axis (red). (b) Amplifier output pulse spectra for different optical pump powers (pump current in legend), (gray trace): seed supercontinuum spectrum measured in an unpumped amplifier.

In figure 6.7, I show measurement results of the output power of the Tm amplifier for two different SC seed powers. It can be observed that with an increase in the SC seed power, the slope efficiency is also increased. For the seed power of 5 mW, I obtained slope efficiency η = 36.8 %, and for 7 mW, η = 39.4 %, that is around 2.5 % increase in the slope efficiency. The maximum output power obtained is 580 mW, when the seed is 7 mW and 500 mW when the seed is 5 mW. Thus, in comparison to the Tm amplifier built in the previous chapter, I obtained better output power, which corresponds to improved slope efficiency. The main factor responsible for the better slope efficiency was the amount of SC seed used which is significantly improved with the use of the tellurite PM ANDi PCF. In this chapter, work involved simultaneous seeding of Er and Tm amplifier arms, which imposed new, stringent requirements on the seed pulse power budget. Replacement of the nonlinear fiber available for the experiments described in chapter 5, with the tellurite PM ANDi PCF answered to these requirements.

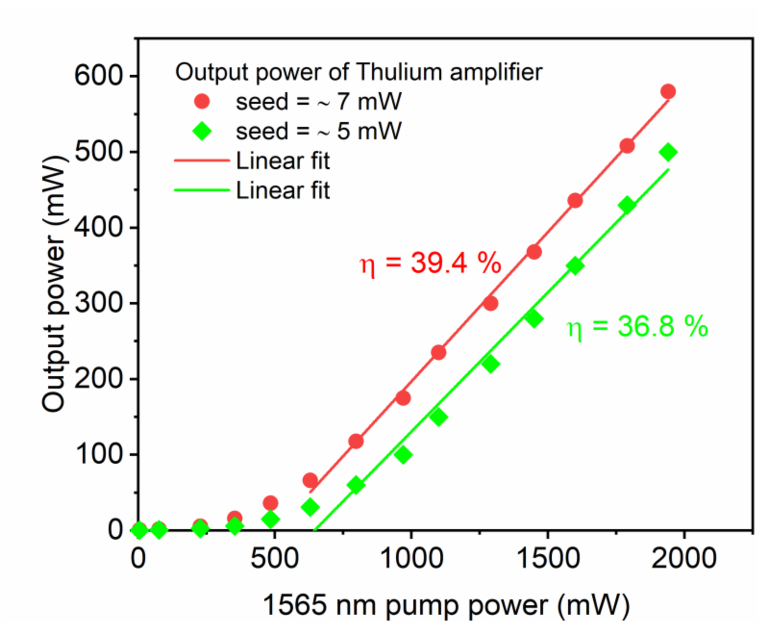

Figure 6.7. The output power of the Tm-doped fiber amplifier with SC seed power of 7 mW and 5 mW, plotted as a function of total launched pump power at 1565 nm. Experimental points are plotted with a linear fit to show the slope efficiency.

Figures 6.8 (a) and (b) show the measured and retrieved FROG traces at the output of the Tm amplifier at 200 mW of average output power. Wavelength scale was converted back to the original from the SHG wavelength. The FROG retrieval error was 6×10^{-3} over a 256 × 256 grid size. The color map of the FROG trace revealed that more than 60% of the total energy was concentrated in the main part of the pulse. The pulse duration was 120 fs considering the Gaussian pulse shape as shown in figure 6.8(d). The compressed pulse has a TBP of 0.858, which is 1.9 times larger than the transform-limited pulse. Here I did not compress the pulse completely for the ease of implementing further experiments, which will be discussed in the following sections of this chapter. Due to the accumulation of significant TOD over the length of the all-fiber system, the simultaneous compensation of GVD and TOD using only optical fibers was not possible. Moreover, the small mode field diameter of the PM1550 fiber used as a compressor contributed to pulse distortion at high pulse energies due to nonlinear effects. LMA fibers or external compression using bulk optics, such as gratings or chirped mirror pairs, could be used for pulse compression even at high pulse energies.

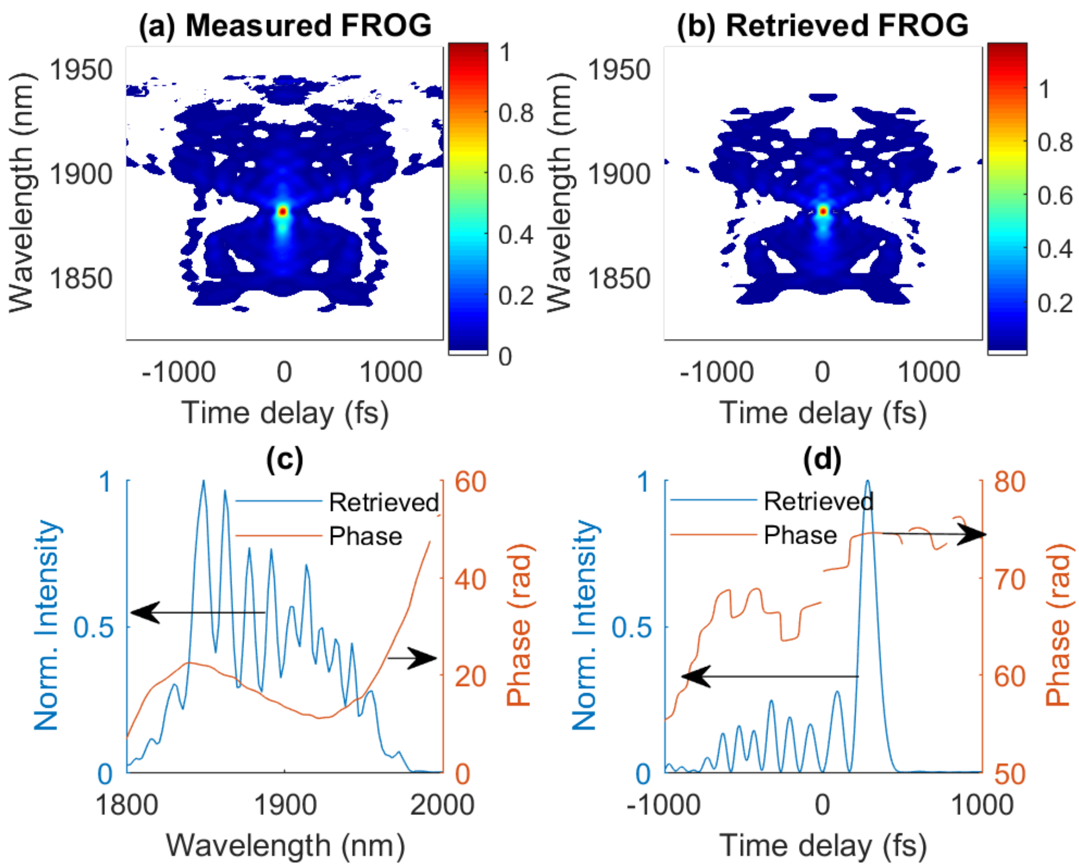

Figure 6.8. Characterization of the Tm amplifier compressed pulse using SHG FROG. (a) Measured FROG trace, (b) retrieved FROG trace, (c) FROG-retrieved spectrum (blue) and phase profile (red), (d) FROG retrieved pulse shape (blue) and phase profile (red).

6.2.3.2 *PM Er-doped fiber amplification*

This amplification stage consisted of a 1.2 m long section of PM single-mode Er-doped silica fiber (iXblue photonics IXF-EDF-HD-PM, 0.2 NA, 36 dB/m core absorption at 977 nm and 75 dB/m core absorption at 1528 nm [200]) with emission and absorption cross-sections as shown in figure 6.9. The absorption peaks are at 977 nm and 1528 nm, emission peak is at 1530 nm.

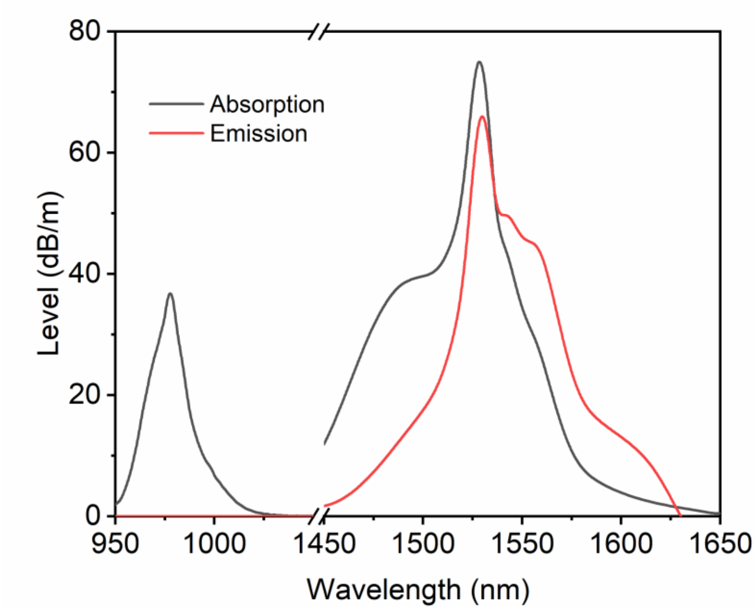

Figure 6.9: Absorption and emission spectra for iXblue Er-doped silica fiber [200].

The Er-doped fiber amplifier arm is backward core pumped by a 976 nm continuous wave laser and the seed is provided from the same supercontinuum source as in the case of the Tm-fiber amplifier. Again, first, the PMWDM is temporarily spliced before the active fiber to monitor the leftover pump during the optimization of Er-fiber length. The optimization was performed to achieve maximum power efficiency. Figure 6.10 summarizes the output power characteristics of the Er-fiber amplifier and the 976 nm pump laser diode. Figure 6.10(a) plots the output power of the 976 nm laser diode as a function of the driving current. The threshold current is ~80 mA. The output power grows linearly with the driving current and reached ~900 mW at 1500 mA. Figure 6.10(b) plots the output power of the PM Er-doped amplifier system as a function of the total launched pump power by 976 nm laser diode. The output power of the SC seeded Er amplifier increased linearly with the pump power with a slope efficiency of 24.8 %.

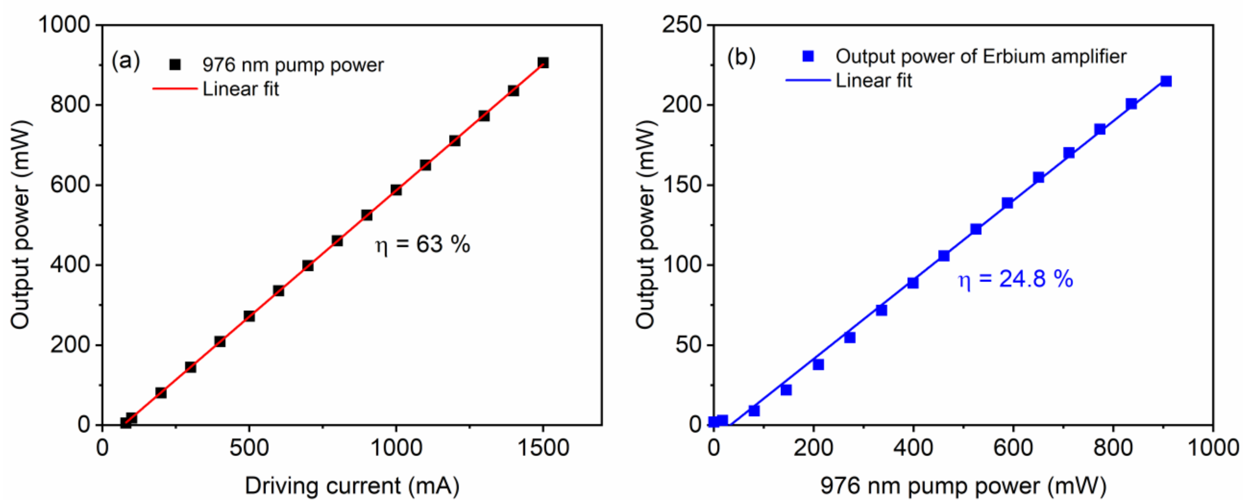

Figure 6.10. Power characteristics of the 976 nm laser diode used to pump the SC seed Er-doped fiber amplifier. (a) Output power as a function of driving current of the 976 nm pump laser diode, (b) output power of Erbium amplifier as a function of total launched pump power. Experimental points are plotted with a linear fit to show the slope efficiency.

Figure 6.11 (a) plots the amplified spectrum at the output of the Er fiber amplifier in a log scale (dark blue). The spectrum of the pulses at the output of the amplifier is shaped mostly by the Er-doped fiber gain profile and SC seed. I obtained 220 mW of average output power centered at 1555 nm with a 3 dB bandwidth of 64 nm, and 15 dB PER. In figure 6.11 (b) I present the output spectrum at the end of the amplifier measured by increasing pump power (driving current of pump source are shown in the legend). The black spectrum represents the unabsorbed SC seed measured at the output of the unpumped Er fiber amplifier.

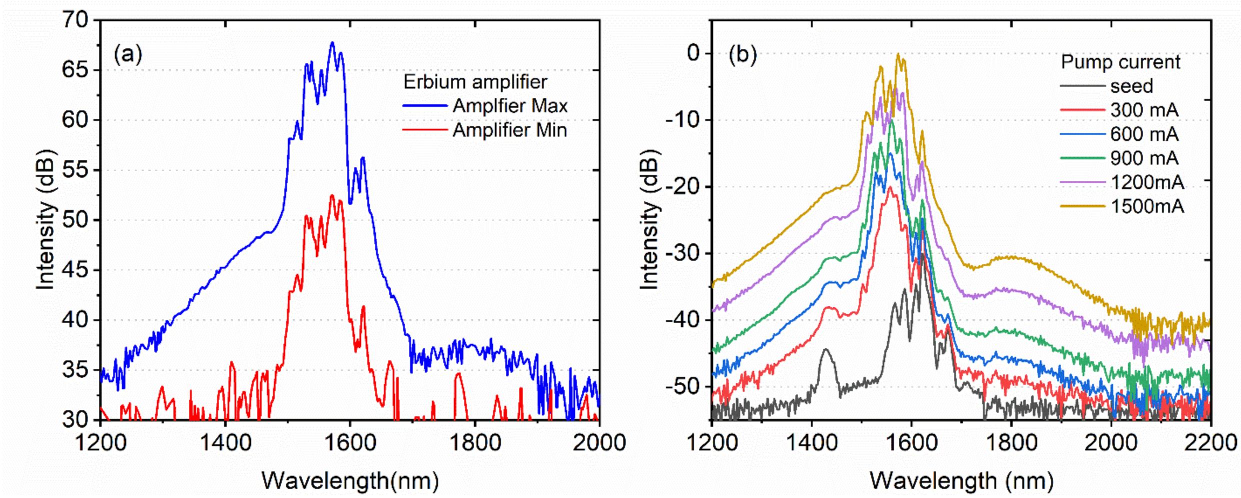

Figure 6.11. (a) Logarithmic scale spectra at the output of the Er amplifier measured in the slow axis (dark blue) and in the fast axis (red). (b) Amplifier output pulse spectra for different optical pump powers (pump current in legend), (gray trace): seed supercontinuum spectrum measured in an unpumped amplifier.

Figures 6.12 (a) and (b) show the measured and retrieved FROG traces at the output of the Er amplifier. Wavelength scale is converted back to the original from the SHG wavelength. The FROG retrieval error was 2×10^{-2} over a 256 × 256 grid size. The color map of the FROG trace revealed that more than 60% of the total energy was concentrated in the main part of the pulse. The pulse duration was 56 fs considering the Gaussian pulse shape, as shown in the figure. 6.12(d), which is close to a transform-limited pulse of 53 fs. Also due to the accumulation of significant TOD over the length of the all-fiber system, as the simultaneous compensation of GVD and TOD using only optical fibers is not possible. Moreover, the small mode field diameter of the PM1550 fiber used as a compressor distorts the pulse at high pulse energies due to nonlinear effects, especially in this case we observe soliton at the longer section of fibers. LMA fibers or external compression using bulk optics, such as gratings or chirped mirror pairs are much suitable for pulse compression even at high pulse energies.

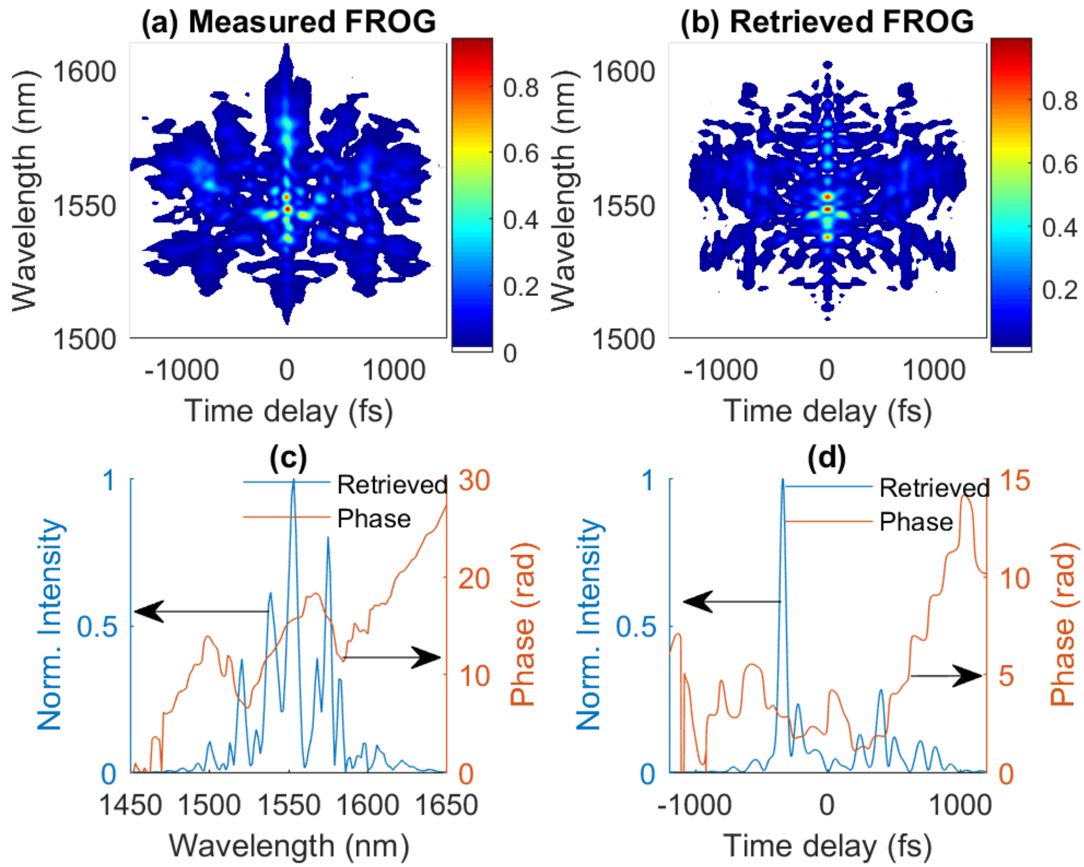

Figure 6.12. Characterization of the Erbium compressed pulse at the output using SHG FROG. (a) Measured FROG trace, (b) retrieved FROG trace, (c) FROG-retrieved spectrum (blue) and phase profile (red), (d) FROG retrieved pulse shape (blue) and phase profile (red).

6.2.3.3 Sum frequency generation from Er and Tm amplifier signals

In this section, I discuss the SFG signal generation between Er and Tm amplifiers. The main goal is to match the optical path lengths between the two arms. The amplifiers discussed above are based on the all-fiber configuration as it is quite challenging due to very long path lengths. The optical path length is described as the geometrical length of the optical wave propagation in the fiber, which is refractive index (RI) dependent and the length of the fiber used in each arm. Even though it slightly varies with respect to wavelength, for initial calculations I considered it to be similar. Apart from active fibers, we know the relative RI of the passive fibers measured during the dispersion measurements or we can simply assume the values for the silica fiber. The two varieties of passive fiber in my amplifier system are PM2000 and PM1550 fiber. In the case of Tm active fiber, I consider RI to be the same as PM1550. But from the experiments, we realized that it is different in the case of Er active fiber due to different core doping concentrations.

Consequently, I know all the parameters to match the optical path lengths in each arm and temporally overlap the signals by adding or subtracting the fiber lengths. At the same time, the pulses at the output should be compressed in each arm. Tm amplifier was built first based on previous knowledge of dispersion compensation calculations and it needs a longer length of fiber compared to the Er amplifier section. In the second step Er amplifier arm was constructed by monitoring the pulse at the output to match the optical path length to the Tm amplifier arm and to obtain the compressed output. It is also important to note that, without this goal, I could use a lesser amount of fiber in the Er arm. More the fiber length, higher-order dispersion is difficult to compensate, which gives side pedestal in compressed output and is clearly seen in figure 6.12 (d).

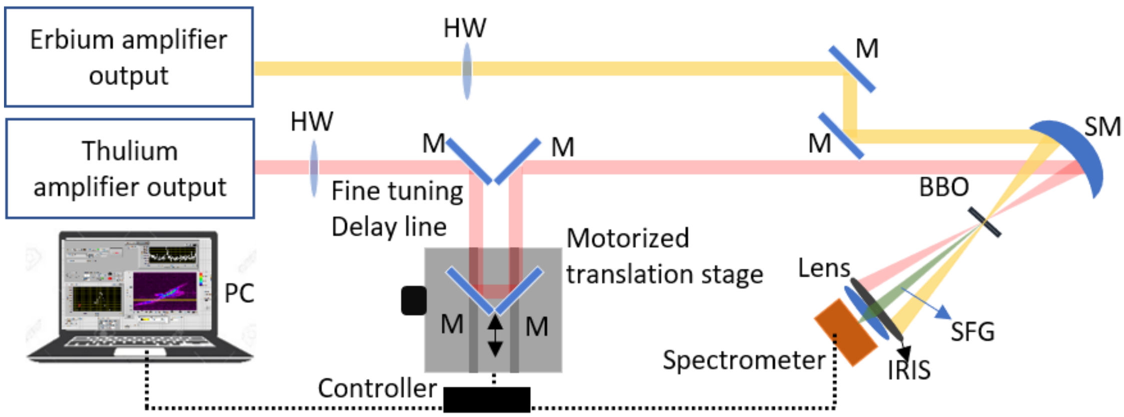

Figure. 6.13. Schematic setup for sum frequency generation between Erbium and Thulium amplifier signal. M: highly reflective mirror; HW: half-wave plate; SM: spherical mirror; BBO: β- barium borate crystal; PC: computer; SFG: sum frequency generated signal.

Figure 6.13 shows the setup for SFG between Er and Tm amplifiers outputs. This setup is similar to the XFROG setup, but instead of the known gate pulse and the unknown pulse (the measured pulse), I am using two pulses with known properties. The pulses obtained at the amplifier outputs of each amplifier were only roughly compressed, which was shown in figures 6.8 and 6.12. The purpose behind this was to obtain SFG and, in the following part of discussion in this chapter, to explore the RIN level of this process in comparison to RIN levels of individual amplifiers in each of the arms. To that end, the maximization of chirp compensation for obtaining the shortest pulse possible was replaced with moderate compression, which was deemed sufficient to facilitate the SFG. The average output power at each amplifier output was 200 mW. To measure the optical path length difference between the Tm and Er amplifiers, the pulses from the output of each amplifier were combined using a dichroic mirror and measured using an oscilloscope and a PD.

The Tm-doped fiber amplifier pulse was lagging by 80 ps, which corresponded to 3 cm of optical path length in air. To compensate this dealy, the Tm amplifier's output pulses were passed through an optical delay line with a motorized translation stage to match the optical path length to the Er amplifier arm and to control it in the experiment. Both the signals were focused onto a 2 mm thick BBO crystal using a spherical mirror, to generate SFG. A relatively thick BBO crystal was used to increase the SFG signal level. The SFG signal was recorded as a function of the time-delay between the Er and Tm signals using a compact Czerny-Turner spectrometer (Ocean Optics, 350 – 1000 nm sensitivity range, 2.0 nm resolution). The polarization state of both pulses was controlled with broadband half-wave plates. Any unconverted Er and Tm signals transmitted through the BBO crystal were filtered with an iris before the spectrometer.

Figures 6.8 (d) and 6.12 (d) shown earlier illustrate the retrieved temporal profiles at the end of Tm and Er amplifiers, respectively. Both traces show side pedestals due to not fully compensated higher-order dispersion. The generated SFG signal has complicated pulse shape due to the mixing of Tm and Er amplifiers pulses as shown in figure 6.14. The retrieval of full-field information of this signal was challenging, but I note it did not preclude RIN measurement and analysis, the results of which are discussed in the following section.

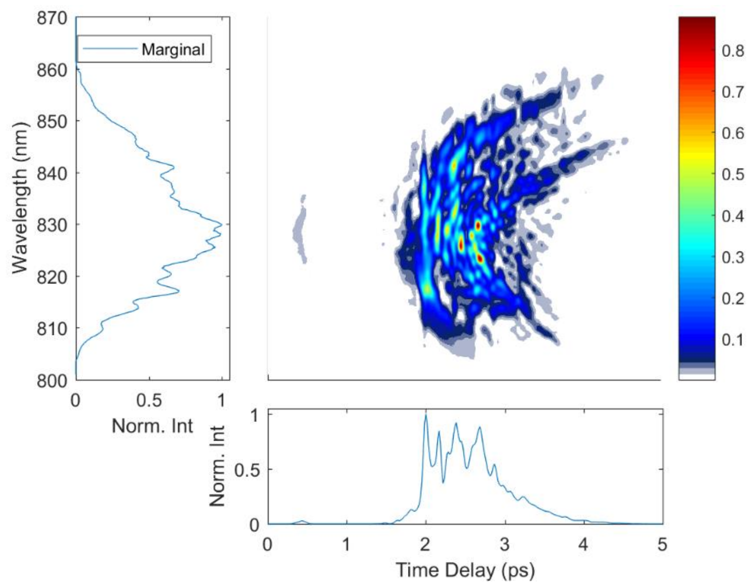

Figure 6.14. Measured group dealy trace of the sum frequency generation (SFG) signal obtained from nonlinear mixing of the Erbium and Thulium amplifier signals in a BBO crystal. The spectral and temporal projection displays the marginal of the spectrogram. Y-axis is the original SFG scale.

6.2.4 Relative intensity noise

In the final stage of the work, I performed a noise characterization experiment using a similar approach to the one in chapter 5. RIN measurements were performed with the same 12.5 GHz InGaAs broadband photodiode (PD), sensitive over the entire spectral bandwidth of the SC seed signal (ET-5000F from Electro-Optics Technology). Agilent E4443A electronic spectrum analyzer (ESA) was used to record the Radio Frequency (RF) spectrum. The light from the amplifier system was directly coupled into the PD using a single-mode fiber. For the linear operation of the PD, the power was maintained around 1 mW and the DC photocurrent was monitored at the output of the photodiode using a digital multimeter.

Figures 6.15, 6.16,6.17 show the amplitude noise spectrum, as well as the integrated rms RIN in the range 10 Hz - 1 MHz measured at different positions along the amplifier. For the Er: fiber seed laser, the RIN was measured at a level 0.035% in the previous chapter. Figure 6.15 shows the measured intensity noise of the SC used in this chapter. The RIN was measured with and without a filter. The filter used in this experiment had 500 nm bandwidth centered at a wavelength of 2000 nm, hence only RIN of the long-wavelength SC wing was measured. The integrated RIN of the entire SC (no filter in the setup) was 0.041% while with the filter it was 0.034%. Hence we can see that RIN above 1750 nm is very identical to Er: fiber seed laser and most of the noise contribution come from the signal below 1750 nm. This attributes to the excitation of cladding modes in the pump region and the relatively low PER, which is seen as noise contributions in the frequency range 200 Hz - 1 kHz.

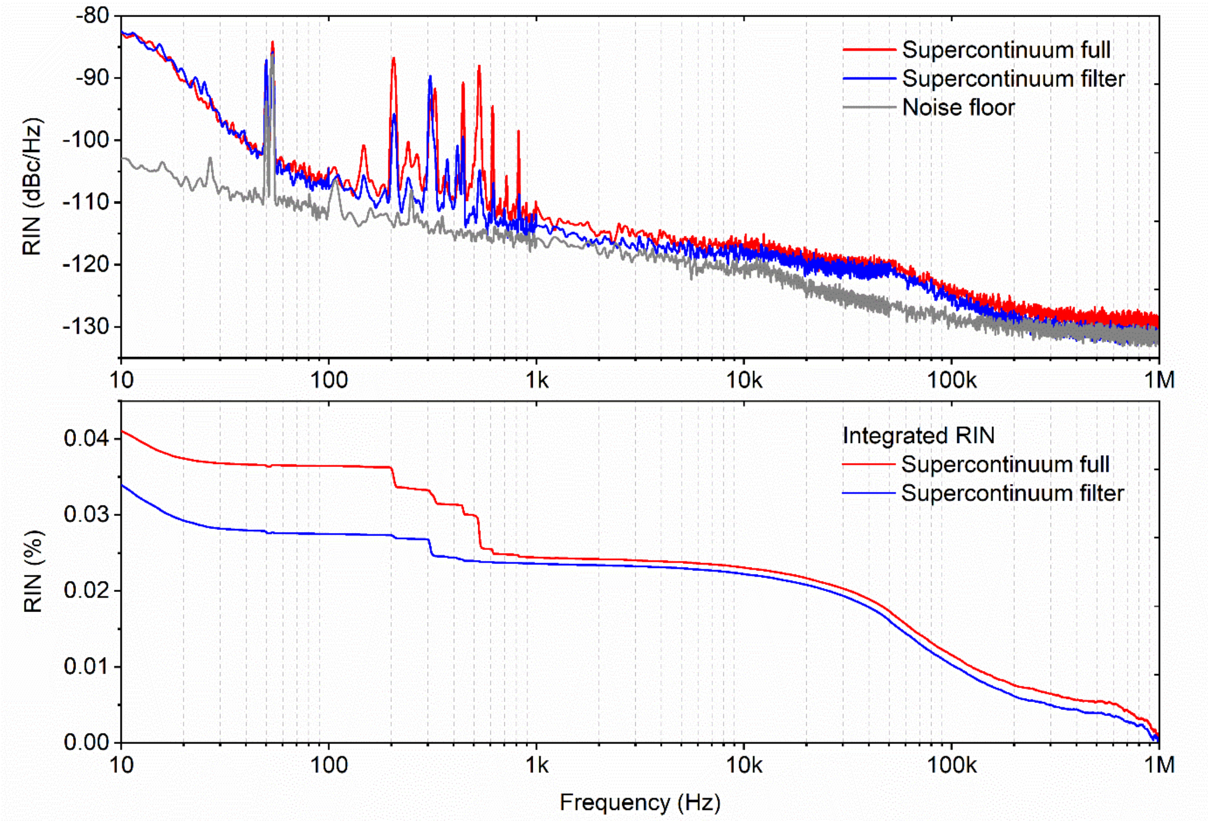

Figure 6.15. Measured noise characteristics of the full-bandwidth supercontinuum (red trace) and of filtered SC, with a bandpass filter centered at a wavelength of 2000 nm (blue trace). The top plot shows the spectrally resolved amplitude noise in the frequency range from 10 Hz to 1 MHz, while the bottom plot shows the total integrated RIN. The noise floor of the measurement setup is shown in gray in the top plot.

Similarly, RIN of the Tm amplifier was measured for different pump powers to understand in-depth the noise contribution during the amplifier operation. Hence the signal on the PD was maintained roughly the same for comparison of results. The RIN is measured in a frequency range from 10 Hz to 1 MHz, and most of the noise signals are observed in the range of 100 Hz to 1 kHz as shown in figure 6.16. From the integrated RIN spectrum, I can observe that the RIN characteristics measured for different pump powers delivered to the amplifier are very close to each other in the range of 1 kHz to 1 MHz. Below 1 kHz, the significant difference is observed for different pumping currents, with RIN being the highest at 0.041 % for low pumping current and lowest at 0.035 % for the maximum pumping current. This was clearly observed in the intensity difference of the noise feature in the range of 100 Hz to 1 kHz. Hence, the integrated RIN at the output of the Tm amplifier developed in this chapter is very close to the RIN of the Er: fiber seed laser and the long-wavelength part of the SC. This Tm amplifier system additionally improved the RIN compared to one described in chapter 5 [163].

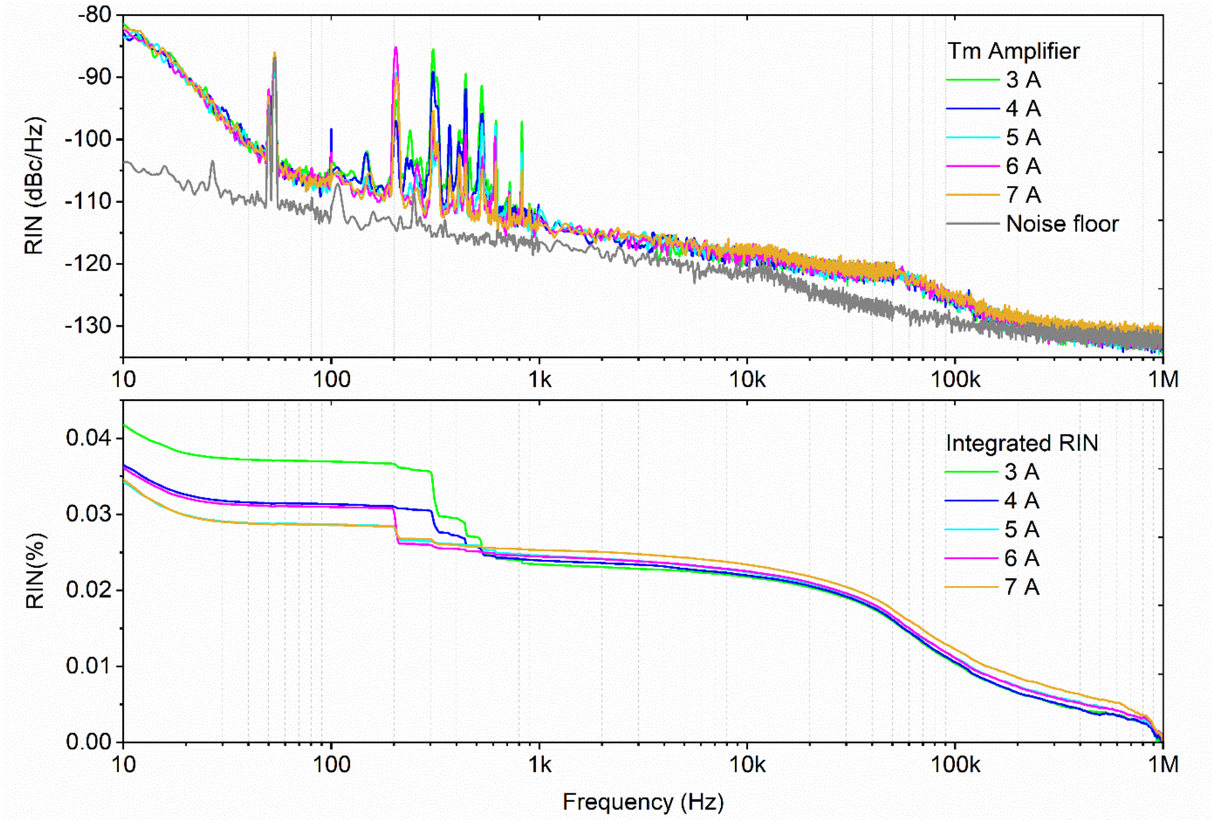

Figure 6.16. Measured noise characteristics of the Tm amplifier at different pump powers (legend shows corresponding pump current). Top plot shows spectrally resolved amplitude noise in the frequency range 10 Hz - 1 MHz, while the bottom plot shows the total integrated RIN. The noise floor of the measurement setup is shown in gray in the top plot.

Similarly, RIN of the Er amplifier was measured for different pump powers to observe the noise contribution during amplification, as shown in figure 6.17. The signal on the PD was maintained at 1 mW for all the measurements in order to compare the results. The RIN was measured in a frequency range from 10 Hz to 1 MHz, and most of the noise signals are observed in the range of 100 Hz to 1 kHz. From the integrated RIN spectrum, I can observe that the RIN decreases with an increase in pump power, which is similar to the case of the Tm amplifier. Below a frequency of 1 kHz, a significant difference in the intensity peaks for different pumping currents can be observed. For low pumping current, the RIN is the highest at 0.055 % and for the maximum current of the amplifier pump diode, the amplifier RIN of 0.049 % is lowest. Compared to the Tm amplifier RIN, the Er amplifier has 40% higher RIN level, which is attributed to the small PER of the SC seed signal in the spectral region overlapping the Er amplifier gain band – and the spectral region of the SC seed signal pump region which overlaps with the Er amplifier gain band. The integrated RIN at the output of the Er amplifier developed in this chapter is increased by the factor of roughly 1.4 compared to the Er-doped fiber-based femtosecond laser at the front-end of the entire system, and compared to the long-wavelength (>1750 nm) part of the SC seed signal.

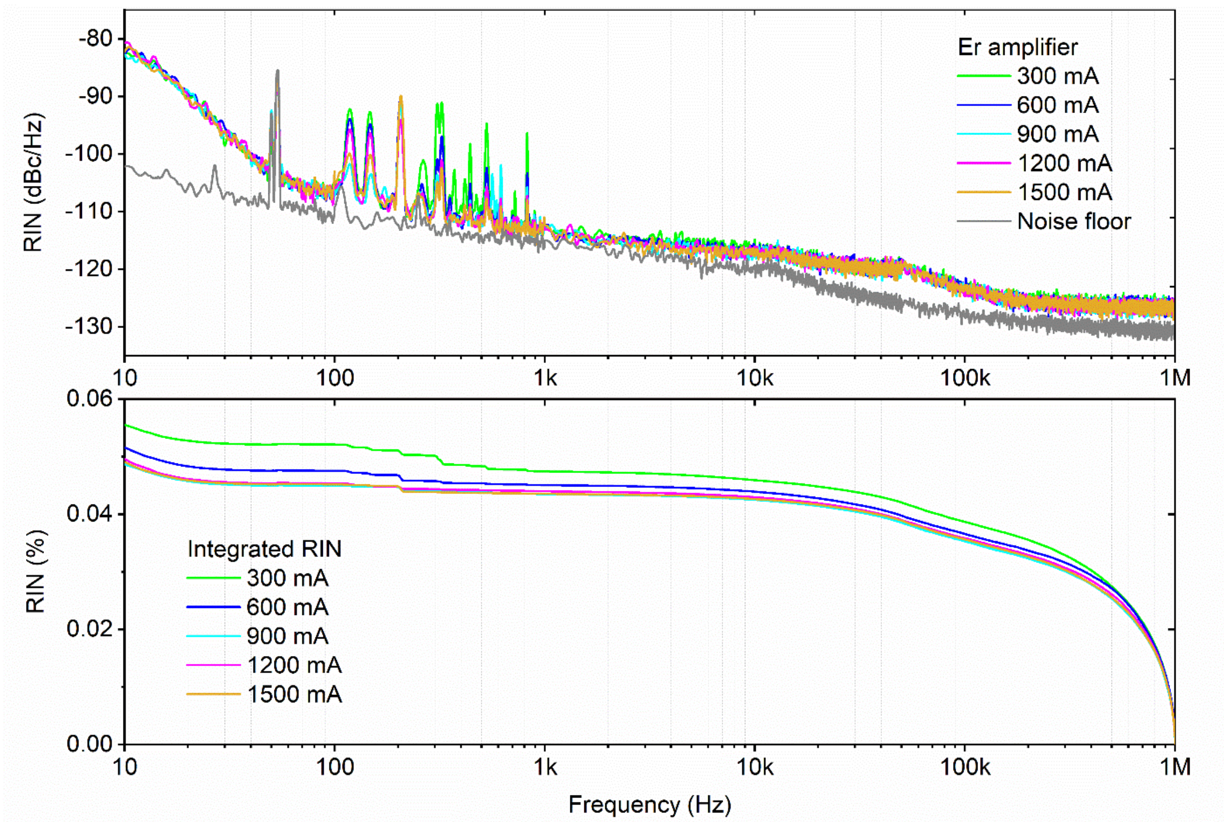

Figure 6.17. Measured noise characteristics of Erbium amplifier at different pump powers (legend shows corresponding pump current). The top plot shows spectrally resolved amplitude noise in the frequency range of 10 Hz - 1 MHz, while the bottom plot shows the total integrated RIN. The noise floor of the measurement setup is shown in gray in the top plot.

In the final part of the work described in this chapter, RIN was measured for the SFG signal obtained from the nonlinear mixing of the Er and Tm amplifier outputs. The SFG signal was in the order of microwatts and the beam was strongly divergent after the BBO crystal used for mixing. This posed an additional challenge during characterization of this signal because a maximum of 1 mW of average power of the SFG signal was obtainable. After passing through the optics it was very difficult to use the fiber-coupled fast photodiode as used before. This was solved by replacing with a free space PD with 8 MHz bandwidth to acquire the data. In addition, I used a voltage amplifier (VA) to amplify the SFG signal, which imposed a low-frequency limit of the RIN measurement at 1kHz (amplification bandwidth of this device was 1 kHz - 1 GHz). The data on ESA was recorded in 2 parts, 1 kHz to 100 kHz and 100 kHz to 10 MHZ. Figure 6.18 shows the amplitude noise spectrum as well as the integrated rms RIN of the SFG signal. By scanning the time delay between Er and Tm arm signals, complete SFG RIN was obtained. From figure 6.14, it can be observed that intensity is different at different positions. Hence, RIN was measured at the position where the maximum intensity was obtained during the SFG scan. The resulting integrated RIN of the SFG signal was 1.47 %, whereas the noise floor itself was 0.7%. in the range of 1 kHz to 10 MHz as shown in figure 6.18, which is very high compared to both Er and Tm amplifier. A similar scenario was observed previously [201]: The SFG RIN was 0.58 % when the signal was measured in a frequency range up to 1 MHz. The increase in the SFG RIN in my work can actually originate from different parameters in the system. One of the contributions is Er amplifier noise in the higher frequency range when measured from 10 Hz up to 10 MHz and 50 MHz the rms RIN was 0.12 % and 0.3 % respectively. Secondly, SFG signal is generated from both Tm and Er arms and has to travel in the free space optics and it can increase the jitter and overall amplitude noise. Finally, the noise from the VA during the amplification of a weak signal. Hence overall the RIN of SFG is quite high compared to individual amplifiers.

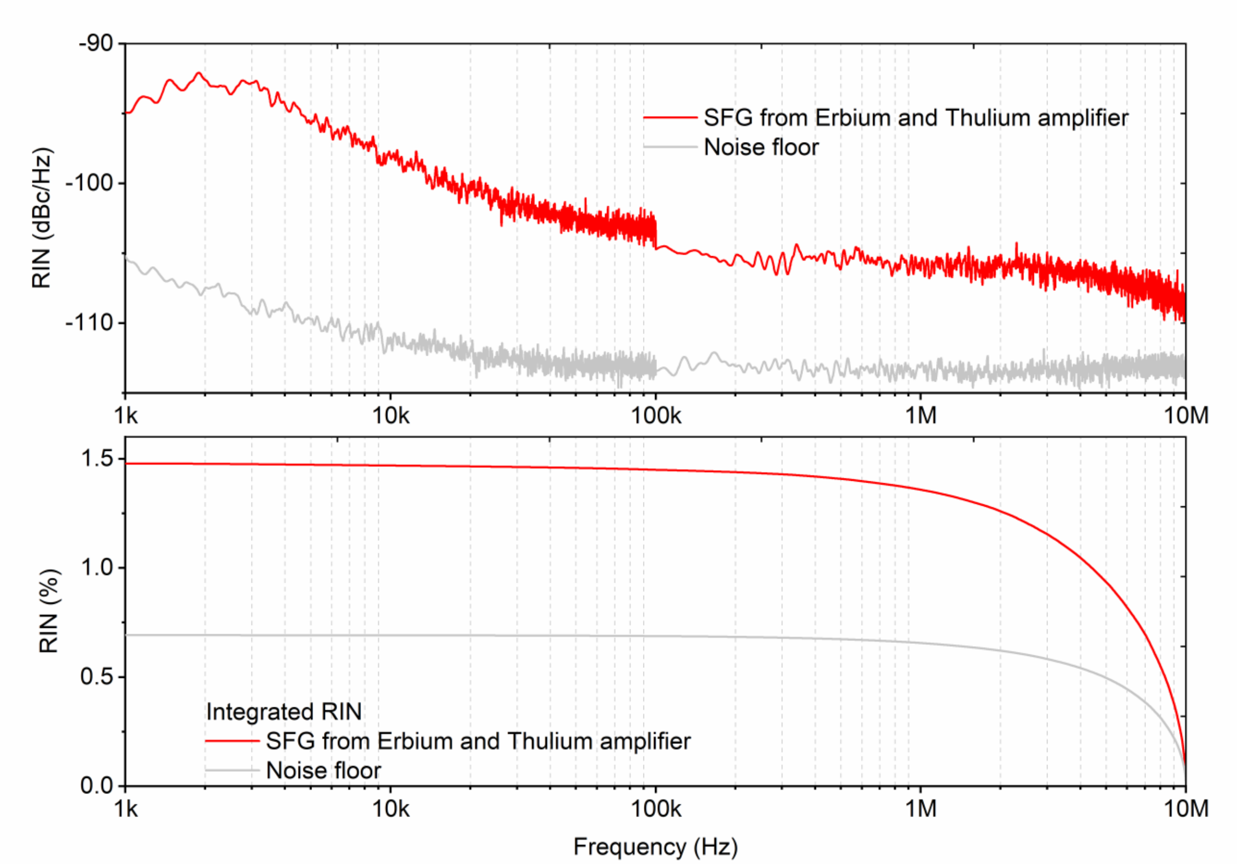

Figure 6.18. Measured noise characteristics of the SFG signal generated from the Erbium and Thulium amplifier. Top plot shows spectrally resolved amplitude noise in the frequency range 1 kHz - 10 MHz, while the bottom plot shows the total integrated RIN. The noise floor of the measurement setup is shown in gray.

6.3 Conclusions

In this chapter, I demonstrated simultaneous and coherent seeding of the Tm and Er doped fiber amplifier system. The system based on FCPA enabled the realization of linear pulse amplification and all PM architecture removed white noise fluctuations caused by PMI

Improved pulse amplification in Tm doped amplifier system was observed compared to the one demonstrated in chapter 5 [163]. I obtained 580 mW of average output power, 3 dB bandwidth of 100 nm centered at 1880 nm, with 20 dB PER when the highest SC seed available. The pulse was compressed to 120 fs at 200 mW output average power. The lower RIN obtained for maximum output power in the range of 10 Hz – 1 MHz is only 0.035% at the amplifier output, which is virtually identical to the RIN of the Erbium-fiber laser driving the SC.

SC seed Er amplifier system delivers 220 mW of average output power centered at 1555 nm with a 3 dB bandwidth of 64 nm, and 15 dB PER with output pulses compressed to 56 fs. The corresponding RIN was 40% excess in comparison to the Tm amplifier in the range of 10 Hz – 1 MHz. This can be improved by using better PER SC seed in the 1550 nm region.

In the final part, SFG was generated between the Tm and Er amplifier. The SFG RIN was 1.47 % and its noise floor was 0.7%. in the range of 1 kHz to 10 MHz The noise was higher than that of the Tm amplifier and front-end laser but comparable to the soliton systems. The increase can be related to low PER in the Er amplifier region leading to PMI, which leads to significant pulse-to-pulse fluctuations. This is well supported by complex SC generated based on pump pulse structure. This was explained in chapter 4, relating it to the temporal low-level pedestal of the femtosecond front-end laser.

Er and Tm amplifiers are inherently synchronized as both amplifiers are seeded by the same SC and have the same repetition rate as the front-end laser. In addition to the low RIN of individual amplifiers, if the carrier-envelope offset (CEO) of the new spectral components produced by SC is retained during amplification, the two output compressed pulses from Er and Tm can be combined coherently to obtain few-cycle pulses.

Therefore, the passively synchronized amplifier pair scheme, proposed in this work with the common ANDi SC seed is not defeated by RIN level increase, since it stemmed from limitations of the disposed components of the experimental setup (ie. non-transform limited femtosecond pump pulse at the front end and limited PER of the SC seed around 1560 nm). These factors could be improved at the technical level, employing improved PCF design or chirp management of the driving lasers, without fundamental changes to the coherent, synchronized seeding of the dual amplifier scheme proposed in this dissertation.

Chapter 7. Conclusion and future developments

The dissertation is focused on the research of the interplay of linear optical phenomena including predominantly dispersive pulse stretching, with nonlinear optical effects, occurring in tight spatial confinement over large distances. Presented implementation involved optical fibers, including standard polarization maintaining active and passive fibers, as well as custom nonlinear photonic crystal fibers. The main objectives of the thesis were concentrated on elaborating methods enabling separation of noise-susceptible nonlinear dynamics from amplification of broadband, coherent seed signals originating from mode-locked lasers. Revealing the mechanisms governing structuring of self-seeded, coherent supercontinuum generation was considered a secondary objective in the work because it contributed to the understanding of the physics behind fine, sub-25 fs structuring of coherent supercontinuum pulses used as seeds in the amplifiers.

Work done is the scope of this dissertation was set apart from the state-of-the-art in ultrafast, fiber-based amplification in that it avoided soliton seeding, relying instead on positively chirped broadband signals generated in all-normal dispersion nonlinear fibers. As a consequence, soliton-related nonlinear processes, such as fission and soliton self-frequency shift were eliminated from the amplification process. This was important because opposed to previous, literature demonstrations, the related noise was not amplified in the amplifier along with the seed signal. Resulting relative intensity noise levels measured for the developed amplifier systems were a factor of 10 smaller, that the best soliton-seeded implementations reported earlier in literature.

FCPA configuration was employed to build all amplifiers, which served as experimental platforms during the work. The setups were designed using the GVD characteristics of commercially available fibers and custom, nonlinear photonic crystal fibers, measured over the entire spectral range relevant to the operation of the investigated devices. The proper combination of normal and anomalous dispersion components ensured optimal pulse stretching and compression even when operated at high pump power levels. In chapter 3, firstly I measured the GVD in a series of commercially available ultra-high numerical aperture fibers in a broad spectral range which covered the typically used erbium, holmium, and thulium dopant ions' emission wavelengths. The literature review found that the available dispersion values of such fibers were mostly estimated based on the calculations or only measured at a specific wavelength, which is inadequate for the design of ultrafast fiber-based light sources. To address this shortcoming, I employed a spectral interferometry-based dispersion measurement method. These results served as a guideline for the selection of appropriate fibers and their lengths for pulse stretching and compression in the design of ultrafast fiber amplifiers in my work. They were also published in the Journal of Optical Society of America B [70].

ANDi SC served as a seed for the development of a broadband low noise amplifier system. Therefore, to understand the SC dynamics, it is very important to test the dispersion characteristics. As a result, I characterized the physically developed all-solid glass, ANDi, weakly PM PCFs in terms of dispersion and birefringence. Besides, the SC produced by silicate ANDi PCF and silica/Ge:silica core PCF was spectro-temporal characterized using XFROG in chapter 4. SPM and OWB were identified as the dominant nonlinear effects in the SC generation dynamics, preserving the temporal integrity of the SC pulse. TDP was employed for XFROG retrieval, which further demonstrates its exceptional efficiency by reconstructing the complex spectrally broadband SC pulses. The temporal fine structure and oscillations on time scales of < 6 to 8 femtoseconds were observed, which is linked to the low-level pedestals of the pump pulse. This is further confirmed by GNLSE simulations by considering pump pulse obtained from measurements and temporal filtering the side peaks of the pump pulse. For the first time, the fine, femtosecond-level structure of the otherwise uniform, normal-dispersion supercontinuum pulses were reconstructed accurately using standard, scalar GNLSE, albeit parametrized with physical data on the output pulses of the driving femtosecond laser. This part of the work also revealed signatures of incoherent noise amplification due to PMI in weakly birefringent fiber samples. Results obtained in this part of the work were accepted for publication in Optics Express [178]. Based on these results, nonlinear fibers with designed, normal dispersion characteristics have been implemented in the following stages of amplifier design in my work.

In chapter 5, an all-PM Tm-doped fiber amplifier seeded by coherent ANDi SC was demonstrated. The spectral-temporal characteristics, amplification, and noise of the amplifier were measured at the output. I obtained 96 fs pulses with 350 mW output power at 100 MHz, centered at 1900 nm with a RIN of 0.04% (10 Hz - 1 MHz), which was virtually identical to the RIN of the Erbium-fiber laser driving the SC seed signal. The RIN of the developed system was an order of magnitude lower than similar systems previously seeded with Raman solitons. This highlights the superior noise properties of ANDi SC and their potential as ultra-low noise seed sources for broadband, high power ultrafast fiber amplifiers, and frequency combs. Results obtained in this part of the work were published in Optics Express [163]. This system can be further employed to pump the PCF in the 2 μm window to extend the SC bandwidth. Recently it has been utilized to study the soliton self-frequency shift in a suspended core tellurite soft glass fiber [202].

In the next part of the work, ANDi SC seed was used to demonstrate the simultaneous seeding of an erbium-doped fiber amplifier, along with the Tm-doped unit. A new SC seed was chosen with improved output power and PER made of tellurite glass microstructured PM PCF, based on feedback, which I was able to work out in the course of detailed, XFROG characterization and e-PIE reconstruction of full-field information on the seed signals. Detailed spectral-temporal, amplification, and RIN measurements were performed. Improved amplification was observed in the Tm region with 580 mW of average output power, 3 dB bandwidth of 100 nm centered at 1880 nm compressed to 120 fs, with 20 dB PER and 0.035% RIN (10 Hz - 1 MHz). This was directly related to larger seed power available for the improved design of nonlinear fiber used in the system. Importantly, enhanced PER also corresponded to decreased RIN figure, compared to amplifier implementation investigated in chapter 4, despite increased output power level. The erbium-doped fiber amplifier system delivered 220 mW of average output power (pump power limited) centered at 1555 nm with a 3 dB bandwidth of 64 nm, and 15 dB PER with output pulses compressed to 56 fs and RIN was 0.049% (10 Hz - 1 MHz). These RIN levels remain an order of magnitude below state-of-the-art soliton-seeded systems and provide evidence confirming the thesis of the dissertation about the superiority of all-normal dispersion dynamics in the seeding of ultrafast amplifiers, over their soliton-based counterparts. A sum-frequency signal has been generated between the two branches of the simultaneously seeded Er and Tm amplifiers and their RIN was measured at around 0.7% above the detector noise floor. It is to be noted, that no active phase control or carrier-envelope phase offset (CEO) control was implemented between the two arms of the system. This result can be considered a proof of principle platform for wavelength-division multiplexed femtosecond pulse amplification or few-cycle pulse synthesis and completes the list of objectives of the dissertation.

Future developments

The SC seed to the amplifier stage contains free space optics which can be made fully fiberized by splicing the PCF to the amplifier stage. In order to achieve this, silica PM PCF should be implemented to make the completely free from alignments. Silica PM PCFs for seed signal generation were tested in scope of the dissertation, and although their parameters (most notably the spectral reach of generated supercontinuum signal) was either insufficient to fully cover Tm-fiber amplifier gain band or was achieved due to mixed normal-anomalous dispersion dynamics, there exists the potential for fully-fiberdized variants of amplifiers investigated in the scope of this work.

In chapter 6 the amplification of the Er amplifier is limited by pump power, which can be improved by choice of high-power pump sources. The compressed pulses had pronounced side pulses and low-level pedestals due to the uncompensated higher-order dispersion, which could be improved by further changes to the amplifier configuration. These could include: (i) Replacing the active Er-doped fiber from anomalous dispersion by normal dispersion fiber (which is currently available in the market) would help to obtain the higher amplified output. (ii) The use of properly designed dispersion compensating fiber (DCF) for compression can account for higher-order dispersion compensation.

The output of the two amplifiers is intrinsically synchronized due to the same seed pulse that originates from the pump laser and thus has the same repetition rate. If the CEO of the new spectral components generated by SC is retained during the amplification process, the two-output compressed pulse can be combined coherently as a way of ultimate optimization of output pulse temporal compression. With the further extension of SC seed to 1000 nm – which would have to involve PCF engineering, the Yb-doped fiber gain band could be simultaneously addressed along with Er and Tm amplifiers, which would offer access to coherent, soliton dynamics-free, and thus ultra-low noise few- and single-cycle pulse synthesis.

References

1. A. H. Zewail, "Femtochemistry: recent progress in studies of dynamics and control of reactions and their transition states," J. Phys. Chem. **100**, 12701–12724 (1996).

2. U. Keller, "Recent developments in compact ultrafast lasers," Nature **424**, 831–838 (2003).

3. S. Rota-Rodrigo, I. Ibañez, and M. Lopez-Amo, "Multi-wavelength fiber laser in single-longitudinal mode operation using a photonic crystal fiber Sagnac interferometer," Appl. Phys. B **110**, 303–308 (2013).

4. Y.-G. Han, T. V. A. Tran, S.-H. Kim, and S. B. Lee, "Multiwavelength Raman-fiber-laser-based long-distance remote sensor for simultaneous measurement of strain and temperature," Opt. Lett. **30**, 1282–1284 (2005).

5. M. Azimipour and R. Pashaie, "Nonlinear optical signal processing on multiwavelength sensitive materials," Opt. Lett. **38**, 4324–4326 (2013).

6. J. J. Veselka and S. K. Korotky, "A multiwavelength source having precise channel spacing for WDM systems," IEEE Photonics Technol. Lett. **10**, 958–960 (1998).

7. A. Schliesser, N. Picqué, and T. W. Hänsch, "Mid-infrared frequency combs," Nat. Photonics **6**, 440–449 (2012).

8. A. V Muraviev, V. O. Smolski, Z. E. Loparo, and K. L. Vodopyanov, "Massively parallel sensing of trace molecules and their isotopologues with broadband subharmonic mid-infrared frequency combs," Nat. Photonics **12**, 209–214 (2018).

9. K. F. Lee, C. J. Hensley, P. G. Schunemann, and M. E. Fermann, "Midinfrared frequency comb by difference frequency of erbium and thulium fiber lasers in orientation-patterned gallium phosphide," Opt. Express **25**, 17411–17416 (2017).

10. C. Gaida, T. Heuermann, M. Gebhardt, E. Shestaev, T. P. Butler, D. Gerz, N. Lilienfein, P. Sulzer, M. Fischer, R. Holzwarth, A. Leitenstorfer, I. Pupeza, and J. Limpert, "High-power frequency comb at 2 μm wavelength emitted by a Tm-doped fiber laser system," Opt. Lett. **43**, 5178 (2018).

11. T. P. Butler, D. Gerz, C. Hofer, J. Xu, C. Gaida, T. Heuermann, M. Gebhardt, L. Vamos, W. Schweinberger, J. A. Gessner, T. Siefke, M. Heusinger, U. Zeitner, A. Apolonski, N. Karpowicz, J. Limpert, F. Krausz, and I. Pupeza, "Watt-scale 50-MHz source of single-cycle waveform-stable pulses in the molecular fingerprint region," Opt. Lett. **44**, 1730–1733 (2019).

12. M. Scheller, M. S. Mills, M.-A. Miri, W. Cheng, J. V Moloney, M. Kolesik, P. Polynkin, and D. N. Christodoulides, "Externally refuelled optical filaments," Nat. Photonics **8**, 297–301 (2014).

13. Y. Wu, E. Cunningham, H. Zang, J. Li, M. Chini, X. Wang, Y. Wang, K. Zhao, and Z. Chang, "Generation of high-flux attosecond extreme ultraviolet continuum with a 10 TW laser," Appl. Phys. Lett. **102**, 201104 (2013).

14. D. Strickland and G. Mourou, "Compression of amplified chirped optical pulses," Opt. Commun. **56**, 219–221 (1985).

15. A. Dubietis, G. Jonušauskas, and A. Piskarskas, "Powerful femtosecond pulse generation by chirped and stretched pulse parametric amplification in BBO crystal," Opt. Commun. **88**, 437–440 (1992).

16. F. P. Kapron, D. B. Keck, and R. D. Maurer, "Radiation losses in glass optical waveguides," Appl. Phys. Lett. **17**, 423–425 (1970).

17. J. C. Knight, T. A. Birks, P. S. J. Russell, and D. M. Atkin, "All-silica single-mode optical fiber with photonic crystal cladding," Opt. Lett. **21**, 1547–1549 (1996).

18. J. C. Knight, "Photonic crystal fibres," Nature **424**, 847–851 (2003).

19. P. Russell, "Photonic crystal fibers," Science (80-.). **299**, 358–362 (2003).

20. J. K. Ranka, R. S. Windeler, and A. J. Stentz, "Visible continuum generation in air–silica microstructure optical fibers with anomalous dispersion at 800 nm," Opt. Lett. **25**, 25–27 (2000).

21. R. R. Alfano and S. L. Shapiro, "Emission in the region 4000 to 7000 Å via four-photon coupling in glass," Phys. Rev. Lett. **24**, 584 (1970).

22. C. Lin and R. H. Stolen, "New nanosecond continuum for excited-state spectroscopy," Appl. Phys. Lett. **28**, 216–218 (1976).

23. R. R. Alfano, *The Supercontinuum Laser Source: The Ultimate White Light* (Springer, 2016).

24. N. G. R. Broderick, T. M. Monro, P. J. Bennett, and D. J. Richardson, "Nonlinearity in holey optical fibers: measurement and future opportunities," Opt. Lett. **24**, 1395–1397 (1999).

25. T. A. Birks, J. C. Knight, and P. S. J. Russell, "Endlessly single-mode photonic crystal fiber," Opt. Lett. **22**, 961–963 (1997).

26. J. Herrmann, U. Griebner, N. Zhavoronkov, A. Husakou, D. Nickel, J. C. Knight, W. J. Wadsworth, P. S. J. Russell, and G. Korn, "Experimental Evidence for Supercontinuum Generation by Fission of Higher-Order Solitons in Photonic Fibers," Phys. Rev. Lett. **88**, 173901 (2002).

27. J. M. Dudley and S. Coen, "Coherence properties of supercontinuum spectra generated in photonic crystal and tapered optical fibers," Opt. Lett. **27**, 1180–1182 (2002).

28. K. L. Corwin, N. R. Newbury, J. M. Dudley, S. Coen, S. A. Diddams, K. Weber, and R. S. Windeler, "Fundamental Noise Limitations to Supercontinuum Generation in Microstructure Fiber," Phys. Rev. Lett. **90**, 113904 (2003).

29. J. M. Dudley, G. Genty, and S. Coen, "Supercontinuum generation in photonic crystal fiber," Rev. Mod. Phys. **78**, 1135–1184 (2006).

30. X. Gu, L. Xu, M. Kimmel, E. Zeek, P. O'Shea, A. P. Shreenath, R. Trebino, and R. S.

Windeler, "Frequency-resolved optical gating and single-shot spectral measurements reveal fine structure in microstructure-fiber continuum," Opt. Lett. **27**, 1174–1176 (2002).

31. X. Gu, M. Kimmel, A. P. Shreenath, R. Trebino, J. M. Dudley, S. Coen, and R. S. Windeler, "Experimental studies of the coherence of microstructure-fiber supercontinuum," Opt. Express **11**, 2697–2703 (2003).

32. A. M. Heidt, A. Hartung, G. W. Bosman, P. Krok, E. G. Rohwer, H. Schwoerer, and H. Bartelt, "Coherent octave spanning near-infrared and visible supercontinuum generation in all-normal dispersion photonic crystal fibers," Opt. Express **19**, 3775 (2011).

33. A. M. Heidt, "Pulse preserving flat-top supercontinuum generation in all-normal dispersion photonic crystal fibers," J. Opt. Soc. Am. B **27**, 550–559 (2010).

34. N. Nishizawa and J. Takayanagi, "Octave spanning high-quality supercontinuum generation in all-fiber system," JOSA B **24**, 1786–1792 (2007).

35. L. E. Hooper, P. J. Mosley, A. C. Muir, W. J. Wadsworth, and J. C. Knight, "Coherent supercontinuum generation in photonic crystal fiber with all-normal group velocity dispersion," Opt. Express **19**, 4902–4907 (2011).

36. Y. Liu, H. Tu, and S. A. Boppart, "Wave-breaking-extended fiber supercontinuum generation for high compression ratio transform-limited pulse compression," Opt. Lett. **37**, 2172–2174 (2012).

37. C. Finot, B. Kibler, L. Provost, and S. Wabnitz, "Beneficial impact of wave-breaking for coherent continuum formation in normally dispersive nonlinear fibers," JOSA B **25**, 1938–1948 (2008).

38. G. Millot, E. Seve, S. Wabnitz, and M. Haelterman, "Observation of induced modulational polarization instabilities and pulse-train generation in the normal-dispersion regime of a birefringent optical fiber," J. Opt. Soc. Am. B **15**, 1266 (1998).

39. Y. Liu, Y. Zhao, J. Lyngsø, S. You, W. L. Wilson, H. Tu, and S. A. Boppart, "Suppressing Short-Term Polarization Noise and Related Spectral Decoherence in All-Normal Dispersion Fiber Supercontinuum Generation," J. Light. Technol. **33**, 1814–1820 (2015).

40. S. R. Domingue and R. A. Bartels, "Overcoming temporal polarization instabilities from the latent birefringence in all-normal dispersion, wave-breaking-extended nonlinear fiber supercontinuum generation," Opt. Express **21**, 13305 (2013).

41. I. B. Gonzalo, R. D. Engelsholm, M. P. Sørensen, and O. Bang, "Polarization noise places severe constraints on coherence of all-normal dispersion femtosecond supercontinuum generation," Sci. Rep. **8**, 1–13 (2018).

42. K. Tarnowski, T. Martynkien, P. Mergo, K. Poturaj, A. Anuszkiewicz, P. Béjot, F. Billard, O. Faucher, B. Kibler, and W. Urbanczyk, "Polarized all-normal dispersion supercontinuum reaching 2.5 µm generated in a birefringent microstructured silica fiber," Opt. Express **25**, 27452 (2017).

43. D. Dobrakowski, A. Rampur, G. Stępniewski, A. Anuszkiewicz, J. Lisowska, D. Pysz, R. Kasztelanic, and M. Klimczak, "Development of highly nonlinear polarization-maintaining

fibers with normal dispersion across entire transmission window," J. Opt. (United Kingdom) **21**, (2019).

44. N. Zhang, X. Peng, Y. Wang, S. Dai, Y. Yuan, J. Su, G. Li, P. Zhang, P. Yang, and X. Wang, "Ultrabroadband and coherent mid-infrared supercontinuum generation in Te-based chalcogenide tapered fiber with all-normal dispersion," Opt. Express **27**, 10311–10319 (2019).

45. S. Rao D. S., R. D. Engelsholm, I. B. Gonzalo, B. Zhou, P. Bowen, P. M. Moselund, O. Bang, and M. Bache, "Ultra-low-noise supercontinuum generation with a flat near-zero normal dispersion fiber," Opt. Lett. **44**, 2216 (2019).

46. A. Hartung, A. M. Heidt, and H. Bartelt, "Nanoscale all-normal dispersion optical fibers for coherent supercontinuum generation at ultraviolet wavelengths," Opt. Express **20**, 13777–13788 (2012).

47. T. S. Saini, N. P. T. Hoa, T. H. Tuan, X. Luo, T. Suzuki, and Y. Ohishi, "Tapered tellurite step-index optical fiber for coherent near-to-mid-IR supercontinuum generation: experiment and modeling," Appl. Opt. **58**, 415–421 (2019).

48. E. Genier, P. Bowen, T. Sylvestre, J. M. Dudley, P. Moselund, and O. Bang, "Amplitude noise and coherence degradation of femtosecond supercontinuum generation in all-normal-dispersion fibers," J. Opt. Soc. Am. B **36**, A161 (2019).

49. J. Szczepanek, T. M. Kardaś, and Y. Stepanenko, "Group delay measurements of ultra-broadband pulses generated in highly nonlinear fibers," Photonics Lett. Pol. **8**, 107–109 (2016).

50. A. Okamura, Y. Sakakibara, E. Omoda, H. Kataura, and N. Nishizawa, "Experimental analysis of coherent supercontinuum generation and ultrashort pulse generation using cross-correlation frequency resolved optical gating (X-FROG)," JOSA B **32**, 400–406 (2015).

51. M. Klimczak, B. Siwicki, P. Skibiński, D. Pysz, R. Stępień, A. Heidt, C. Radzewicz, and R. Buczyński, "Coherent supercontinuum generation up to 2.3 µm in all-solid soft-glass photonic crystal fibers with flat all-normal dispersion," Opt. Express **22**, 18824 (2014).

52. M. Klimczak, B. Siwicki, B. Zhou, M. Bache, D. Pysz, O. Bang, and R. Buczyński, "Coherent supercontinuum bandwidth limitations under femtosecond pumping at 2 µm in all-solid soft glass photonic crystal fibers," Opt. Express **24**, 29406 (2016).

53. M. Klimczak, B. Siwicki, A. Heidt, and R. Buczyński, "Coherent supercontinuum generation in soft glass photonic crystal fibers," Photonics Res. **5**, 710 (2017).

54. J. M. Dudley and J. R. Taylor, *Supercontinuum Generation in Optical Fibers* (Cambridge University Press, 2010).

55. T. Udem, R. Holzwarth, and T. W. Hänsch, "Optical frequency metrology," Nature **416**, 233–237 (2002).

56. J. C. Knight, J. Arriaga, T. A. Birks, A. Ortigosa-Blanch, W. J. Wadsworth, and P. S. J. Russell, "Anomalous dispersion in photonic crystal fiber," IEEE photonics Technol. Lett. **12**, 807–809 (2000).

57. F. Poletti, X. Feng, G. M. Ponzo, M. N. Petrovich, W. H. Loh, and D. J. Richardson, "All-solid highly nonlinear singlemode fibers with a tailored dispersion profile," Opt. Express **19**, 66–80 (2011).

58. M. Seidel, X. Xiao, and A. Hartung, "Solid-core fiber spectral broadening at its limits," IEEE J. Sel. Top. Quantum Electron. **24**, 1–8 (2018).

59. S. Kumkar, G. Krauss, M. Wunram, D. Fehrenbacher, U. Demirbas, D. Brida, and A. Leitenstorfer, "Femtosecond coherent seeding of a broadband Tm:fiber amplifier by an Er:fiber system," Opt. Lett. **37**, 554–556 (2012).

60. N. Coluccelli, M. Cassinerio, P. Laporta, and G. Galzerano, "Single-clad Tm-Ho:fiber amplifier for high-power sub-100-fs pulses around 1.9 µm," Opt. Lett. **38**, 2757–2759 (2013).

61. F. Tan, H. Shi, R. Sun, P. Wang, and P. Wang, "1 µJ, sub-300 fs pulse generation from a compact thulium-doped chirped pulse amplifier seeded by Raman shifted erbium-doped fiber laser," Opt. Express **24**, 22461–22468 (2016).

62. G. Soboń, T. Martynkien, D. Tomaszewska, K. Tarnowski, PawełMergo, and J. Sotor, "All-in-fiber amplification and compression of coherent frequency-shifted solitons tunable in the 1800-2000nm range," Photon. Res. **6**, 368–372 (2018).

63. A. M. Heidt, J. Modupeh Hodasi, A. Rampur, D.-M. Spangenberg, M. Ryser, M. Klimczak, and T. Feurer, "Low noise all-fiber amplification of a coherent supercontinuum at 2 µm and its limits imposed by polarization noise," arXiv e-prints arXiv:1903.09583 (2019).

64. A. M. Heidt, A. Hartung, and H. Bartelt, "The Supercontinuum Laser Source: The Ultimate White Light," in (Springer New York, 2016), pp. 247–280.

65. A. M. Heidt, J. S. Feehan, J. H. V. Price, and T. Feurer, "Limits of coherent supercontinuum generation in normal dispersion fibers," J. Opt. Soc. Am. B **34**, 764–775 (2017).

66. N. R. Newbury, B. R. Washburn, K. L. Corwin, and R. S. Windeler, "Noise amplification during supercontinuum generation in microstructure fiber," Opt. Lett. **28**, 944–946 (2003).

67. A. M. Heidt, J. Rothhardt, A. Hartung, H. Bartelt, E. G. Rohwer, J. Limpert, and A. Tünnermann, "High quality sub-two cycle pulses from compression of supercontinuum generated in all-normal dispersion photonic crystal fiber," Opt. Express **19**, 13873–13879 (2011).

68. S. Demmler, J. Rothhardt, A. M. Heidt, A. Hartung, E. G. Rohwer, H. Bartelt, J. Limpert, and A. Tünnermann, "Generation of high quality, 1.3 cycle pulses by active phase control of an octave spanning supercontinuum," Opt. Express **19**, 20151 (2011).

69. J. Rothhardt, A. M. Heidt, S. Hädrich, S. Demmler, J. Limpert, and A. Tünnermann, "High stability soliton frequency-shifting mechanisms for laser synchronization applications," J. Opt. Soc. Am. B **29**, 1257–1262 (2012).

70. P. Ciąćka, A. Rampur, A. Heidt, T. Feurer, and M. Klimczak, "Dispersion measurement of ultra-high numerical aperture fibers covering thulium, holmium, and erbium emission wavelengths," J. Opt. Soc. Am. B **35**, 1301–1307 (2018).

71. J. Tyndall, *Notes of a Course of Nine Lectures on Light: Delivered at the Royal Institution of Great Britain, April 8-June 3, 1869* (Longmans, Green, and Company, 1872).

72. J. Tyndall, *Six Lectures on Light: Delivered in America in 1872-1873* (Longmans, Green, 1873).

73. R. J. Mears, L. Reekie, I. M. Jauncey, and D. N. Payne, "Low-noise erbium-doped fibre amplifier operating at 1.54 µm," Electron. Lett. **23**, 1026–1028 (1987).

74. B. N. Chichkov, C. Momma, S. Nolte, F. Von Alvensleben, and A. Tünnermann, "Femtosecond, picosecond and nanosecond laser ablation of solids," Appl. Phys. A **63**, 109–115 (1996).

75. P. Giaccari, J.-D. Deschênes, P. Saucier, J. Genest, and P. Tremblay, "Active Fourier-transform spectroscopy combining the direct RF beating of two fiber-based mode-locked lasers with a novel referencing method," Opt. Express **16**, 4347–4365 (2008).

76. W. Liu, S.-H. Chia, H.-Y. Chung, R. Greinert, F. X. Kärtner, and G. Chang, "Energetic ultrafast fiber laser sources tunable in 1030–1215 nm for deep tissue multi-photon microscopy," Opt. Express **25**, 6822–6831 (2017).

77. R. Buczynski, "Photonic crystal fibers," Acta Phys. Pol. Ser. A **106**, 141–168 (2004).

78. B. E. A. Saleh and M. C. Teich, "Fundamental of Photonics, New Jersey: John and Wiley & Sons," (2007).

79. G. P. Agrawal, *Nonlinear Fiber Optics* (Academic Press, 2007).

80. C. Incorporated, "Corning SMF-28 ultra optical fiber product information," https://www.corning.com/media/worldwide/coc/documents/Fiber/SMF-28 Ultra.pdf.

81. C. Dunsby and P. M. W. French, "Biophotonics applications of supercontinuum generation," in *Supercontinuum Generation in Optical Fibers*, J. M. Dudley and J. R. Taylor, eds. (Cambridge University Press, 2010), pp. 349–372.

82. G. Soboń, T. Martynkien, K. Tarnowski, P. Mergo, and J. Sotor, "Generation of sub-100 fs pulses tunable from 1700 to 2100 nm from a compact frequency-shifted Er-fiber laser," Photonics Res. **5**, 151–155 (2017).

83. J. Sotor, T. Martynkien, P. G. Schunemann, P. Mergo, L. Rutkowski, and G. Soboń, "All-fiber mid-infrared source tunable from 6 to 9 µm based on difference frequency generation in OP-GaP crystal," Opt. Express **26**, 11756–11763 (2018).

84. A. A. Rieznik, A. M. Heidt, P. G. Konig, V. A. Bettachini, and D. F. Grosz, "Optimum Integration Procedures for Supercontinuum Simulation," IEEE Photonics J. **4**, 552–560 (2012).

85. R. H. Stolen and C. Lin, "Self-phase-modulation in silica optical fibers," Phys. Rev. A **17**, 1448 (1978).

86. Y. Kodama and A. Hasegawa, "Nonlinear pulse propagation in a monomode dielectric guide," IEEE J. Quantum Electron. **23**, 510–524 (1987).

87. F. M. Mitschke and L. F. Mollenauer, "Discovery of the soliton self-frequency shift," Opt. Lett. **11**, 659–661 (1986).

88. J. P. Gordon, "Theory of the soliton self-frequency shift," Opt. Lett. **11**, 662–664 (1986).

89. N. Akhmediev and M. Karlsson, "Cherenkov radiation emitted by solitons in optical fibers," Phys. Rev. A **51**, 2602 (1995).

90. F. Vanholsbeeck, S. Martin-Lopez, M. González-Herráez, and S. Coen, "The role of pump incoherence in continuous-wave supercontinuum generation," Opt. Express **13**, 6615–6625 (2005).

91. A. Mussot, E. Lantz, H. Maillotte, T. Sylvestre, C. Finot, and S. Pitois, "Spectral broadening of a partially coherent CW laser beam in single-mode optical fibers," Opt. Express **12**, 2838–2843 (2004).

92. S. M. Kobtsev and S. V Smirnov, "Modelling of high-power supercontinuum generation in highly nonlinear, dispersion shifted fibers at CW pump," Opt. Express **13**, 6912–6918 (2005).

93. M. Remoissenet, *Waves Called Solitons*, Advanced Texts in Physics (Springer Berlin Heidelberg, 1999).

94. A. Demircan and U. Bandelow, "Supercontinuum generation by the modulation instability," Opt. Commun. **244**, 181–185 (2005).

95. J. M. Dudley and G. Genty, "Supercontinuum light," Phys. Today **66**, 29–34 (2013).

96. A. Höök and M. Karlsson, "Ultrashort solitons at the minimum-dispersion wavelength: effects of fourth-order dispersion," Opt. Lett. **18**, 1388–1390 (1993).

97. F. K. Abdullaev, S. A. Darmanyan, S. Bischoff, P. L. Christiansen, and M. P. Sørensen, "Modulational instability in optical fibers near the zero dispersion point," Opt. Commun. **108**, 60–64 (1994).

98. J. D. Harvey, R. Leonhardt, S. Coen, G. K. L. Wong, J. Knight, W. J. Wadsworth, and P. S. J. Russell, "Scalar modulation instability in the normal dispersion regime by use of a photonic crystal fiber," Opt. Lett. **28**, 2225–2227 (2003).

99. T. Tanemura, Y. Ozeki, and K. Kikuchi, "Modulational instability and parametric amplification induced by loss dispersion in optical fibers," Phys. Rev. Lett. **93**, 163902 (2004).

100. G. P. Agrawal, "Modulation instability induced by cross-phase modulation," Phys. Rev. Lett. **59**, 880 (1987).

101. S. Coen and M. Haelterman, "Modulational instability induced by cavity boundary conditions in a normally dispersive optical fiber," Phys. Rev. Lett. **79**, 4139 (1997).

102. A. V Gorbach, D. V Skryabin, J. M. Stone, and J. C. Knight, "Four-wave mixing of solitons with radiation and quasi-nondispersive wave packets at the short-wavelength edge of a supercontinuum," Opt. Express **14**, 9854–9863 (2006).

103. G. Genty, M. Lehtonen, and H. Ludvigsen, "Effect of cross-phase modulation on supercontinuum generated in microstructured fibers with sub-30 fs pulses," Opt. Express **12**, 4614–4624 (2004).

104. D. V Skryabin and A. V Yulin, "Theory of generation of new frequencies by mixing of solitons and dispersive waves in optical fibers," Phys. Rev. E **72**, 16619 (2005).

105. A. Efimov, A. J. Taylor, F. G. Omenetto, A. V Yulin, N. Y. Joly, F. Biancalana, D. V Skryabin, J. C. Knight, and P. S. J. Russell, "Time-spectrally-resolved ultrafast nonlinear dynamics in small-core photonic crystal fibers: Experiment and modelling," Opt. Express **12**, 6498–6507 (2004).

106. S. Wabnitz, "Modulational polarization instability of light in a nonlinear birefringent dispersive medium," Phys. Rev. A **38**, 2018 (1988).

107. S. G. Murdoch, R. Leonhardt, and J. D. Harvey, "Polarization modulation instability in weakly birefringent fibers," Opt. Lett. **20**, 866–868 (1995).

108. "ET-5000 - >12 GHz 2 μm Extended InGaAs Photodetector," https://www.eotech.com/cart/116/photodetectors/%3E10-ghz-photodetectors/et-5000---%3E12-ghz-2-μm-extended-ingaas-photodetector.

109. K. Sala, G. Kenney-Wallace, and G. Hall, "CW autocorrelation measurements of picosecond laser pulses," IEEE J. Quantum Electron. **16**, 990–996 (1980).

110. R. Wyatt and E. E. Marinero, "Versatile single-shot background-free pulse duration measurement technique, for pulses of subnanosecond to picosecond duration," Appl. Phys. **25**, 297–301 (1981).

111. D. J. Kane and R. Trebino, "Characterization of arbitrary femtosecond pulses using frequency-resolved optical gating," IEEE J. Quantum Electron. **29**, 571–579 (1993).

112. R. Trebino and D. J. Kane, "Using phase retrieval to measure the intensity and phase of ultrashort pulses: frequency-resolved optical gating Rick," J. Opt. Soc. Am. A **10**, 1–11 (1993).

113. D. J. Kane and R. Trebino, "Single-shot measurement of the intensity and phase of an arbitrary ultrashort pulse by using frequency-resolved optical gating," Opt. Lett. **18**, 823–825 (1993).

114. R. Trebino, *Frequency-Resolved Optical Gating: The Measurement of Ultrashort Laser Pulses* (Springer Science & Business Media, 2012).

115. R. Trebino, K. W. DeLong, D. N. Fittinghoff, J. N. Sweetser, M. A. Krumbügel, B. A. Richman, and D. J. Kane, "Measuring ultrashort laser pulses in the time-frequency domain using frequency-resolved optical gating," Rev. Sci. Instrum. **68**, 3277–3295 (1997).

116. K. W. DeLong, R. Trebino, J. Hunter, and W. E. White, "Frequency-resolved optical gating with the use of second-harmonic generation," JOSA B **11**, 2206–2215 (1994).

117. T. S. Clement, A. J. Taylor, and D. J. Kane, "Single-shot measurement of the amplitude and phase of ultrashort laser pulses in the violet," Opt. Lett. **20**, 70–72 (1995).

118. J. N. Sweetser, D. N. Fittinghoff, and R. Trebino, "Transient-grating frequency-resolved optical gating," Opt. Lett. **22**, 519–521 (1997).

119. S. Linden, H. Giessen, and J. Kuhl, "XFROG - A new method for amplitude and phase characterization of weak ultrashort pulses," Phys. Status Solidi Basic Res. **206**, 119–124 (1998).

120. S. Linden, J. Kuhl, and H. Giessen, "Amplitude and phase characterization of weak blue ultrashort pulses by downconversion," Opt. Lett. **24**, 569–571 (1999).

121. J. Ratner and R. Trebino, "XFROG Retrieval of Extremely Complex Pulses," in *Frontiers in Optics* (Optical Society of America, 2011), p. FThV6.

122. J. Zhang, A. P. Shreenath, M. Kimmel, E. Zeek, R. Trebino, and S. Link, "Measurement of the intensity and phase of attojoule femtosecond light pulses using optical-parametric-amplification cross-correlation frequency-resolved optical gating," Opt. Express **11**, 601–609 (2003).

123. L. Xu, X. Gu, M. Kimmel, P. O'Shea, R. Trebino, and A. Galvanauskas, "Ultra-broadband IR continuum generation and its phase measurement using cross-correlation FROG," in *Technical Digest. Summaries of Papers Presented at the Conference on Lasers and Electro-Optics. Postconference Technical Digest (IEEE Cat. No. 01CH37170)* (IEEE, 2001), pp. 198–200.

124. P. O'Shea, M. Kimmel, X. Gu, and R. Trebino, "Increased-bandwidth in ultrashort-pulse measurement using an angle-dithered nonlinear-optical crystal," Opt. Express **7**, 342–349 (2000).

125. J. M. Dudley, X. Gu, L. Xu, M. Kimmel, E. Zeek, P. O'Shea, R. Trebino, S. Coen, and R. S. Windeler, "Cross-correlation frequency resolved optical gating analysis of broadband continuum generation in photonic crystal fiber: simulations and experiments," Opt. Express **10**, 1215 (2002).

126. Q. Cao, X. Gu, E. Zeek, M. Kimmel, R. Trebino, J. Dudley, and R. S. Windeler, "Measurement of the intensity and phase of supercontinuum from an 8-mm-long microstructure fiber," Appl. Phys. B **77**, 239–244 (2003).

127. B. Tsermaa, B. K. Yang, M. W. Kim, and J. S. Kim, "Characterization of supercontinuum and ultraviolet pulses by using XFROG," J. Opt. Soc. Korea **13**, 158–165 (2009).

128. J. Teipel, K. Franke, D. Türke, F. Warken, D. Meiser, M. Leuschner, and H. Giessen, "Characteristics of supercontinuum generationin tapered fibers using femtosecond laser pulses," Appl. Phys. B **77**, 245–251 (2003).

129. S. N. Bagaev, V. I. Denisov, V. F. Zakharyash, V. M. Klementyev, S. M. Kobtsev, S. A. Kuznetsov, S. V Kukarin, V. S. Pivtsov, S. V Smirnov, and N. V Fateev, "Spectral and temporal characteristics of a supercontinuum in tapered optical fibres," Quantum Electron. **34**, 1107 (2004).

130. T. C. Wong, M. Rhodes, and R. Trebino, "Single-shot measurement of the complete temporal intensity and phase of supercontinuum," Optica **1**, 119 (2014).

131. K. W. DeLong, D. N. Fittinghoff, R. Trebino, B. Kohler, and K. Wilson, "Pulse retrieval in frequency-resolved optical gating based on the method of generalized projections," Opt. Lett. **19**, 2152–2154 (1994).

132. D. Spangenberg, P. Neethling, E. Rohwer, M. H. Brügmann, and T. Feurer, "Time-domain ptychography," Phys. Rev. A **91**, 21803 (2015).

133. D. Spangenberg, E. Rohwer, M. H. Brügmann, and T. Feurer, "Ptychographic ultrafast pulse reconstruction," Opt. Lett. **40**, 1002–1005 (2015).

134. D.-M. Spangenberg, M. Brügmann, E. Rohwer, and T. Feurer, "All-optical implementation of a time-domain ptychographic pulse reconstruction setup," Appl. Opt. **55**, 5008–5013 (2016).

135. K. W. DeLong and R. Trebino, "Improved ultrashort pulse-retrieval algorithm for frequency-resolved optical gating," J. Opt. Soc. Am. A **11**, 2429–2437 (1994).

136. H. M. L. Faulkner and J. M. Rodenburg, "Error tolerance of an iterative phase retrieval algorithm for moveable illumination microscopy," Ultramicroscopy **103**, 153–164 (2005).

137. A. M. Maiden and J. M. Rodenburg, "An improved ptychographical phase retrieval algorithm for diffractive imaging," Ultramicroscopy **109**, 1256–1262 (2009).

138. A. M. Heidt, D.-M. Spangenberg, M. Brügmann, E. G. Rohwer, and T. Feurer, "Improved retrieval of complex supercontinuum pulses from XFROG traces using a ptychographic algorithm," Opt. Lett. **41**, 4903 (2016).

139. M. Lucchini, M. H. Brügmann, A. Ludwig, L. Gallmann, U. Keller, and T. Feurer, "Ptychographic reconstruction of attosecond pulses," Opt. Express **23**, 29502–29513 (2015).

140. T. Witting, D. Greening, D. Walke, P. Matia-Hernando, T. Barillot, J. P. Marangos, and J. W. G. Tisch, "Time-domain ptychography of over-octave-spanning laser pulses in the single-cycle regime," Opt. Lett. **41**, 4218–4221 (2016).

141. D. J. Kane, "Comparison of the Ptychographic Inversion Engine to Principal Components Generalized Projections," IEEE J. Sel. Top. Quantum Electron. **25**, (2019).

142. C. Nufern, "Ultra-High NA Single-Mode Fibers," https://www.nufern.com/pam/optical_fibers/spec/id/988/.

143. C. Nufern, "PM2000D," https://www.nufern.com/pam/optical_fibers/3017/pm2000d/.

144. K. Kieu and F. W. Wise, "Soliton thulium-doped fiber laser with carbon nanotube saturable absorber," IEEE Photonics Technol. Lett. (2009).

145. R. Kadel and B. R. Washburn, "All-fiber passively mode-locked thulium/holmium laser with two center wavelengths," Appl. Opt. **51**, 6465–6470 (2012).

146. Q. Wang, T. Chen, M. Li, B. Zhang, Y. Lu, and K. P. Chen, "All-fiber ultrafast thulium-doped fiber ring laser with dissipative soliton and noise-like output in normal dispersion by single-wall carbon nanotubes," Appl. Phys. Lett. **103**, 19–22 (2013).

147. F. Haxsen, A. Ruehl, M. Engelbrecht, D. Wandt, U. Morgner, and D. Kracht, "Stretched-pulse operation of a thulium-doped fiber laser," Opt. Express **16**, 20471 (2008).

148. A. Wienke, F. Haxsen, D. Wandt, U. Morgner, J. Neumann, and D. Kracht, "Ultrafast, stretched-pulse thulium-doped fiber laser with a fiber-based dispersion management," Opt. Lett. **37**, 2466 (2012).

149. R. Kadel and B. R. Washburn, "Stretched-pulse and solitonic operation of an all-fiber thulium/holmium-doped fiber laser," Appl. Opt. **54**, 746 (2015).

150. H. Li, J. Liu, Z. Cheng, J. Xu, F. Tan, and P. Wang, "Pulse-shaping mechanisms in passively mode-locked thulium-doped fiber lasers," Opt. Express **23**, 6292 (2015).

151. Y. Tang, A. Chong, and F. W. Wise, "Generation of 8 nJ pulses from a normal-dispersion thulium fiber laser," Opt. Lett. **40**, 2361 (2015).

152. H. Liu, K. Kieu, S. Lefrancois, W. H. Renninger, A. Chong, and F. W. Wise, "Tm fiber laser mode-locked at large normal dispersion," Opt. InfoBase Conf. Pap. 24–25 (2011).

153. F. Haxsen, D. Wandt, U. Morgner, J. Neumann, and D. Kracht, "Monotonically chirped pulse evolution in an ultrashort pulse thulium-doped fiber laser," Opt. Lett. (2012).

154. G. Sobon, J. Sotor, T. Martynkien, and K. M. Abramski, "Ultra-broadband dissipative soliton and noise-like pulse generation from a normal dispersion mode-locked Tm-doped all-fiber laser," Opt. Express **24**, 6156 (2016).

155. D. L. Marks, A. L. Oldenburg, J. J. Reynolds, and S. A. Boppart, "Study of an ultrahigh-numerical-aperture fiber continuum generation source for optical coherence tomography," Opt. Lett. **27**, 2010 (2002).

156. N. Nishizawa, Y. Chen, F. Hsiung, V. Sharma, T. H. Ko, and J. G. Fujimoto, "All fiber high resolution OCT system using an ultrashort pulse high power fiber laser," OSA Trends Opt. Photonics Ser. **96 A**, 1109–1110 (2004).

157. C.-L. Pan, A. Zaytse, Y.-J. You, and C.-H. Li, "Fiber-laser-generated Noise-like Pulses and Their Applications," in *Fiber Laser* (2016).

158. and H. B. A. M. Heidt, A. Hartung, "Generation of ultrashort and coherent supercontinuum light pulses in all-normal dispersion fibers," in *The Supercontinuum Laser Source: The Ultimate White Light,R. R. Alfano* (Springer, 2016), pp. 247–280.

159. B. Costa, D. Mazzoni, M. Puleo, and E. Vezzoni, "Phase Shift Technique for the Measurement of Chromatic Dispersion in Optical Fibers Using LED's," IEEE J. Quantum Electron. (1982).

160. P. Hlubina, M. Kadulová, and D. Ciprian, "Spectral interferometry-based chromatic dispersion measurement of fibre including the zero-dispersion wavelength," J. Eur. Opt. Soc. **7**, (2012).

161. G. M. Ponzo, M. N. Petrovich, X. Feng, P. Horak, F. Poletti, P. Petropoulos, and D. J. Richardson, "Fast and broadband fiber dispersion measurement with dense wavelength sampling," Opt. Express **22**, 943 (2014).

162. J. M. Hodasi, A. Heidt, M. Klimczak, B. Siwicki, and T. Feurer, "Femtosecond seeding of a Tm-Ho fiber amplifier by a broadband coherent supercontinuum pulse from an all-solid all-normal photonic crystal fiber," in *2017 European Conference on Lasers and Electro-Optics and European Quantum Electronics Conference* (Optical Society of America, 2017), p. CJ_P_7.

163. A. Rampur, Y. Stepanenko, G. Stępniewski, T. Kardaś, D. Dobrakowski, D.-M. Spangenberg, T. Feurer, A. Heidt, and M. Klimczak, "Ultra low-noise coherent supercontinuum amplification and compression below 100 fs in an all-fiber polarization-maintaining thulium fiber amplifier," Opt. Express **27**, 35041 (2019).

164. F. W. Wise, A. Chong, and W. H. Renninger, "High-energy femtosecond fiber lasers based on pulse propagation at normal dispersion," Laser Photonics Rev. **2**, 58–73 (2008).

165. J. Rothhardt, S. Demmler, S. Hädrich, J. Limpert, and A. Tünnermann, "Octave-spanning OPCPA system delivering CEP-stable few-cycle pulses and 22 W of average power at 1 MHz repetition rate," Opt. Express **20**, 10870–10878 (2012).

166. J. Rothhardt, S. Hädrich, J. C. Delagnes, E. Cormier, and J. Limpert, "High Average Power Near-Infrared Few-Cycle Lasers," Laser Photon. Rev. **11**, (2017).

167. H. Tu and S. A. Boppart, "Coherent fiber supercontinuum for biophotonics," Laser Photon. Rev. **7**, 628–645 (2013).

168. H. Tu and S. A. Boppart, "Coherent anti-Stokes Raman scattering microscopy: overcoming technical barriers for clinical translation," J. Biophoton. **7**, 9–22 (2014).

169. N. Nishizawa, "Wideband ultrafast fiber laser sources for OCT and metrology," J. Phys. B At. Mol. Opt. Phys. **49**, 182003 (2016).

170. N. M. Kearns, A. C. Jones, M. B. Kunz, R. T. Allen, J. T. Flach, and M. T. Zanni, "Two-dimensional white-light spectroscopy using supercontinuum from an all-normal dispersion photonic crystal fiber pumped by a 70 MHz Yb fiber oscillator," J. Phys. Chem. A **123**, 3046–3055 (2019).

171. Y. Wang, S. Dai, G. Li, D. Xu, C. You, X. Han, P. Zhang, X. Wang, and P. Xu, "1.4--7.2 μm broadband supercontinuum generation in an As-S chalcogenide tapered fiber pumped in the normal dispersion regime," Opt. Lett. **42**, 3458–3461 (2017).

172. K. Tarnowski, T. Martynkien, P. Mergo, J. Sotor, and G. Soboń, "Compact all-fiber source of coherent linearly polarized octave-spanning supercontinuum based on normal dispersion silica fiber," Sci. Rep. **9**, 12313 (2019).

173. K. Tarnowski, T. Martynkien, P. Mergo, K. Poturaj, G. Soboń, and W. Urbańczyk, "Coherent supercontinuum generation up to 2.2 μm in an all-normal dispersion microstructured silica fiber," Opt. Express **24**, 30523 (2016).

174. S. Dupont, P. M. Moselund, L. Leick, J. Ramsay, and S. R. Keiding, "Up-conversion of a megahertz mid-IR supercontinuum," J. Opt. Soc. Am. B **30**, 2570–2575 (2013).

175. J. C. Travers, "Blue solitary waves from infrared continuous wave pumping of optical fibers," Opt. Express **17**, 1502 (2009).

176. Y. Shen, A. A. Voronin, A. M. Zheltikov, S. P. O'Connor, V. V. Yakovlev, A. V. Sokolov, and M. O. Scully, "Picosecond supercontinuum generation in large mode area photonic crystal fibers for coherent anti-Stokes Raman scattering microspectroscopy," Sci. Rep. **8**, 1–12 (2018).

177. J. Vengelis, V. Jarutis, and V. Sirutkaitis, "Estimation of photonic crystal fiber dispersion by means of supercontinuum generation," Opt. Lett. **42**, 1844 (2017).

178. A. Rampur, D.-M. Spangenberg, G. Stepniewski, D. Dobrakowski, K. Tarnowski, K. Stefanska, A. Pazdzior, P. Mergo, T. Martynkien, T. Feurer, M. Klimczak, and A. Heidt, "Temporal fine structure of all-normal dispersion fiber supercontinuum pulses caused by non-ideal pump pulse shapes," (accepted for publication in Optics Express).

179. G. Taft, A. Rundquist, M. M. Murnane, I. P. Christov, H. C. Kapteyn, K. W. DeLong, D. N. Fittinghoff, M. A. Krumbugel, J. N. Sweetser, and R. Trebino, "Measurement of 10-fs laser pulses," IEEE J. Sel. Top. Quantum Electron. **2**, 575–585 (1996).

180. D. Brida, G. Krauss, A. Sell, and A. Leitenstorfer, "Ultrabroadband Er: fiber lasers," Laser Photon. Rev. **8**, 409–428 (2014).

181. B. Kibler, J. M. Dudley, and S. Coen, "Supercontinuum generation and nonlinear pulse propagation in photonic crystal fiber: influence of the frequency-dependent effective mode area," Appl. Phys. B **81**, 337–342 (2005).

182. J. Luo, B. Sun, J. Liu, Z. Yan, N. Li, E. L. Tan, Q. Wang, and X. Yu, "Mid-IR supercontinuum pumped by femtosecond pulses from thulium doped all-fiber amplifier," Opt. Express **24**, 13939–13945 (2016).

183. A. Khodabakhsh, V. Ramaiah-Badarla, L. Rutkowski, A. C. Johansson, K. F. Lee, J. Jiang, C. Mohr, M. E. Fermann, and A. Foltynowicz, "Fourier transform and Vernier spectroscopy using an optical frequency comb at 3–5.4 μm," Opt. Lett. **41**, 2541–2544 (2016).

184. T. Heuermann, C. Gaida, M. Gebhardt, and J. Limpert, "50 fs-pulses emitted by a Tm-doped nonlinear fiber amplifier at 20 W of average power," Opt. InfoBase Conf. Pap. **Part F121-**, 4441–4444 (2018).

185. C. Gaida, M. Gebhardt, T. Heuermann, F. Stutzki, C. Jauregui, and J. Limpert, "Ultrafast thulium fiber laser system emitting more than 1 kW of average power," Opt. Lett. **43**, 5853 (2018).

186. F. Adler and S. A. Diddams, "High-power, hybrid Er:fiber/Tm:fiber frequency comb source in the 2 μm wavelength region," Opt. Lett. **37**, 1400 (2012).

187. N. Coluccelli, M. Cassinerio, A. Gambetta, P. Laporta, and G. Galzerano, "High-power frequency comb in the range of 2–2.15 μm based on a holmium fiber amplifier seeded by wavelength-shifted Raman solitons from an erbium-fiber laser," Opt. Lett. **39**, 1661 (2014).

188. N. R. Newbury and W. C. Swann, "Low-noise fiber-laser frequency combs (Invited)," J. Opt. Soc. Am. B **24**, 1756–1770 (2007).

189. H. Hoogland, A. Thai, D. Sánchez, S. L. Cousin, M. Hemmer, M. Engelbrecht, J. Biegert, and R. Holzwarth, "All-PM coherent 2.05 µm Thulium/Holmium fiber frequency comb

source at 100 MHz with up to 0.5 W average power and pulse duration down to 135 fs," Opt. Express **21**, 31390–31394 (2013).

190. T. Heuermann, C. Gaida, M. Gebhardt, and J. Limpert, "Thulium-doped nonlinear fiber amplifier delivering 50 fs pulses at 20 W of average power," Opt. Lett. **43**, 4441 (2018).

191. H. Tu, Y. Liu, X. Liu, D. Turchinovich, J. Lægsgaard, and S. A. Boppart, "Nonlinear polarization dynamics in a weakly birefringent all-normal dispersion photonic crystal fiber: toward a practical coherent fiber supercontinuum laser," Opt. Express **20**, 1113–1128 (2012).

192. "CorActive DCF-EY-6/128-PM," https://coractive.com/fileadmin/documents_publics/boutique/Activefibers/eryb-fibers/DCF-EY-6_128-PM_DS100690r1.2.pdf%0D.

193. "Nufern PM-TSF-9/125," https://www.nufern.com/pam/optical_fibers/5/PM-TSF-9/125/#.

194. "Nufern Tm Cross Section," http://www.nufern.com/marketing/fiber_data/Tm_Cross_Section.xlsx.

195. R. P. Scott, C. Langrock, and B. H. Kolner, "High-dynamic-range laser amplitude and phase noise measurement techniques," IEEE J. Sel. Top. Quantum Electron. **7**, 641–655 (2001).

196. C. Gaida, M. Gebhardt, T. Heuermann, F. Stutzki, C. Jauregui, and J. Limpert, "Ultrafast thulium fiber laser system emitting more than 1 kW of average power," Opt. Lett. **43**, 5853–5856 (2018).

197. D. Churin, K. Kieu, R. A. Norwood, and N. Peyghambarian, "Efficient Frequency Comb Generation in the 9-µm Region Using Compact Fiber Sources," IEEE Photonics Technol. Lett. **26**, 2271–2274 (2014).

198. G. Krauss, S. Lohss, T. Hanke, A. Sell, S. Eggert, R. Huber, and A. Leitenstorfer, "Synthesis of a single cycle of light with compact erbium-doped fibre technology," Nat. Photonics **4**, 33 (2009).

199. M. Klimczak, D. Michalik, G. Stępniewski, T. Karpate, J. Cimek, X. Forestier, R. kasztelanic, D. Pysz, R. Stępień, and R. Buczyński, "Coherent supercontinuum generation in tellurite glass regular lattice photonic crystal fibers," J. Opt. Soc. Am. B **36**, A112–A124 (2019).

200. "iXblue Photonics IXF-EDF-HD-PM," https://photonics.ixblue.com/sites/default/files/2019-01/IXF-EDF-HD-PM_edA Er SC highly doped PM fiber.pdf.

201. T. W. Neely, T. A. Johnson, and S. A. Diddams, "High-power broadband laser source tunable from 3.0 µm to 4.4 µmbased on a femtosecond Yb:fiber oscillator," Opt. Lett. **36**, 4020–4022 (2011).

202. T. Karpate, G. Stepniewski, D. Pysz, A. Rampur, Y. Stepanenko, R. Buczynski, and M. Klimczak, "Soliton detuning of 68.5 THz in the near-infrared in a highly nonlinear suspended core tellurite fiber," J. Opt. Soc. Am. B **37**, 1502–1509 (2020).